

VRIJE UNIVERSITEIT

High-Precision Rovibrational Saturation Spectroscopy of H₂, HD and HT

ACADEMISCH PROEFSCHRIFT

ter verkrijging van de graad Doctor
aan de Vrije Universiteit Amsterdam,
op gezag van de rector magnificus
prof.dr. J.J.G. Geurts,
in het openbaar te verdedigen
ten overstaan van de promotiecommissie
van de Faculteit der Bètawetenschappen
op vrijdag 25 oktober 2024 om 09.45 uur
in een bijeenkomst van de universiteit,
De Boelelaan 1105

door

Franciscus Martinus Jacobus Cozijn
geboren te Leiderdorp

promotor: prof.dr. W.M.G. Ubachs

copromotor: dr. E.J. Salumbides

promotiecommissie: dr. L.V. Amitonova
prof.dr. A. Freise
prof.dr. C. Lauzin
prof.dr. J. Oomens
dr. R.J.C. Spreeuw

For my son Tobi

*In a lab where molecules dance and play,
A technique called NICE-OHMS leads the way.
It's sensitive, precise, and immune to noise,
A spectroscopy method that everyone enjoys.*

*With a laser so bright and a cavity so tight,
The sidebands emerge with EOM's might.
The modulation's high, yet the linewidth's thin,
Measuring weak transitions with a triumphant grin.*

*A breakthrough was made, a feat so grand,
A quadrupole transition in hydrogen, first in the land.
Saturation spectroscopy brought it so near,
NICE-OHMS, the hero, made it appear.*

ChatGPT 4.0 (prompted by me)

The work was performed at the LaserLaB at the Vrije Universiteit Amsterdam. Funding for the project was obtained through a European Research Council Advanced Grant (Ubachs - 670168) under the European Union's Horizon 2020 research and innovation program. Additional funding was obtained through the Dutch Astrochemistry Network (NWO), and the NWO-Program "The mysterious size of the proton".



The cover shows a phase-modulated lightwave incident on an enhancement cavity, causing three distinctive resonant laser fields in the cavity (the carrier and two modulated sidebands). This represents the basics of the NICE-OHMS technique, which is the foundation of all measurements in this Thesis. In the bottom right corner of the front and back side, a schematic representation of the hydrogen molecule is shown in the para and ortho states. .

Printed by Ipskamp Printing B.V., Enschede
DOI: <https://doi.org/10.5463/thesis.744>

Contents

1	Introduction and Summary	1
1.1	The hydrogen molecule as a quantum benchmark	1
1.2	History and future of the rovibrational states	2
1.3	Summary	5
1.4	Concluding remarks and outlook	6
2	Frequency comb referenced NICE-OHMS for saturation spectroscopy of extremely weak rovibrational transitions	9
2.1	Introduction	9
2.2	NICE-OHMS principles	11
2.2.1	Frequency modulation spectroscopy formalism	11
2.2.2	Cavity-enhanced saturation spectroscopy	13
2.2.3	Wavelength modulation	16
2.2.4	Typical implementation of NICE-OHMS	16
2.3	Residual amplitude modulation	19
2.3.1	Introduction	19
2.3.2	RAM originating from the EOM	19
2.3.3	Residual etalons causing RAM	20
2.3.4	Methods of reducing impact of etalons	22
2.3.5	Independent RAM measurement	25
2.4	Laser source and optical beampath	25
2.5	Parallel demodulation through a high-speed digital lock-in amplifier	30
2.6	Active PDH setpoint stabilization	33
2.7	Frequency comb referencing	36

3	Vibration insensitive cryogenic cavity design for cavity-enhanced saturation spectroscopy	39
3.1	Introduction	39
3.2	Cavity geometry	42
3.2.1	General description	42
3.2.2	Paralellism tolerance	46
3.3	Higher-order mode collisions	47
3.3.1	Introduction	47
3.3.2	Higher-order mode avoidance	48
3.3.3	Higher-order mode dampening	51
3.4	Cryogenic cavity design for high roundtrip powers	54
3.4.1	Introduction	54
3.4.2	Material selection	55
3.4.3	Other cryogenic design considerations	58
3.5	Cavity resonator design	59
3.5.1	Linear cavity	59
3.6	Vibration immune cavity mount design	63
3.6.1	3-axis spring mount	67
3.7	Cavity shields and supporting structures	68
3.7.1	Primary shield	68
3.7.2	Secondary shield	70
3.8	Cryocooler assembly, vibration isolation and temperature control	73
3.9	Cavity operation and performance	76
3.9.1	Cryogenic performance	76
3.9.2	Mirror substrates and coating	76
3.9.3	Linewidth of cavity	77
3.9.4	Frequency stability	79
4	Sub-Doppler frequency metrology in HD for test of fundamental physics	81
4.1	Introduction	82
4.2	Experiment	82
4.3	Results and discussion	85
4.3.1	Measurements of the R(1), R(2), and R(3) lines	85
4.3.2	Systematic effects	86
4.4	Conclusion	89

5	Rotational level spacings in HD from vibrational saturation spectroscopy	91
5.1	Introduction	92
5.2	Experiment and results	94
5.2.1	NICE-OHMS experimental layout	94
5.2.2	Asymmetric lineshapes of rovibrational lines in HD	95
5.2.3	Extracting rotational level spacings	97
5.3	Discussion and Conclusion	101
6	Saturation spectroscopy of R(0), R(2) and P(2) lines in the (2-0) band of HD	105
6.1	Introduction	106
6.2	Experiment	107
6.3	Results	107
6.3.1	Vibrational transitions	107
6.3.2	Rotational level separations	109
6.4	Discussion	113
6.4.1	Comparison with QED calculations	113
6.4.2	Dispersive lineshape of R(0)	116
6.5	Conclusion	118
7	Lamb Dip of a Quadrupole Transition in H₂	121
7.1	Introduction	122
7.2	Experiment	123
7.3	Results	125
7.3.1	Lamb dip of a quadrupole transition	125
7.3.2	Recoil doublet in saturation spectroscopy	127
7.3.3	Carrier-Sideband saturation spectroscopy	129
7.4	Conclusion	131
8	Hyperfine structure in a vibrational quadrupole transition of ortho-H₂	133
8.1	Introduction	134
8.2	Experiment	135
8.3	Results	135
8.3.1	Hyperfine resolved Lamb dip measurements	135
8.3.2	Systematic effects	137
8.3.3	Recoil doublet analysis	139
8.4	Discussion	141

8.5	Conclusion	141
9	Precision Measurement of Vibrational Quanta in Tritium Hydride (HT)	143
9.1	Introduction	144
9.2	Experiment	145
9.2.1	Radiation-safe design for tritiated hydrogen	145
9.2.2	NICE-OHMS methodology	146
9.3	Results and discussion	147
9.3.1	Measurements of the R(0) and R(1) lines	147
9.3.2	Lamb peaks in P(1) spectrum	150
9.3.3	Recoil shift	150
9.3.4	Comparison with theory	151
9.4	Conclusion	152
	Bibliography	155
	Dankwoord	175

Introduction and Summary

1.1 The hydrogen molecule as a quantum benchmark

Spectroscopy's role in unveiling the intricacies of hydrogen, first in its atomic form [1] and later also in its molecular form, has been pivotal in advancing our understanding of quantum mechanics. Due to its fundamental simplicity, molecular hydrogen and its isotopologues remain to serve as a cornerstone in the progression of quantum mechanics. This inherent simplicity of hydrogen has catalyzed the development of precise *ab initio* computations grounded in molecular quantum electrodynamics (QED) theory. These computations facilitate rigorous benchmarking of theoretical models against experimental observations, underscoring the integral role of hydrogen in validating and refining quantum mechanical principles.

Ab initio calculations are essential for accurately predicting the electronic and vibrational spectra of hydrogen isotopologues. These theoretical predictions are instrumental in benchmarking the systems, providing a critical testbed for QED within the molecular domain. In the recent decade tremendous progress has been made in this field by the activity of Pachucki, Komasa and Puchalski [2–5]. The current accuracy of *ab initio* calculations enables probing the fundamental constants of nature and to investigate the validity of quantum mechanics at unprecedented levels of precision. Moreover, the agreement of these the-

oretical predictions with experimental data not only validates the robustness of QED but also highlights the potential for discovering new physics beyond the Standard Model (BSM) [6] by probing potential new forces [7] and dimensions that may lie beyond our current theoretical frameworks [8]. Consequently, the elemental simplicity of hydrogen extends beyond its fundamental attributes, serving as a critical instrument for advancing our understanding of fundamental physical principles, as explored through quantum electrodynamics.

Historically, the dissociation energy of the hydrogen molecule stood as the paramount benchmark, with vibrational transitions receiving less attention due to experimental limitations. This benchmarking has primarily focused on comparison between precise measurements and calculations of the dissociation limit of H_2 [9, 10], D_2 [11], and HD [12], reaching an impressive 1 MHz agreement with theory. This remarkable endeavor of benchmarking the dissociation limit spans already over a century, with the first measurement performed by Langmuir [13], and involves intricate experimental tricks to continuously push the accuracy forward. However, the limited lifetimes of the states involved in determining this benchmark value are putting a fundamental limit on future improvement.

1.2 History and future of the rovibrational states

Transitioning from the dissociation energy to the measurement of rotational and vibrational splittings introduces a new dimension of investigation, leveraged by the long lifetimes of these states and the potential for extreme accuracy. However, the pursuit of such measurements has historically been challenged by the inherent weakness of the associated spectral lines. Gerhard Herzberg succeeded to observe the extremely weak quadrupole absorption spectrum of the homonuclear H_2 species [14, 15]. The intricate story of the heteronuclear HD isotopologue, which was also the initial target of this Thesis, started with the observation of its vacuum ultraviolet spectrum [16], achieved soon after the discovery of the hydrogen isotope of mass 2 [17]. Herzberg realized that the inversion symmetry in the heteronuclear HD molecule is broken due to the slight charge asymmetry within the molecule. This marked a pivotal advancement in understanding molecular spectroscopy witnessed

by the observation of dipole rovibrational lines in overtone bands of HD [18]. For both seminal experiments, on the vibrational spectrum of H₂ and HD, he employed high-pressure cells combined with multi-pass absorption techniques. It marked the genesis of quantitative vibrational absorption spectroscopy in hydrogen.

In subsequent decades the rovibrational spectra were measured with refined methods, for H₂ with Fourier-transform spectroscopy [19] and Raman spectroscopy [20]. More refined spectra of HD were recorded for the vibrational overtones [21, 22] and for the pure rotational far-infrared spectrum [23, 24].

These efforts were later complemented by the invention of the laser and advancements in cavity-enhanced techniques. The combined methods, all involving Doppler-limited spectroscopy, were employed for H₂ [25–29], for HD [30, 31] and D₂ [32–34]. Dickenson’s method of measurements of combination differences by exploiting the stronger electronic excitations [35] and Meek’s molecular beam experiment using state-selective ionization [36, 37] have been notable milestones. These methods, based on sub-Doppler configurations, provided innovative pathways to enhance the detection and analysis of weak vibrational transitions, contributing significantly to the field of precision spectroscopy of rovibrational states.

Recently, the playfield of hydrogen isotopologues has been extended further by performing measurements on tritiated species. This activity was carried out at LaserLaB Amsterdam, in collaboration with scientists from the Tritium Laboratory Karlsruhe. Coherent Raman studies of HT, DT and T₂ samples entrained in static gas cells led to improvements on the vibrational spectroscopy of all three species by several orders of magnitude [38–40]. The addition of tritium doubles the possible flavors of molecular hydrogen isotopologues for testing fundamental physics.

The next step of improvement in the rovibrational absorption spectroscopy of hydrogen warrants the acquisition of Doppler-free spectra through saturation spectroscopy. This approach, which was taken as the perspective for the studies laid down in this Thesis, would bring a three orders of magnitude reduction in linewidth, allowing more precise extraction of transition frequencies. This would put the determined rovibrational level structure at the forefront of benchmarking within hydrogen and potentially even with competitive ionic benchmark system [41]. Before this study, no rovibrational transition in any isotope of

hydrogen was ever observed under conditions of saturation due to their inherent weakness. Here, by the latest advancements in cavity and laser technology were combined and applied via the spectroscopic technique of Noise-Immune Cavity-Enhanced Optical Heterodyne Molecular Spectroscopy (NICE-OHMS). NICE-OHMS was selected as it has proven to be the most sensitive absorption technique under conditions of saturation with near shot-noise limited performance [42, 43]. Another novelty of the present work is to combine the extremely sensitive NICE-OHMS method with frequency comb calibration - combining extreme sensitivity with extreme frequency accuracy.

The field of Noise-Immune Cavity-Enhanced Optical Heterodyne Molecular Spectroscopy (NICE-OHMS), invented by Hall and coworkers [44], is a cavity-enhanced spectroscopic technique, somewhat similar to Cavity Ring-Down Spectroscopy (CRDS), invented by O’Keefe and Deacon [45] for pulsed operation, and later by Romanini et al. [46] for CW operation. Several reviews have been written on the wide variety of such techniques explored [47–49]. The specific variant of NICE-OHMS is able to reduce the noise equivalent absorption (NEA) level close to the absolute noise limit; the photon shot noise, allowing extraction of the full potential of cavity-enhanced spectroscopy.

Chapter 4 of this thesis represents our genesis study, the first implementation of NICE-OHMS in our laboratory, and describes the successful observation and measurement of the saturated absorption spectra of the first overtone dipole transition in HD. These results were, simultaneously obtained with the work of the Hefei group [50] and resulted in a puzzling 4-sigma discrepancy. This sparked many studies and resulted in an underlying puzzling lineshape. However, no definite solution to this lineshape conundrum has yet been found, although several ideas have been presented [51–53].

The success of achieving saturation of the weakest transition so far led us to the idea of saturating a rovibrational quadrupole transition in para- H_2 . As this is a hyperfineless transition, the potential influence of the hyperfine on the lineshape is absent. The two orders of magnitude lower transition moment compared to the dipole transitions in HD required the development of a sophisticated new setup, in which high laser power, a cryogenic narrow linewidth cavity, and a new novel implementation of NICE-OHMS were all combined.

1.3 Summary

The remainder of this PhD Thesis is separated into two parts. Chapters 2 and 3 describe the design and construction of the experimental layout that was used in the experiments, while chapters 4 through 9 present a sequence of studies on the spectroscopy of HD, H₂, and HT.

Chapter 2 introduces and describes our sophisticated NICE-OHMS implementation used in our latest experiments. Our implementation is based on fully digital parallel demodulation using a high-speed digital lock-in amplifier, allowing robust and repeatable acquisition. Several tricks to reduce or eliminate background signal drifts are discussed and implemented to allow long-term averaging. A novel method of carrier locking symmetrization was implemented, which allowed prolonged measurements near the quantum noise limit. This was combined with frequency comb locking, providing absolute frequency calibration.

Chapter 3 describes the design and development of a vibration-insensitive cryogenic cavity suitable for high-power saturation spectroscopy. This section covers the technical design aspects, such as cavity geometry, higher-order mode avoidance, material selection and the integration of cryogenic technology.

Note that not all methods and tricks discussed in Chapters 2 and 3 were present or included in all of the following spectroscopy studies mentioned. The setup used in Chapter 4 was the first realization of a NICE-OHMS setup in our laboratory with an initial cavity configuration and signal recovery scheme. From Chapter 5 and onwards the full digital demodulation scheme was implemented. From Chapter 6 a transition to the cryogenic cavity was made and the free-space EOM was implemented. The active PDH setpoint stabilization was only used in Chapter 7 and 8. For Chapter 9 a third cavity was built, in collaboration with the Tritium Laboratory Karlsruhe, directed at radiation safety for the use of tritium gas; this cavity operated only at room temperature. After the initial study of HD in Chapter 4 this isotopologue was further investigated in Chapters 5 and 6, focusing on the determination of rotational level spacings. This was done by using combination differences of obtained sub-Doppler spectra of rovibrational transitions. This partially overcomes the intricate lineshape problem encountered in saturated spectra of HD.

Chapter 7 marks the first-ever observation and measurement of a rovibrational quadrupole transition under conditions of saturation in hy-

drogen or any neutral molecule. Not only does this mark a new era in saturation spectroscopy, but its symmetric Lamb dip spectra set the most accurate benchmark transition to date in any isotope of hydrogen. Chapter 8 further explores the hydrogen molecule by saturation of the Q(1) transition in ortho-H₂, successfully exposing the underlying hyperfine structure. This shows the remarkable resolution obtained by saturation spectroscopy and marks the first quantitative study of the hyperfine spectrum in the optical domain for molecular hydrogen.

Chapter 9 concludes the experimental investigation with precision measurements of vibrational quanta in tritium hydride (HT). This study required the development of a sophisticated gas loading scheme and radiation-safe measurement setup. The more favorable hyperfine structure compared to HD allowed extraction of the underlying substructure and put the tritiated isotopes back at the forefront of benchmarkable systems within hydrogen.

1.4 Concluding remarks and outlook

This journey from Herzberg's initial measurements to the latest sub-Doppler spectroscopic achievements underscores the remarkable evolution of rovibrational spectroscopy of hydrogen. These advancements have not only led to the most accurate benchmark values in hydrogen to date but also highlight substantial potential for future improvements. The exceptionally long lifetimes of the states involved, combined with their extremely narrow natural linewidths, provide ample opportunity for further refinement, promising even greater precision in the measurement of rovibrational transitions. This reaffirms molecular hydrogen's prominence as a future benchmark system in precision spectroscopy.

This thesis has focused on precision measurements of the level structure of the simplest molecule, testing the underlying theory of quantum electrodynamics that describes its quantum structure. Concurrently, it represents a study in the advancement of optical technology, achieving record sensitivities. Notably, we have measured in saturation a single hyperfine component of the Q(1) quadrupole transition in the (2-0) band of H₂, with a line strength as low as 4.4×10^{-28} cm/molecule.

Despite these significant achievements, further progress necessitates a deeper understanding of the underlying dynamics causing the encountered and currently unexplainable lineshapes, particularly for the het-

eronuclear isotopes of hydrogen (HD and HT in this study). Further progression in accuracy in these isotopes is presently hindered by the absence of a general model to reliably extract transition frequencies. The compact underlying hyperfine spectrum complicates the lineshape further; thus, a full resolution of the hyperfine structure is essential for a comprehensive understanding of the underlying dynamics. In the case of the homonuclear isotope H_2 , symmetric Lamb dips of quadrupole transitions have been observed under specific experimental conditions, marking a promising path toward further improvement.

Experimentally, our results also indicate a fundamental limit in the progression of saturation spectroscopy due to the photon shot noise limit. The near shot-noise-limited performance of the current experiment permits only minor incremental improvements through further noise reduction, suggesting that additional experimental progress must be sought through alternative avenues. Enhancing sensitivity by increasing the effective optical path length faces experimental constraints: both the finesse and cavity length cannot be significantly scaled, as the finesse is limited by material properties and scaling the cavity length introduces disproportionate experimental challenges.

A clear path forward lies in significantly increasing the interrogation time of the spectroscopy laser with the molecules under study. This strategy would result in narrower linewidths and eventually enable full resolution of the hyperfine structure in the heteronuclear isotopes. Repeating the current experiments at temperatures lower than 72 K will help in this endeavor, but with an experimental lower limit of around 4 K by using buffer gas cooling again a limit is faced. Expanding the intracavity beam size is another solution to increase the interrogation time, but this too is hindered by the disproportionate extreme tolerances required in angular alignment of the mirrors. Ultimately, achieving full trapping of the hydrogen molecule is necessary to fully exploit the potential of its long-lived rovibrational states.

As a final remark; it is imperative that both theory and experiment of the hydrogen molecule attain comparable levels of accuracy to serve as a proper benchmark system. Historical precedent suggests that theoretical breakthroughs are always on the horizon, and it is probably only a matter of time before theory and experiment are in competition once again.

Frequency comb referenced NICE-OHMS for saturation spectroscopy of extremely weak rovibrational transitions

2.1 Introduction

Noise-Immune Cavity-Enhanced Optical Heterodyne Molecular Spectroscopy (NICE-OHMS) is an extremely sensitive spectroscopic technique invented and pioneered in the late 90's by J.L. Hall and his co-workers [43, 44]. In its essence it is performing frequency modulation spectroscopy (FMS) within an enhancement cavity, which combines both the benefit of path length enhancement from the cavity and the extreme noise reduction of FMS. The sensitivity and potential of NICE-OHMS were directly shown in these first studies, where an impressive noise level of only 30% above the shot-noise limitation was achieved. This resulted in a detection sensitivity of $5 \times 10^{-13} \text{ Hz}^{-1/2}$, which set the record and benchmark value as the most sensitive cavity-enhanced absorption spectrometer for the decades to come. NICE-OHMS was originally developed

2. FREQUENCY COMB REFERENCED NICE-OHMS FOR SATURATION SPECTROSCOPY OF EXTREMELY WEAK ROVIBRATIONAL TRANSITIONS

with the potential to serve as an optical frequency standard, as optical standards were limited during that period of time. This can be achieved by stabilizing the cavity and its respective laser onto a Doppler-free narrow molecular resonance through saturation spectroscopy, as NICE-OHMS is able to provide a dispersive signal of the molecular transition which can be used as an error signal. However, the realization of the frequency comb laser shortly after made the need for secondary optical frequency standards less stringent as a direct conversion between the existing primary standards in the RF domain and the optical domain was ensured. Despite its impressive sensitivity, the onset of the frequency comb era combined with the relative technical complexity of NICE-OHMS limited further progression and uptake within molecular spectroscopy for some time.

The somewhat limited uptake is also due to the great success of cavity ring-down spectroscopy (CRDS) [45], which is another leading technique of cavity-enhanced spectroscopy. CRDS is an absolute workhorse within molecular spectroscopy due to its relative simplicity and theoretically nearly identical shot-noise limited performance as NICE-OHMS [54]. A strong benefit of CRDS is that it directly measures the absolute absorbance of the molecular transition, which directly gives a measure of its linestrength; a crucial parameter for most molecular studies. While NICE-OHMS is capable of measuring the absorbance, it relies on several instrumental parameters to retrieve the absolute absorbance. CRDS is also better suited for Doppler-broadened spectroscopy compared to NICE-OHMS, as some background noise reduction methods are less effective or impossible when measuring in wider frequency ranges with NICE-OHMS [54].

A new period of increasing NICE-OHMS implementation started around 2006, when the group of Axner and co-workers started a series of experiments which led to significant development on the technical aspects of NICE-OHMS [55–59]. The Umea group benefitted from the development of fiber technology [60–62], which significantly simplified the realization of NICE-OHMS. The main focus was Doppler-broadened spectroscopy, where the main goal was applying the sensitivity of NICE-OHMS as a potential method for trace gas detection [63, 64]. Another noteworthy example are the experiments in the group of McCall, where an adaptation of NICE-OHMS was used called NICE-OHVMS. Here, VM stands for velocity modulation, where ionic radicals were velocity modulated inside a cavity using electric fields [65, 66]. Also, the im-

plementation of NICE-OHMS on trapped atoms is noteworthy [67]. All these experiments show the versatility of NICE-OHMS.

NICE-OHMS mainly excels at Doppler-free saturation spectroscopy on extremely weak rovibrational lines, the main target for the present studies in this Thesis. This is due to the fact that NICE-OHMS operates continuously at constant intensity, which is a crucial aspect for non-linear spectroscopy such as saturation spectroscopy. Moreover, since the linewidths of saturated transitions are typically less than a MHz, the dominating origin of noise within NICE-OHMS can be effectively removed. This has also been supported by the studies so-far, as most implementations of NICE-OHMS have been on saturated lineshapes with a main focus on the development of frequency standards [68–71]. However, none of these previously mentioned experiments were able of surpassing the sensitivity achieved in the original realization in the group of J.L. Hall, which shows the subtleties involved of implementing this method. Despite the technical complexity and delicacy of the method involved, we selected NICE-OHMS for our experiments of saturation spectroscopy on extremely weak rovibrational lines, as it exhibits the best properties for these anticipated measurements.

The remainder of this chapter will first give a general overview of NICE-OHMS applied to saturation spectroscopy. Thereafter, the technical implementation of NICE-OHMS within our experiment will be presented. Here, all novelties used in our implementation will be discussed which led to the record sensitivity to measure a quadrupole transition under conditions of saturation.

2.2 NICE-OHMS principles

2.2.1 Frequency modulation spectroscopy formalism

As NICE-OHMS is essentially a successful combination of frequency modulation spectroscopy (FMS) and cavity enhancement, it follows the same formalism as FMS. FMS is a technique invented by Bjorklund [72], which allowed shot-noise limited absorption sensitivity due to the noise-immune characteristics of the heterodyne detection. Within FMS, the electric field of the laser (the carrier at frequency ν_c) is modulated by a frequency ν_{mod} , which results in the following description of the electric field

2. FREQUENCY COMB REFERENCED NICE-OHMS FOR SATURATION SPECTROSCOPY OF EXTREMELY WEAK ROVIBRATIONAL TRANSITIONS

$$\tilde{E}^{fm}(\nu_c, t) = \frac{E_0}{2} \hat{\mathbf{e}} e^{i[2\pi\nu_c t + \beta \sin(2\pi\nu_{\text{mod}} t)]} + \text{c.c.} \quad (2.1)$$

Here, E_0 is the field amplitude, $\hat{\mathbf{e}}$ a vector representing the direction of polarization, β the modulation index, a measure of the extent of modulation imposed on a carrier signal, and c.c. the complex conjugate. For the limit of small modulations ($\beta \leq 0.5$), the modulated field mainly consists of two sidebands next to the carrier, thus the previous equation can be rewritten using only the first order sidebands as

$$\begin{aligned} \tilde{E}^{fm}(\nu_c, t) = \frac{E_0}{2} \hat{\mathbf{e}} & [J_0(\beta) + J_1(\beta)e^{i2\pi\nu_{\text{mod}} t} \\ & - J_1(\beta)e^{-i2\pi\nu_{\text{mod}} t}] e^{i2\pi\nu_c t} + \text{c.c.}, \end{aligned} \quad (2.2)$$

where $J_0(\beta)$ and $J_1(\beta)$ are the zeroth and first-order Bessel functions, which describe the amplitude of carrier and sidebands respectively. This essentially describes a frequency triplet, which consists of the carrier wave with two balanced out-of-phase sidebands spaced at ν_{mod} . This expression also shows that when no disturbance is present, the heterodyne beat signals of the two individual sidebands with the carrier will cancel each other. Thus, no signal is present when an absorber is absent. The presence of a molecular absorber causes a disturbance to the balanced triplet, of which the transmitted electric field can be described as [58]

$$\begin{aligned} \tilde{E}_T^{fm}(\nu_c, t) = \frac{E_0 \hat{\mathbf{e}}}{2} & \left[\hat{T}_0(\nu_c) J_0(\beta) + \hat{T}_1(\nu_c) J_1(\beta) e^{i2\pi\nu_{\text{mod}} t} \right. \\ & \left. - \hat{T}_{-1}(\nu_c) J_1(\beta) e^{-i2\pi\nu_{\text{mod}} t} \right] e^{i2\pi\nu_c t} + \text{c.c.} \end{aligned} \quad (2.3)$$

Here, $\tilde{T}_j(\nu_c) = \exp[-\delta_j(\nu_c) - i\phi_j(\nu_c)]$ is the complex transmission function of the molecular absorber, in which $\delta_j(\nu_c)$ and $\phi_j(\nu_c)$ are the amplitude attenuation and the optical phase shift of the electric field at frequency $\nu_j = \nu_c + j\nu_{\text{mod}}$, where $j = 0, \pm 1$, respectively. In the limit of low absorption, the intensity of the modulated field contains a term oscillating at the modulation frequency and can be written as

$$\begin{aligned}
 \tilde{I}_T^{fm}(\nu_d, t) &= 2I_0 J_0(\beta) J_1(\beta) \\
 &\times \{ [\phi_{-1}(\nu_d) - 2\phi_0(\nu_d) + \phi_1(\nu_d)] \sin(2\pi\nu_m t) \\
 &+ [\delta_{-1}(\nu_d) - \delta_1(\nu_d)] \cos(2\pi\nu_{\text{mod}} t) \}, \quad (2.4)
 \end{aligned}$$

where I_0 is the intensity of the incident light before the molecular absorber. Here, also the detuning of the laser (ν_d) with respect to the transition center (ν_0) is introduced, thus $\nu_d = \nu_0 - \nu_c$. This equation contains two different signal components differing in phase. The sine term is called the in-phase component as it is in-phase with the applied modulation. This term is proportional to the difference between the phase shift experienced by the carrier and the average phase shift by the sidebands. The cosine term, which is orthogonal in phase, is called the out-of-phase component. This term is proportional to the difference of the attenuation of the two sidebands. The final FMS signal can be obtained by phase-sensitive demodulation by the modulation frequency and results in a DC signal described by

$$\begin{aligned}
 \mathcal{S}_T^{fm}(\nu_d, \theta_{fm}) &= \eta P_0 J_0(\beta) J_1(\beta) \\
 &\times \{ [\phi_{-1}(\nu_d) - 2\phi_0(\nu_d) + \phi_1(\nu_d)] \cos \theta_{fm} \\
 &+ [\delta_{-1}(\nu_d) - \delta_1(\nu_d)] \sin \theta_{fm} \}, \quad (2.5)
 \end{aligned}$$

where θ_{fm} is the demodulation phase, $\eta(V/W)$ is the photodetector and amplifier responsivity, and P_0 the total laser power incident on the photodetector.

2.2.2 Cavity-enhanced saturation spectroscopy

Now in addition, we have a linear cavity that exhibits discrete resonance modes. The mode spacing, or the free spectral range (FSR) is given by

$$\nu_{\text{FSR}} = \frac{c}{2nL_c}, \quad (2.6)$$

where c is the speed of light, n the index of refraction, and L_c the cavity resonator length. In order to couple in the generated frequency triplet to perform FMS within the cavity, the modulation frequency must be equal to the FSR ($\nu_{\text{mod}} = \nu_{\text{FSR}}$). If this primary condition for NICE-OHMS is fulfilled, the cavity will provide additional enhancement to the

2. FREQUENCY COMB REFERENCED NICE-OHMS FOR SATURATION SPECTROSCOPY OF EXTREMELY WEAK ROVIBRATIONAL TRANSITIONS

signals acquired with FMS, which is defined by the enhancement factor $2F/\pi$. Here, F is the finesse of the cavity which can be approximated by

$$F \approx \frac{\pi R^{-1/2}}{1 - R}, \quad (2.7)$$

where R is the reflectivity of the mirrors. This approximation is valid for $R \gg 0.5$ and when both mirrors have equal reflectivity. Thus enhancement factors of up to or over 10^5 can be expected by modern cavity mirrors.

NICE-OHMS can be used in both Doppler-broadened and sub-Doppler spectroscopy, and studies have been executed in both domains. In our studies, we will solely focus on sub-Doppler spectroscopy on a Doppler-free Lamb dip obtained through saturation spectroscopy. Saturation spectroscopy is well facilitated within linear enhancement cavities due to the power enhancement inside a cavity and the perfectly overlapping counter-propagating beams, excluding any residual first-order Doppler effect.

Due to the allowable combinations of the carrier and sidebands, there is a total of 9 combinations where two counter-propagating waves may interact with the same velocity class of molecules. This results in a total of 5 distinctive frequency locations at where sub-Doppler signals may occur within NICE-OHMS [58], specifically at the frequency detunings $\nu_d = 0, \pm\nu_{\text{mod}}/2, \pm\nu_{\text{mod}}$. For the studies outlined in this Thesis we will primarily focus on the main resonance located at $\nu_d = 0$, corresponding to carrier-carrier saturation. Except in the study of the H_2 quadrupole in Chapter 7 a different saturation scheme will be exploited, which will be described in that specific chapter.

The consequence of only considering the central Lamb dip originating from the carrier-carrier saturation is that only the in-phase dispersion component of the carrier in Eq. (2.5) contributes to the NICE-OHMS signal. If we now simplify this equation and also include the cavity enhancement, we obtain a description of the NICE-OHMS signal for carrier-carrier saturation which can be written as

$$\mathcal{S}_T^{NO}(\nu_d, \theta_{fm}) = \frac{4F}{\pi} \eta P_0 J_0(\beta) J_1(\beta) \phi_0(\nu_d) \cos \theta_{fm} \quad (2.8)$$

Now $\phi_0(\nu_d)$ is the only term remaining, which is the optical phase shift induced by the transition and describes to observed lineshape.

Thus, NICE-OHMS is only capable of measuring the dispersion of a sub-Doppler transition when considering saturation spectroscopy at the center of the transition and results in a dispersive lineshape.

The observed lineshape within saturation spectroscopy is typically constructed of two individual resonances as the optical pumping involved in saturation spectroscopy actually causes the formation of two Lamb dips, the so-called recoil doublet. This will be further explained in Chapter 7. The formation of the recoil doublet has been observed in numerous atomic experiments but only has been resolved in three experiments within molecular systems, all in methane [73–75]. Ordinarily, the recoil doublet splitting is significantly smaller than the typical transition linewidth in molecular spectroscopy, making it impossible to resolve. However, the general consensus is that a recoil doublet of equal intensity is present and that no recoil shift must be applied for saturated lineshapes.

The typical linewidths experienced in cavity-enhanced saturation spectroscopy are mainly dictated by pressure broadening, power broadening, and transit-time broadening [76]. The long lifetimes of the upper states of these weak transitions are typically an insignificant contribution to the linewidth. For sufficiently low power and pressure, the obtained linewidth (FWHM) is mostly limited by the transit-time broadening and is given by [77, 78]

$$\Delta\nu_t = \frac{1}{4} \frac{\hat{v}}{w_0}. \quad (2.9)$$

Here, $\hat{v} = (2k_B T/M)^{1/2}$ is the most probable molecular velocity, and w_0 is the waist size radius of the cavity. For most typical systems, this results in typical transit-time limited linewidths between 100 to 1000 kHz, depending on the temperature, molecular mass, and waist size. While this is often a lower limit, some experiments (also in this Thesis) have observed linewidths below the transit time under conditions of extremely weak saturation [43].

All effects discussed contribute to homogeneous broadening, thus the observed lineshape within NICE-OHMS when performing saturation spectroscopy is a dispersive Lorentzian.

2.2.3 Wavelength modulation

In addition to the fast phase modulation at $\nu_{\text{mod}} = \nu_{\text{FSR}}$, a second slower wavelength modulation can be applied to remove remaining low-frequency noise and slow varying baseline drifts. This is particularly effective within saturation spectroscopy, as the linewidths of interest are significantly smaller than the expected baseline features, which will be further discussed in subchapter 2.3.

Wavelength modulation within NICE-OHMS is typically implemented by modulating the cavity length at a frequency (f_{wm}) smaller than the linewidth of the cavity. This additional modulation can be retrieved within a lock-in amplifier after the high-frequency demodulation step of the in-phase dispersion component at ν_{mod} . If the modulation amplitude is well within the linewidth of interest to not significantly alter the retrieved signal and lineshape, the action of the wavelength modulation can be considered a derivative of the original lineshape, depending on the selected order of demodulation (harmonic) (Fig. 2.1). Demodulation within the lock-in can be done at any desired harmonic, which all have their distinctive characteristics. The narrower lines at $3f$ can be used for unraveling spectroscopic substructure as was shown for the case of hyperfine structure in the H_2^{17}O [79]. In the studies outlined in this Thesis, only the $1f$ signal is used as it provides the best signal-to-noise level for weak signals. The typical Lorentzian lineshape expected for the $1f$ demodulation is provided by

$$f_{1f}^{\text{disp}}(\nu_d) = \frac{4A[\Gamma^2 - 4\nu_d^2]}{[\Gamma^2 + 4\nu_d^2]^2}, \quad (2.10)$$

where A is the amplitude of the signal and Γ the half-width of the transition. In some literature, the addition of wavelength-modulation is referred to as *wm-NICE-OHMS*, but we consider it an essential part of NICE-OHMS and assume wavelength-modulation is always present. If we refer to the NICE-OHMS signal in absence of wavelength-modulation we refer to it as the *direct NICE-OHMS* signal.

2.2.4 Typical implementation of NICE-OHMS

NICE-OHMS requires laser locking to optical cavities, for which primarily Pound-Drever-Hall (PDH) stabilization is used. The PDH technique also works through phase-sensitive heterodyne detection, thus also re-

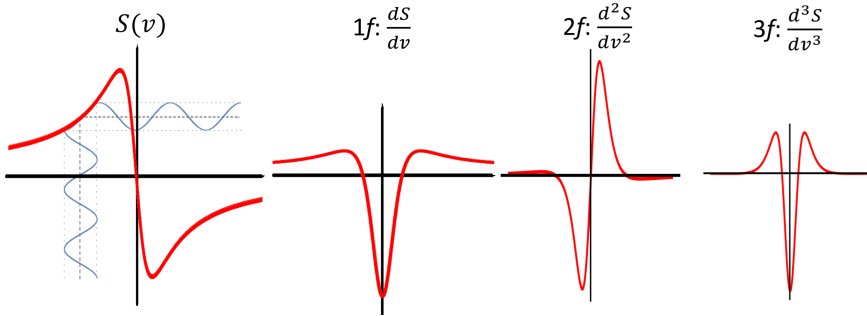


Figure 2.1: The characteristic sub-Doppler signals of the central carrier-carrier saturation within NICE-OHMS. The leftmost signal, $S(\nu)$, is the dispersive direct NICE-OHMS signal, which typically follows a dispersive Lorentzian lineshape. The applied wavelength modulation is visible in blue, which causes additional modulation of the signal amplitude and allows derivative detection. Shown are the typical lineshapes for the 1st, 2nd, and 3rd harmonic of detection. Typically the 1st harmonic ($1f$) is used for most sub-Doppler spectroscopy studies in this Thesis.

quiring a pair of sidebands at frequency ν_{PDH} which falls typically in the range 10 - 20 MHz. The applied modulation at ν_{PDH} in combination with the necessary modulation for the NICE-OHMS signal at ν_{mod} , results in the formation of additional sidebands at the sum and difference frequencies at frequencies $\nu_{\text{mod}} \pm \nu_{\text{PDH}}$. Thus, in total 4 pairs of sidebands emerge next to the carrier (see Fig. 2.2).

Stabilizing the modulation frequency onto the FSR of the cavity can be done through several methods. In the original realization by Ye *et al.* a dither onto the modulation frequency ν_{mod} was applied to perform derivative detection of the transmitted power after the cavity through a lock-in amplifier to acquire an error signal. In later realizations of NICE-OHMS the method derived by deVoe-Brewer (dVB) [80] was implemented. Within this method a PDH-like error signal is generated for the pair of NICE-OHMS sidebands with their respective cavity mode, which can be used to feedback ν_{mod} . The error signal can be retrieved at frequencies $\nu_{\text{mod}} \pm \nu_{\text{PDH}}$, thus forming a beat signal with the NICE-OHMS sidebands and either the closest or furthest spaced original PDH sideband. Both the PDH and dVB error signals are retrieved in the same photodetector in reflection.

An overview of a typical NICE-OHMS implementation is given in Fig. 2.2. After both the carrier and sidebands are locked to the cavity through the PDH and FSR stabilization (either through the dVB method or

2. FREQUENCY COMB REFERENCED NICE-OHMS FOR SATURATION SPECTROSCOPY OF EXTREMELY WEAK ROVIBRATIONAL TRANSITIONS

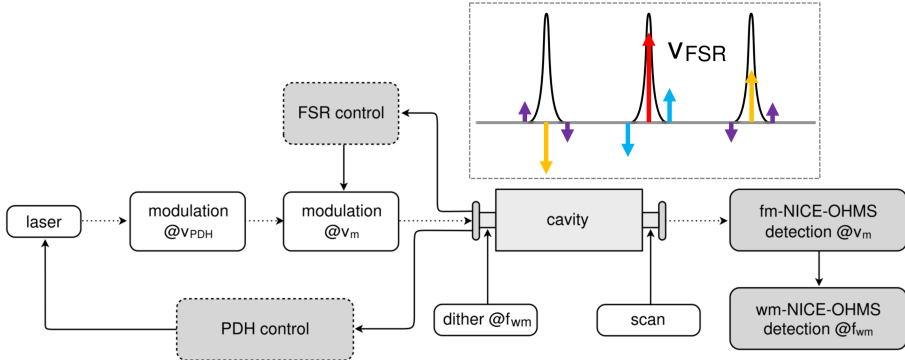


Figure 2.2: Schematic overview of a typical NICE-OHMS setup adapted from Axner *et al.* [58]. Visible are the two applied modulations at ν_{PDH} and ν_{mod} , produced within a single or two separate EOM stages. This results in a pair of sidebands next to the carrier (light blue) from the modulation at ν_{PDH} and a pair of sidebands at the adjacent cavity mode (yellow) from the modulation at ν_{mod} . In addition, sidebands from the sum and difference frequencies at $\nu_{\text{mod}} \pm \nu_{\text{PDH}}$ are generated as well (purple), which results in a total of 4 pairs of sidebands. The ν_{PDH} (blue) and $\nu_{\text{mod}} \pm \nu_{\text{PDH}}$ (purple) sidebands will be reflected from the cavity and are used to generate the necessary error signals to lock the carrier to its respective cavity mode through the PDH locking technique and the two spectroscopy sidebands at ν_{mod} with their respective cavity modes through the deVoe-Brewer technique. Next to the fast phase modulation, a slow dither modulation (f_{wm}) at one of the cavity mirrors to perform wavelength modulation to allow derivative detection is often applied within NICE-OHMS. A signal can be acquired by scanning the carrier through a molecular resonance by tuning the cavity length. The NICE-OHMS signal is observed in transmission of the cavity by phase-sensitive demodulation at ν_{mod} , and subsequently demodulation at f_{wm} within a lock-in amplifier.

via an alternative solution), the requirements to perform FMS within a cavity are fulfilled. The frequency triplet is detected in transmission by a high-speed photodetector, after typically first the signal is demodulated at the high-frequency component (ν_{mod}), which provides the direct NICE-OHMS signal. If a dither is applied to the piezo of the cavity, the remaining wm-modulation on the direct NICE-OHMS signal can subsequently be demodulated within a lock-in amplifier to obtain the derivative signal(s), as shown in Fig. 2.1.

2.3 Residual amplitude modulation

2.3.1 Introduction

NICE-OHMS has extremely good noise suppression from any remaining technical noise from the laser, as this is present as common mode modulation on the frequency triplet and thereby will be effectively canceled. However, it is very susceptible to noise causing modulation of individual components on either carrier or one of the sidebands. This type of noise is generally called residual amplitude modulation (RAM). RAM is unwanted modulation or drift on the amplitude or phase balance of the carrier or individual sidebands. As this directly affects the heterodyne beat, RAM will directly cause an increase in background noise or background signal drift.

The source of RAM can be anything that causes dispersion or frequency-dependent attenuation, such as weak etalons, (anomalous) dispersion and absorption by a secondary absorber in the beam path, and asymmetric generation of the sidebands. As the EOM is the source of the sidebands, it is both the starting point of potential RAM pick-up in the remaining beam path and also one of the largest potential sources of RAM. RAM can be created within the EOM by generating unbalanced sidebands due to electric field asymmetry, to a polarization mismatch, or through a formed etalon within the crystal itself. Especially in fiber EOM's the more limited control of the input polarization state and the unavoidable etalons from perfectly aligned fiber interfaces is typically noticeable [81].

2.3.2 RAM originating from the EOM

Several strategies have been developed to reduce or eliminate origins of RAM within EOM's, where a free-space EOM is preferred thanks to the availability of AR coatings to avoid reflective crystal-to-fiber interfaces in fiber EOM's. Next to that, a free-space EOM allows a higher degree of control of the polarization input state, to which an EOM is extremely sensitive. Other strategies involved to reduce RAM are the use of an angled back surface of the crystal to deflect the unwanted polarization state [82], precise temperature control due to temperature sensitivity of the crystal, and the use of an additional DC bias field on top of the RF field [83]. Free-space EOM's have an additional complexity as the

2. FREQUENCY COMB REFERENCED NICE-OHMS FOR SATURATION SPECTROSCOPY OF EXTREMELY WEAK ROVIBRATIONAL TRANSITIONS

larger-sized crystal requires an RF resonant circuitry to amplify the input electric field to acquire sufficient modulation depth. This typically means that an EOM can only operate at one distinctive modulation frequency, requiring two separate EOM stages for both the PDH and FSR sidebands within NICE-OHMS. This gives unwanted complexity to the optical beam layout and gives rise to additional potential sources of RAM. Therefore, we made use of a custom-built double resonant EOM (QUBIG GmbH PMd-20/400L3-SWIR), which allowed simultaneous modulation of both the PDH and FSR sidebands in a singular device. To counteract all potential sources of RAM, the EOM is also outfitted with an AR coating, an angled output surface to deflect the different polarization states, and precise temperature control.

2.3.3 Residual etalons causing RAM

The other dominant source of RAM is the formation of etalons in the optical beam path, potentially caused by any optical element that requires transmission [84]. The first approach is to reduce the amount of transmissive surfaces after the EOM to a minimum. For example, the necessary mode-matching stage requiring lenses can be put before the EOM stage, or off-axis parabolic mirrors can be used. For the remaining components, the effect of etalons can be significantly reduced by using proper AR coatings and placing these components under a small angle with respect to the laser beam to avoid overlap of the back reflection. However, some components only allow a small angular tilt due to a limited acceptance angle or are required to be at normal incidence, such as the EOM crystal entrance surface and cavity mirrors. The first strategy to significantly dampen the amplitude of these etalons is by the use of optical isolators within the path of the present etalon, which effectively breaks up these etalons. However, an optical isolator exhibits multiple transmissive surfaces for its operation and thus can be a potential source of a new weaker etalon. Thus ultimately some level of etalons will be present within the setup, for which multiple strategies can be implemented to reduce its resulting effect.

Already in the early studies by the group of Bjorklund it was discovered that modulating at a specific frequency significantly reduced the effect of present etalons by matching the modulation frequency to the FSR of the present etalon [85]. However, within NICE-OHMS the modulation frequency is determined by the FSR of the enhancement cavity, thus

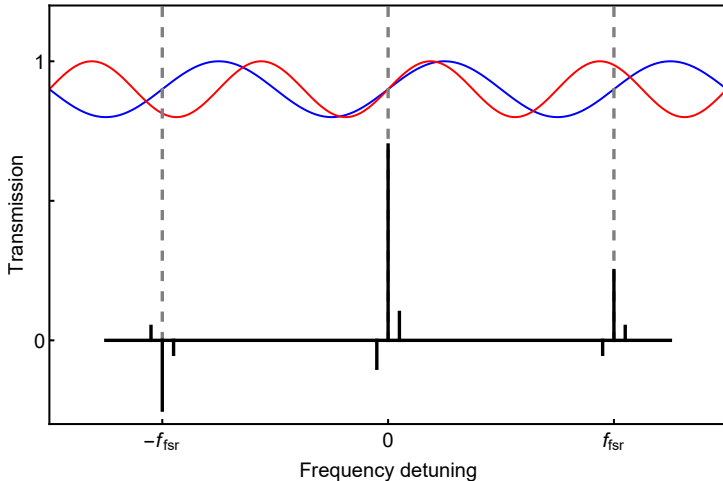


Figure 2.3: Effect of weak etalons present in the setup on the modulated sidebands, causing residual amplitude modulation. Shown in red is an etalon with an FSR at $0.75 \times \nu_{\text{mod}}$, which causes different modulation of each individual frequency component when the etalon starts drifting. Shown in blue is an etalon with an FSR at exactly ν_{mod} , the etalon immune distance, and causes merely common mode modulation of the carrier and ν_{mod} sidebands. However, some level of modulation from etalons will always remain on the ν_{PDH} and $\nu_{\text{mod}} \pm \nu_{\text{PDH}}$ sidebands.

optimization of the modulation frequency is not possible. This led to the concept of etalon immune distances, where the component spacing is matched to an integer value of the cavity length and thus the modulation frequency [86]. The etalon immune distance is defined by $L_{\text{EID}} = q \cdot L_{\text{cav}}$, where q is an integer and L_{cav} is the cavity length. When the component spacing is equal to the etalon immune distance, the modulation of the etalon will be present as common mode modulation of the triplet (see Fig. 2.3). The study of Ehlers *et al.* [86] showed that optimizing the spacing between the output cavity mirror and measurement photodiode resulted in almost an order of magnitude improvement of detection sensitivity through the reduction of drifting background signal from the resulting etalon. This shows the sensitivity and delicacy involved of protecting the modulated triplet of any unwanted disturbance.

While the use of these previous strategies will significantly reduce both the peak-to-peak amplitude of the etalons and its resulting effect on the NICE-OHMS triplet, some level of residual etalons will remain as exact etalon immune distances of all optical interfaces are impossible to achieve. Fortunately, the usual implemented wavelength modulation for

2. FREQUENCY COMB REFERENCED NICE-OHMS FOR SATURATION SPECTROSCOPY OF EXTREMELY WEAK ROVIBRATIONAL TRANSITIONS

the derivative detection is very effective to further reduce the effect of these remaining etalons when performing saturation spectroscopy. This is due to the fact that the expected etalon FSR is typically on the order of over 100 MHz, depending on the component spacing, while the expected linewidths of saturated transitions are typically sub-MHz. Therefore, the weak and nearly linear slope in the measurement range of interest mostly contributes to a constant offset in the signal. However, etalons typically drift in time which will cause either a varying constant baseline or higher order quadratic baseline, depending on the measurement speed and etalon drift. Thus further reduction of the effect of the remaining etalons is warranted when long averaging near the shot-noise limit is desired.

Reduction of the impact of the residual etalons can be achieved by reducing the drift rate of the etalons through thermal stabilization and insulation to reduce higher-order effects on the baseline of the measured signal. However, even for slow drifts, the background signal will still experience the same peak-to-peak variation as the amplitude and maximum slope of the sinusoidal fringe will remain similar. The peak-to-peak amplitude variation of the baseline is determined by the maximum slope of the etalon, which is halfway at either side of the fringe and is spaced by half its respective FSR. This means that for any etalon of any size, the maximum peak-to-peak variation is obtained by a length drift of half the operating wavelength of the laser. Thus stabilization of the etalon length to less than half a wavelength variation will start to lead to reduction of the peak-to-peak amplitude of the baseline variation, but the resulting effect of this stabilization depends on the absolute frequency location of the etalon in question.

2.3.4 Methods of reducing impact of etalons

Let us consider the worst-case scenario for the dispersion mode of measurement, which is at the top of the etalon fringe. Here, the derivative of the phase change experiences the maximum slope also assume we can stabilize well within a single fringe width. We can make a first-order Taylor expansion of the nearly sinusoidal etalon with a certain amplitude A . This expansion results in $A\Delta x$, where Δx is the resulting peak-to-peak length drift. The dominant origin of length drift is the temperature variation and its resulting effect on the thermal expansion of the breadboard on which the optical components are mounted. Thus if

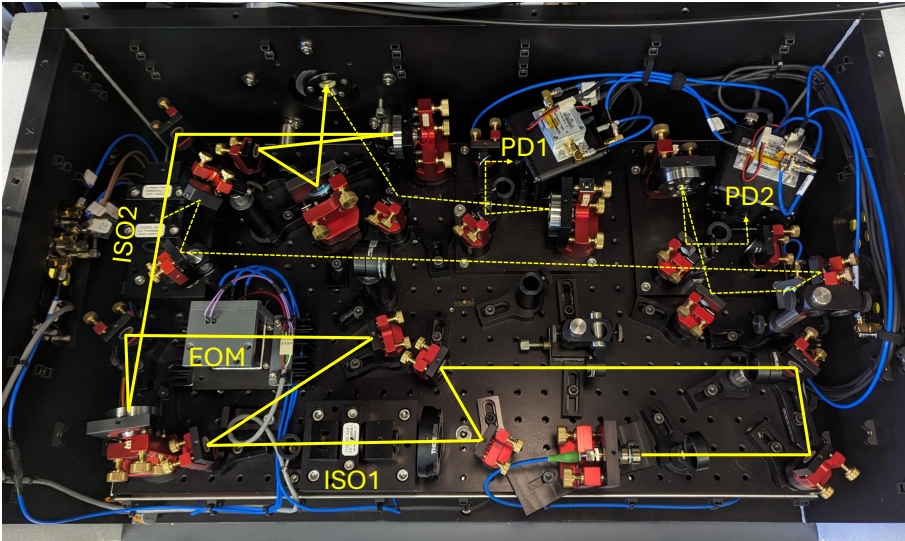


Figure 2.4: Top view of the first box at the incident side of the cavity. All relevant RF electronics for post-processing (filtering and downconversion) are situated underneath the breadboard. The yellow line follows the optical beam path starting from the fiber collimator (bottom right) and ending at the entrance window to the cavity (top left). Highlighted are the two optical isolators (ISO1 and ISO2), the EOM, and two photodiodes (PD1 and PD2).

we solely consider thermal expansion as the origin, then $\Delta x = L_{\text{EL}}\alpha\Delta T$, where L_{EL} is the etalon length, α the thermal expansion coefficient, and ΔT the maximum temperature variation. From this, we can directly see that the impact of thermal drift increases proportionally with the etalon length. This also holds for residual effects of etalons at the etalon immune distance, where the etalon length is multiple cavity lengths. For our experiment we use an aluminum breadboard ($\alpha = 23 \times 10^{-6} \text{ K}^{-1}$), and an anticipated lower wavelength of around 1200 nm for the H_2 experiment. This translates to a $26 \text{ mK} \cdot \text{m}$ upper limit, where the effect of a residual etalon at a single etalon immune distance will be stabilized at half its respective FSR, thus from whereon the baseline signal variation will decrease. For the purpose of avoiding temperature-dependent etaloning leading to RAM all the optics at the input side before the cavity were built inside a temperature-stabilized box that was also flushed with dry nitrogen (see Fig. 2.4).

Another approach to reduce the effect of etalons is by modulating its path length, which results in scrambling their disturbance. This has al-

2. FREQUENCY COMB REFERENCED NICE-OHMS FOR SATURATION SPECTROSCOPY OF EXTREMELY WEAK ROVIBRATIONAL TRANSITIONS

ready been studied by using Brewster-plate spoilers [87] and later found application within a NICE-OHMS experiment [66]. Here, Brewster-angled glass plates were mounted on galvos and provided a continuous modulation of the path length. While this method was effective in removing the etalon modulation for wider frequency scans as in our study, it must be noted that scrambling at a random length through a sinusoidal modulation will not fully remove baseline drifts. To effectively remove the baseline drift, the etalon effect must be completely averaged out, independently of the absolute frequency location of the etalon fringe and thus independent of drifts. This is achieved with a linear pathlength modulation at an integer value of the FSR of the etalon in question, with a modulation frequency higher than the averaging time of the experiment. Thus modulation with a triangular or sawtooth pattern at an integer value of the operating wavelength is required. In principle, this can be achieved through accurate modulation of the Brewster-spoiler plates, or piezo-activated mirrors under a small angle of incidence. However, in both examples, careful calibration must be performed to modulate exactly at the correct amplitude and with sufficient linearity, as otherwise its effect might be limited. Furthermore, such active elements might disturb the pointing stability of the laser beam and cause a power modulation of the cavity round-trip power. We have included several piezo-activated mirrors within the optical beam path to dither remaining etalons, but those were not used as the other RAM suppression methods worked sufficiently.

Besides the etalons, the presence of molecular transitions in the atmospheric composition within the optical beam path is also a potential source of wavelength-dependent absorption and dispersion. Water is the most dominant molecule within standard atmospheric air as it exhibits a rich structure of transitions in the IR range, especially near the expected transitions for the HD overtone study in Chapters 4, 5, and 6. Therefore, flushing the entire beam path with an inert gas such as dry nitrogen gas is a necessity at some wavelength regions to flush out all water vapor to insignificant levels. Ultimately, some level of pressure control of the atmospheric optical beam path could be realized to further stabilize the effective path length of the remaining etalons.

2.3.5 Independent RAM measurement

The direct measurement of RAM is another approach that can help understand or reduce the effect. This can be implemented by adding a third photodiode that samples the frequency triplet just before it enters the cavity, which allows determining the level of RAM acquired until that point. This RAM sampling photodiode has been implemented successfully [83], where it provides feedback to the temperature or DC bias field of the EOM. Also sometimes the photodiode in reflection can contain useful information, which can be used for post-processing of the signal [88]. In our setup, we use the third photodiode only passively to monitor the RAM of the sidebands and minimize their amplitude by tuning the EOM temperature.

The effect of RAM can also be partially removed during post-processing of the signal. As long as the variation of RAM is slow, it typically enters the first-derivative signal as either a constant baseline or a very shallow slope. Removal of a slope from the scan window is typically warranted if the scan range is sufficiently large to allow accurate determination of the present slope and baseline. An example of the effect of baseline drift removal is shown in Fig. 2.7.

Ultimately, some level of RAM on one of the 9 frequency components (8 sidebands and carrier) is unavoidable as simultaneous etalon immune distances for all sidebands are impossible to achieve (Fig. 2.3). However, the consequence of RAM on each sideband pair will be different. In this section, we mostly discussed the consequence of RAM on the NICE-OHMS sidebands at ν_{mod} and its effect on the signal, but RAM on the PDH and dVB sidebands can also lead to indirect signal distortions as it causes lock points to drift. The effect of the PDH setpoint drift will be discussed in Chapter 2.6.

2.4 Laser source and optical beampath

The laser sources used in this experiment are all diode lasers from Topica. The two lasers used for the HD and HT experiment are DL Pro systems, and for the H₂ experiment we make use of a TA (tapered amplifier) Pro system, delivering much higher output powers. While diode lasers are broadband in their nature, they allow extremely fast feedback on their current making locking and stabilizing to high finesse cavities possible. For the feedback and locking we make use of a fast

2. FREQUENCY COMB REFERENCED NICE-OHMS FOR SATURATION SPECTROSCOPY OF EXTREMELY WEAK ROVIBRATIONAL TRANSITIONS

PID controller (Toptica FALC110) and a modified PDH module (Toptica PD110), which involves an external referenced oscillator with digital phase control.

All lasers are outfitted with a double-stage optical isolator, providing around 60 dB of isolation. The lasers are fiber coupled into a polarization maintaining (PM) fiber, which provides mechanical decoupling of the laser with the setup and spatial mode cleaning of the diode laser beam. A small portion of the light is split off in the fiber, which is used for frequency calibration with a wavemeter (coarse) and frequency comb laser (for high accuracy). The main fiber runs inside a hermetically sealed box, where the fiber is terminated at a collimator.

The remainder of the optical beam path (for its layout see Fig. 2.5) is free-space and is housed in two hermetically shielded thick-walled aluminum boxes, one at the incident side of the vacuum chamber housing the cavity, and one at the transmission side. These boxes are temperature stabilized through a temperature controller (SRS PTC10) at an elevated temperature of 26 °C through resistive heating and additionally insulated with styrofoam to further dampen the influence of the varying lab temperature. This provides a constant temperature environment and atmosphere within the box (see Fig. 2.4). Hermetic sealing is acquired by having all electronic connections terminated at the box panel with sealed connectors and the removable box panels are outlined with a groove for sealing with a rubber cord. This allows efficient removal of all water vapor through a small dry nitrogen purge. In theory, even active pressure stabilization of the boxes should be possible but was not implemented in this study.

Within each box, an elevated breadboard for the optical components is mounted. This breadboard is thermally decoupled from the box walls, while having strong mechanical coupling and reference to its environment. A second stage of temperature stabilization is implemented on this breadboard by resistive heating at a slightly elevated temperature with respect to the box at 27 °C through a heating film over the entire bottom surface of the breadboard. The in-loop Pt100 temperature sensor on the breadboard shows a remarkable stability of below 1 mK. When combining this with the thermal expansion coefficient of aluminum, we see that the expected peak-to-peak modulation of one etalon immune distance (37 cm) is around 1%, effectively freezing any formed etalon in place. Another advantage of these modular boxes is that maintenance or modification to the cavity is vastly simplified by removing the entire box

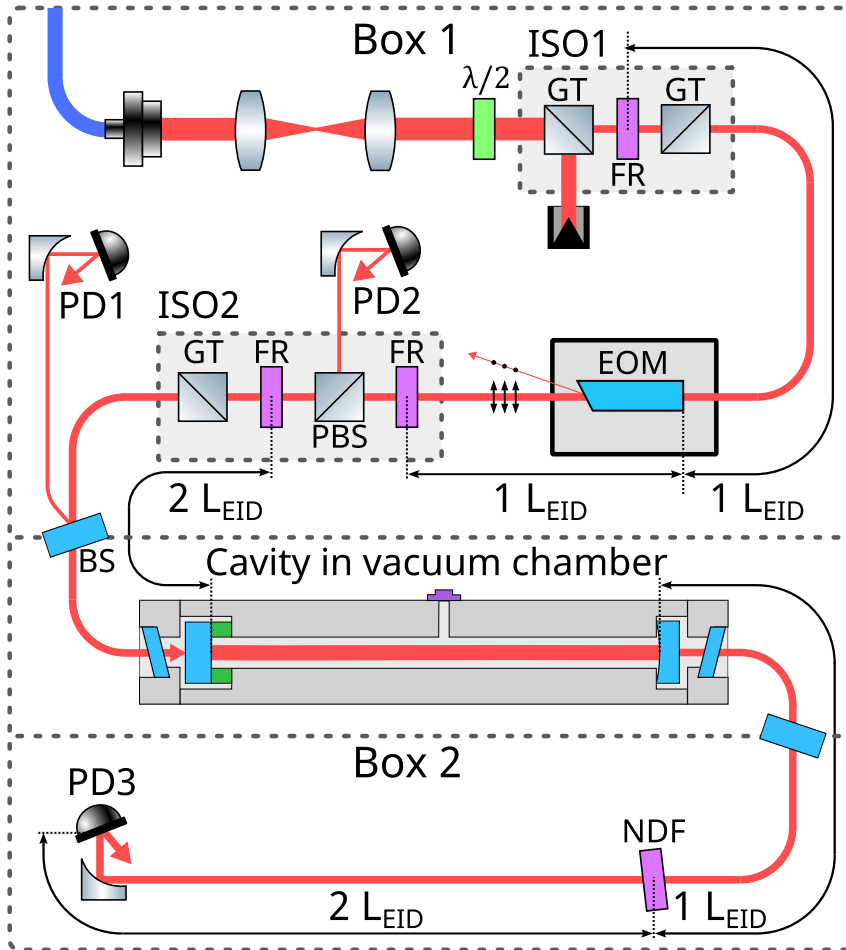


Figure 2.5: Schematic representation of the optical beamline with all relevant optical components. Beam steering mirrors are absent in this overview. ISO is optical isolator, GT is Glan-Taylor prism, FR is Faraday rotator, PBS is polarizing beam splitter cube, NDF is neutral density filter, BS is beam sampler, PD is photodiode and L_{EID} is etalon immune distance. The tilted windows on the box/vacuum chamber interface are the vacuum chamber windows. All windows are wedged and all surfaces have AR coatings, except for the frontside of the beamsampler window.

2. FREQUENCY COMB REFERENCED NICE-OHMS FOR SATURATION SPECTROSCOPY OF EXTREMELY WEAK ROVIBRATIONAL TRANSITIONS

from the experiment. This avoids removing optical elements to acquire access to the cavity and thereby only requires minimal realignment after repositioning the box by positional reference points.

After the fiber is terminated in the fiber coupler on the breadboard the beamline first passes through the mode-matching stage, which can be conveniently positioned before the free-space EOM to avoid unnecessary etalon effects. Mode matching is performed by using a pair of spherical lenses to focus the beam to the waist size in the cavity for optimum incoupling efficiency. After the mode matching the beam passes through a tunable half-waveplate and the first home-built optical isolator, where the half-waveplate is used for laser power adjustment. The optical isolator consists of two Glan-Taylor polarizers (Thorlabs GT5-A) and an interchangeable Faraday rotator (Thorlabs IxxxxR5 series) depending on the used wavelength. All components of the optical isolator are positioned under a small angle to avoid the formation of etalons. The second Glan-Taylor polarizer is aligned at perfect horizontal polarization to match the required polarization input state of the EOM, which directly comes after this optical isolator. The free-space EOM is mounted on a Peltier element with a thermally decoupled heatsink from the breadboard to allow fine control of the EOM temperature without disturbing the thermal stability of the breadboard. After the EOM a second home-built optical isolator is placed. This isolator is responsible for breaking the otherwise unavoidable etalon between the EOM and cavity mirror and deflecting the reflection from the cavity for detection on a photodiode (PD2) for the necessary PDH and deVoe-Brewer locking.

This homebuilt 'double-stage isolator' consists of a Faraday rotator, polarizing beam splitter cube, a second Faraday rotator and a Glan-Taylor polarizer. Here, the first isolation stage is formed by the EOM crystal, the Faraday rotator and polarizing beam splitter cube. Since the EOM crystal is birefringent and has an angled output surface, it will deflect the orthogonal (vertical) polarization component and effectively act as a polarizer. The normal incidence surface of the EOM is positioned at one etalon immune distance with the Faraday rotator, further reducing the effect of any possible etalons. The second stage of the isolator is formed by the PBS, second Faraday rotator and Glan-Taylor polarizer. The PBS at a fixed 45° angle is used to deflect the reflection from the cavity sideways from the optical isolator. All components are under a small angle with respect to the beamline to avoid the formation of etalons.

After the second isolator, the laser beam enters the main vacuum chamber through an angled vacuum window, which is a wedged beam sampler. This is to create a sampling beam for a photodiode (PD1) to measure the power level incident on the cavity and any RAM present on the sidebands before entering the cavity. The main portion of the beam that entered the vacuum chamber first passes through the angled and wedged vacuum window of the cavity before hitting the cavity mirror.

Light in transmission of the cavity exits in a similar fashion by first passing the cavity window and then the vacuum chamber window before entering the second box at the other side of the experiment. This box only houses an optical attenuator to adjust the power to not exceed the damage threshold of the photodiode and the detection photodiode stage (PD3).

The three photodetectors in this experiment (New Focus 1611FS-AC) are modified by removal of the ball cap lens in front of the photodiode chip, as the photodiode and lens can be a significant source of an etalon [86]. The laser beam is focused using an off-axis parabolic mirror onto the photodiode under an angle of 22.5° to avoid any back reflection and potential formation of etalons. The focus of the beam is designed to be significantly smaller than the photodiode diameter of 0.1 mm to properly sample the entire cross-section of the beam. Accurate tuning of the generated focus from the off-axis parabolic mirror with respect to the photodiode chip is achieved by having the photodetector on a translation stage to position the photodiode exactly at the focus. The photodetector has two separate amplification stages; a DC output (DC - 20 kHz), for separate power monitoring and observations of slow modulations, and an AC output (30 kHz - 1 GHz), for the high-frequency signals.

Unfortunately, not all optical elements requiring transmission can be positioned at an etalon immune distance with respect to each-other. However, only the EOM input surface and cavity mirror are at an unavoidable normal incidence angle, while all other components accept some level of angular tilt. Within the optical isolators, the Faraday rotator is the key component where an etalon is broken due to the rotation in polarization. As the Faraday rotator also has the smallest acceptance angle compared to the other components used in the isolators, it is also put at an etalon immune distance with respect to the other normal incidence surfaces. This means the formation of three possible etalons at the etalon immune distance (see Fig. 2.5). The first etalon of one cavity

length distance is formed between the Faraday rotator of the first optical isolator and the front surface of the EOM crystal. The second etalon of one cavity length distance is formed between the front surface of the EOM crystal and the first Faraday rotator of the second isolator. The third etalon of two times the cavity length is formed between the second Faraday rotator of the second optical isolator and the cavity mirror surface.

2.5 Parallel demodulation through a high-speed digital lock-in amplifier

In most realizations of NICE-OHMS for saturation spectroscopy, a second layer of modulation is applied through dithering of the cavity length as this is a very effective method of significantly reducing the effects of RAM, as explained in the previous subchapters. However, these two layers of modulation also require two demodulation steps to recover the desired signal. This is typically approached by two-step demodulation in series (so-called tandem demodulation), by first analog demodulation of the high-frequency component and subsequently demodulation of the low-frequency dither in a lock-in amplifier. The complexity of this approach is that one needs to optimize two phases independently to acquire the desired signal. In the first demodulation step, one needs to select the correct phase for either demodulating at the absorption or dispersion phase. This process can be a burden if not all signal channels are available simultaneously. Secondly, the first high-frequency demodulation step typically occurs in an analog mixer, which have known imperfections. To obtain both the absorption and dispersion phase simultaneously, one could use a so-called I-Q (in-phase and quadrature) mixer, which exhibits a 90° phase relationship in the two output channels. However, this orthogonality is not perfect and some leakage of both channels will occur.

In our experiment, we make use of a high-speed digital lock-in amplifier (Zurich Instruments HF2LI, 50 MHz bandwidth). As the 50 MHz bandwidth is insufficient to directly provide modulation and demodulation at the required $\nu_{\text{mod}} = \nu_{\text{FSR}} \approx 404$ MHz frequency, we use an additional up and down conversion step within RF mixers with a local oscillator (Siglent SSG3021X) at frequency $\nu_{\text{LO}} = 374$ MHz. Thus the modulation starts at the lock-in amplifier at frequency $\nu_{\Delta} = 30$ MHz, which is

2.5. Parallel demodulation through a high-speed digital lock-in amplifier

first upconverted in a mixer by the local oscillator resulting in sum and difference frequencies $\nu_{\text{LO}} \pm \nu_{\Delta}$. Here, the sum of 404 MHz is selected using bandpass filtering and used to drive the EOM. The obtained signals in the photodiodes are first downconverted in a similar fashion by mixing the signal components with the local oscillator. This results in frequencies $\nu_{\text{mod}} \pm \nu_{\text{LO}}$, where ν_{Δ} results from the difference frequency and can be straightforwardly selected and filtered. As the same local oscillator is used for both up and downconversion, the phase relationship of this oscillator drops out and both the absorption and dispersion phase of measurement are maintained on the remaining signal without requiring a more complex I-Q mixer. The necessary feedback to the ν_{mod} frequency to match the FSR of the cavity can be conveniently applied to the local oscillator frequency, which maintains a constant frequency ν_{Δ} within the digital lock-in amplifier.

Both NICE-OHMS signal modulations are available within the lock-in amplifier at frequencies ν_{Δ} and f_{wm} . The HF2LI-MOD option within the lock-in amplifier provides direct demodulation of a 'sideband' (the dither in this experiment) next to an original 'carrier' (the direct NICE-OHMS signal present at ν_{Δ}), thus demodulation of both frequencies in a single step. The benefit is that this only requires a single phase to optimize, and the perfect 90° balanced digital mixer provides direct signal outputs of both the absorption and dispersion phase of measurement. Due to the multiple channels available within the HF2LI-MOD module, it allows simultaneous observation and recording of the direct NICE-OHMS signal and two different harmonics of the derivative detection, for example the first and second.

The other novelty implemented concerns the retrieval of the dVB error signal in a slightly alternative scheme. Traditionally, this signal is acquired by phase-sensitive demodulation at either frequency $\nu_{\text{mod}} \pm \nu_{\text{PDH}}$ which requires first the generation of said frequency using a mixer and narrow bandpass filter to select a single frequency component. This 'traditional' scheme was also implemented in our original NICE-OHMS realization in Chapter 4. In our updated scheme using the digital lock-in, we can obtain both dVB frequency components within the bandwidth range of the lock-in as the relevant dVB signal components are at frequencies $\nu_{\text{mod}} \pm \nu_{\text{PDH}} - \nu_{\text{LO}} = \nu_{\Delta} \pm \nu_{\text{PDH}}$ after the downconversion. For the typical ν_{PDH} frequency of 20 MHz, this results in dVB signal components at either 10 or 50 MHz within the lock-in amplifier environment. However, as the original PDH driving frequency is not originating

2. FREQUENCY COMB REFERENCED NICE-OHMS FOR SATURATION SPECTROSCOPY OF EXTREMELY WEAK ROVIBRATIONAL TRANSITIONS

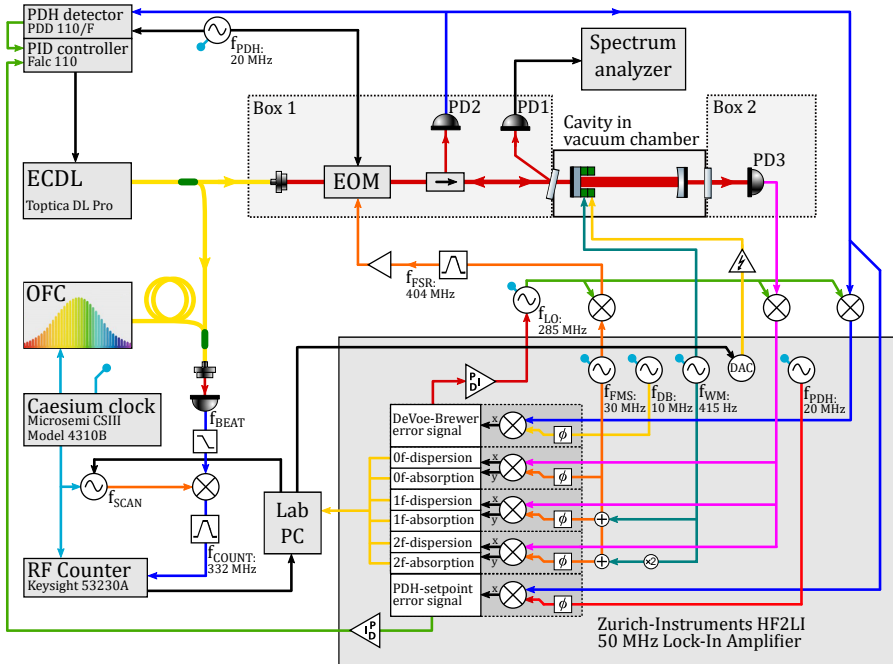


Figure 2.6: Schematic representation of the complete NICE-OHMS setup including all relevant electronic components, such as the double resonant EOM and enhancement cavity. Clearly outlined is the implementation of the digital lock-in amplifier, which forms the center of the NICE-OHMS experiment as it controls multiple PID loops, drives the piezo stages, and handles nearly all phase-sensitive demodulations necessary within the experiment. Outlined at the left bottom part is the frequency locking and calibration stage, consisting of a stabilized frequency comb with our in-house cesium frequency standard.

from the lock-in, both the lock-in amplifier and PDH frequency generator should be phase locked to the same 10 MHz reference to ensure a constant phase relationship. If this is ensured, the dVB error signal can be retrieved at either demodulation at 10 or 50 MHz within the lock-in amplifier. The internal PID controller within the HF2LI can be conveniently used to apply feedback to the local oscillator frequency ν_{LO} to lock the sidebands to their respective modes.

The last implemented method is to simultaneously observe the PDH error signal used for locking the laser in parallel within the lock-in amplifier. As this frequency is already within the bandwidth of the lock-in amplifier, it is added again into the signal input after the down-conversion

stage. Thus in total 4 RF signals of interest can be retrieved from PD2: The direct NICE-OHMS signal in reflection, the two dVB error signals, and the PDH error signal. This signal is used to monitor whether a PDH setpoint offset occurs within the laser PID controller, which can lead to additional signal distortion and increased noise levels. This subject will be discussed in the next subchapter.

The entire logical measurement layout including all modulation and demodulation equipment, locking electronics, optical components, lasers and frequency referencing, and lock-in detector are displayed in Fig. 2.6.

2.6 Active PDH setpoint stabilization

The laser, or carrier wave, is locked to the cavity through PDH stabilization. The obtained PDH error signal often exhibits some level of offset, which if uncorrected will result in an offset of the carrier with the respective cavity mode it is locked onto. A small offset of the lock-point with respect to the peak of the cavity mode has little influence for most applications, as long as this offset remains constant. In the case of NICE-OHMS, all three present fields (the carrier and both modulated sidebands) are simultaneously shifted with respect to their respective cavity mode if a PDH offset is present. This results in an asymmetric situation, where each individual field will experience both amplitude and phase shift from the cavity, which can have significant consequences on both noise and lineshape asymmetry leading to a potential frequency shift due to fitting errors [89].

While at first glance a PDH offset induces only a common mode shift on both the carrier and sidebands, it does bring additional sensitivity to intensity and frequency noise from both the laser and cavity which is not present when the triplet is locked to the center of the cavity modes. In addition, a secondary offset present in the deVoe-Brewer stabilization will only further increase the asymmetry of the triplet balance thereby increasing potential sensitivity to external noise sources. The effect is that the noise floor in NICE-OHMS is significantly degraded when the PDH offset is not optimized to the center of the fringe, which is demonstrated in our noise and stability measurements (Fig. 2.7). This shows that while NICE-OHMS is immune to technical noise in the first order, there can be a secondary effect where this noise can couple into the observations. Already in the first studies of NICE-OHMS it was ob-

2. FREQUENCY COMB REFERENCED NICE-OHMS FOR SATURATION SPECTROSCOPY OF EXTREMELY WEAK ROVIBRATIONAL TRANSITIONS

served that a bad laser lock degraded the signal to noise of the acquired signals [43].

The unavoidable anomalous dispersion when scanning a molecular transition again further complicates the problem, as this will result in an effective change of the FSR locally. Its resulting effect on the NICE-OHMS signal and lineshape has been theoretically investigated in the situation of no present PDH offset by Schmidt *et al.* [90] for the Doppler broadened situation, but can be readily extended to the sub-Doppler condition. This shows that the obtained lineshape is symmetric in case a PDH offset is absent. While no generalization was performed for the situation with PDH offset, its effect can be readily observed as this directly influences the symmetry of the sidebands which then become wavelength-dependent due to the anomalous dispersion. The effect of a PDH offset on the symmetry of an obtained sub-Doppler lineshape has been observed by Hua *et al.* [89], where different settings of the PDH offset resulted in asymmetric lineshapes resulting in significant deviations of the fitted transition frequency.

Manual optimization of the PDH offset is possible by the traditional methods of symmetrization of the PDH error signal, or otherwise through maximizing the power transmission of the laser through the cavity. Calibration to a known symmetric transition is also a possibility for further fine adjustment. The most convenient method is minimizing the residual noise band of the NICE-OHMS signal, which corresponds with the most symmetric locking situation. However, it was found that the PDH offset drifts both in laser frequency when scanning a transition and time. This is partially due to the fundamental nature of NICE-OHMS, as it exhibits a total of 8 sidebands and thereby has 3 competing heterodyne signals at the PDH frequency; one pair of sidebands from the first-order modulation surrounding the carrier for the PDH stabilization, and two pairs of sidebands from the second-order modulation surrounding the spectroscopy sidebands (see Fig. 2.2). This makes it more prone to disturbances such as RAM caused by etalons, as each individual pair of sidebands has influence on the PDH error signal. The effect of scanning the cavity and laser will in turn change the cavity FSR, which in turn changes the DeVoe-Brewer lock, which affects the balance of the second-order sidebands, potentially causing a PDH offset. This all shows that the noise-immunity of NICE-OHMS is significantly degraded when the delicate balance of the sidebands with their respective cavity modes is disturbed.

However, the most notable cause of a drifting PDH offset was the internal competition within the laser PID controller between the unlimited integrator acting on the piezo of the laser and the high-bandwidth loop acting on the current of the laser. This was observed through a drift of the PDH signal within the lock-in amplifier when scanning the experiment in frequency. For this purpose, we implemented an additional feedback loop by adjusting the PDH setpoint value to maintain a constant PDH error signal offset. This was implemented within the lock-in amplifier by first manually optimizing the PDH setpoint and subsequently locking to its respective PDH offset point through the internal PID controller, acting on the 2nd input of the FALC110 PID controller of the laser. This ensures a more stable configuration, where locking drifts over time are canceled. Unfortunately, slowly drifting etalons will still cause RAM on the PDH signal resulting in slow drifts over time, requiring manual optimization from time to time.

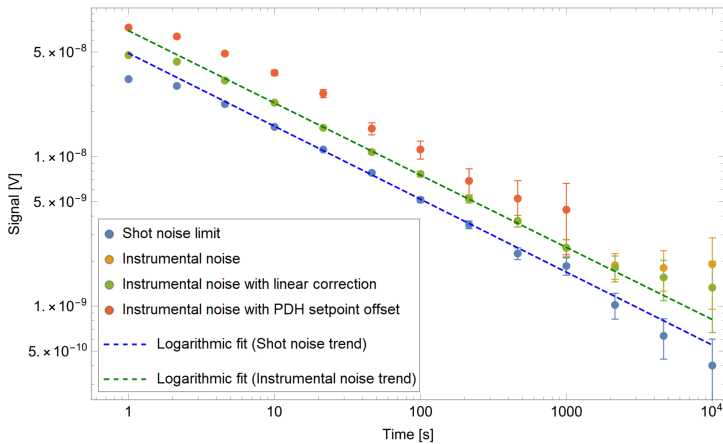


Figure 2.7: Allan deviation of the $1f$ signal component with an empty cavity for both optimum configured PDH offset conditions (yellow and green) and an induced PDH setpoint offset (red). The pure recorded shot-noise of the system is shown in blue. A logarithmic trend is added for clarity. The initial deviation before 10 seconds below the logarithmic trend is an artifact of the low-pass filtering present in the lock-in amplifier. These results show that the noise of the running experiment under optimum conditions is only 40% above the shot-noise limitation. After roughly an hour of averaging drift takes over and degrades the sensitivity for longer averaging times. The effect of removal of a linear background slope is shown in green, which is valid as a method of post-processing of the signal data. It is also clear that an offset in the PDH setpoint degrades the noise floor of the experiment.

2. FREQUENCY COMB REFERENCED NICE-OHMS FOR SATURATION SPECTROSCOPY OF EXTREMELY WEAK ROVIBRATIONAL TRANSITIONS

The performance of the NICE-OHMS spectrometer was assessed by recording the $1f$ signal of an empty cavity over an extended period of time in optimized PDH setpoint condition. As a comparison, also the pure photon-shotnoise was recorded. This was obtained by switching off the sidebands and demodulating the signal at a small offset of 10 kHz with respect to the actual FSR to avoid recording a heterodyne signal of residual photons in the neighboring cavity modes next to the carrier. As an additional comparison a $1f$ signal recording with an induced PDH setpoint offset was also recorded. From these signals, an Allan deviation plot could be generated to assess the noise stability over time (Fig. 2.7). From this result we can observe that the performance is only 40% above the directly measured photon shot-noise floor for extended periods of time, proving its extreme sensitivity. After around an hour of averaging, the background drift of the signal due to RAM starts to dominate, degrading its sensitivity. As the drift is mostly linear and slow, the $1f$ signal can be post-processed by removal of a linear slope, which effectively removes all effects of the present RAM.

2.7 Frequency comb referencing

Our approach is to benefit from the good short-term stability of the enhancement-cavity, which is specifically designed to have low frequency drift and narrow linewidth. This allows the laser to be stabilized onto the enhancement cavity and only slow longterm drift needs to be cancelled, omitting more complicated high-bandwidth loops with external stable references. Effects of instantaneous broadening from fiber noise are also mitigated in this scheme due to the low bandwidth and long averaging. We opted for a frequency lock by stabilizing the beatnote frequency with the frequency comb instead of a more common phase lock. This is due to the fact that the applied dither of the cavity length at 395 Hz has a peak-to-peak amplitude of up to several 100 kHz, which complicates a phase lock due to the need for a large phase capture range for the necessary phase unwrapping. A counter lock can mitigate this problem due to the nature of having a discrete gate timing. By adjusting the gate time to an integer period of the applied dither period, the influence of the dither drops out.

The used frequency comb laser (Menlo Systems FC1500-250-WG) is referenced to our in-house cesium clock (Microsemi CSIII), which is in turn

long-term monitored through GPS. This sequence can provide absolute frequency calibration down to 10^{-13} in the optical domain after sufficient averaging. The beatnote is acquired by first transporting the comb light to the NICE-OHMS setup through a 80m fiber, where a beatnote is generated by the overlap of the spectroscopy laser and the frequency comb light and measured using a photodiode. The beatnote is first upconverted to 332 MHz by a local oscillator (ν_{scan}), where a narrow band-pass filter is applied. This trick significantly increases the usable bandwidth of the frequency comb, where a stable lock can be formed for beatnotes between 5 to 110 MHz and thereby using up to 85% of the usable comb space without needing to alter frequency comb parameters. This allows continuous tuning within the locking range by adjusting the ν_{scan} frequency.

A digital feedback loop is implemented on the lab computer which runs a PID algorithm to provide feedback on the piezo of the cavity. Currently the main limitation is the short term stability of the used frequency comb, which is around 5 to 10 kHz in the optical domain. In principle a modern low-noise frequency comb, which is phase locked to an ultra-stable Hz laser, will provide a direct comparison of the NICE-OHMS cavity with such a stable optical reference. In potential this will allow stabilization to the Hz level, bringing a further advanced stage of ultra-high resolution and precision spectroscopy in reach.

Vibration insensitive cryogenic cavity design for cavity-enhanced saturation spectroscopy

3.1 Introduction

Linear optical resonant enhancement cavities have revolutionized the field of molecular spectroscopy by enabling high-precision and high-resolution spectroscopy of weak rovibrational transitions. This can be primarily attributed to the direct enhancement of the effective optical path length within these cavities, leading to a substantial increase in interaction length and thus sensitivity. In addition, the enhancement leads to power amplification of the counterpropagating beams, which can facilitate saturation spectroscopy and thereby the generation of Doppler-free Lamb dips. As a result, the generation of Doppler-free Lamb dips becomes possible, even for very weak nearly forbidden transitions, thus providing a valuable tool for achieving high precision and resolution in spectroscopy.

Enhancement cavities directly benefited from the ongoing advancement in materials science on better quality mirrors, currently allowing en-

3. VIBRATION INSENSITIVE CRYOGENIC CAVITY DESIGN FOR CAVITY-ENHANCED SATURATION SPECTROSCOPY

hancement ratios of over five orders of magnitude. Although better mirrors will provide a continuing path of improvement in the future, other advances have primarily focused on reducing detection noise levels by employing specific measurement techniques within these enhancement cavities.

Besides these technical advancements focusing on lowering the level of the noise-equivalent absorption, the search for even more accurate and sensitive experiments have also led to cryo-cooled enhancement cavities. Cryo-cooling does not directly alter the experimental sensitivity itself, but it mainly works by manipulating the molecular species of interest. The main effect is reducing the mean velocity of the molecules thereby reducing the Doppler width and enhancing the population of orthogonal flying molecules, which directly benefits saturation spectroscopy. The reduced speed also increases the transit time through the cavity laser mode, potentially providing narrower linewidths, while it also increases the level of saturation of extremely weak resonances. Cooling also reduces the pressure for a fixed density and thus collisional broadening. Moreover, rotational state redistribution at low temperature gives an increase of the lower rotational state population and effectively increases the density of these states. This multitude of advantages led multiple groups during the last decade to develop cryogenic systems despite the challenging engineering of building a cavity which is compatible with cryogenic temperatures and combining a stable cavity with the inherent vibrations of a cryocooler [28, 91, 92].

Cavities can essentially be characterized into two classes: ultra-stable, fixed-length (non-tunable) cavities, primarily used within the field of ultra-stable lasers and optical clocks, and length-tunable cavities, which operate and enhance at a specific operating frequency. The ability to scan a resonance of interest in spectroscopy necessitates tuning of the absolute frequency, hence the need for tunable cavities. Typically, these tunable cavities are actively length-stabilized through a feedback loop by referencing to an external frequency standard. This reference to an absolute frequency standard allows scannable measurements of molecular transitions. The feedback loop also allows for less stringent requirements on both the short and long-term length stability of the design, as it can cancel out these drifts. However, when the linewidths of the resonances of interest approach the short-term stability of the cavity, the lineshape can be artificially broadened due to the limited short-term stability of either the cavity itself or the reference. This issue can be ad-

dressed by employing more advanced feedback involving high bandwidth phase-locked loops and fiber link stabilization to reduce instantaneous broadening, but it can be challenging to construct and adds complexity to the whole system. An alternative approach is by designing a cavity with superior short-term stability, which drastically reduces the need of fast complex stabilization schemes as only the long term drift needs to be controlled with a low bandwidth loop. While the design of a tunable highly-stable cryo-cooled cavity introduces a certain level of complexity in itself, many design aspects have already been successfully developed in the ultra-stable cavity community and can be readily implemented [93–98].

In the following sections of this chapter, we delve into the intricate process of designing a highly-stable, cryogenically-cooled cavity for the saturation of extremely weak transitions. We begin by exploring various cavity geometries and configurations, examining the impact of parameters such as cavity length and mirror radius on potential higher-order mode interferences, giving rise to signal disturbances, and outlining strategies for their avoidance. A crucial component when approaching the photon shot noise limit of detection.

Next, we turn our attention to the construction of the stable cavity resonator itself, with a particular focus on its cryogenic compatibility. This involves a detailed discussion on material selection and the challenges encountered at low temperatures, including piezo operation and glueless mirror mounting. We also address the necessity of high laser power compatibility, a critical requirement for saturation spectroscopy of extremely weak transitions.

Subsequently, we dive into the design of a vibrationally insensitive cavity by carefully choosing and optimizing the mounting points of the resonator. This topic naturally leads us to the dampening of the vibrational perturbations imposed by the cryocooler. This section also encompasses the temperature stability of the entire system and cavity resonator, a key factor in minimizing length variations.

Finally, we present the performance characteristics of the cavity, assessing its linewidth, frequency stability, and other pertinent aspects. This comprehensive exploration underscores the intricate interplay of various factors in the design of a highly-stable, cryogenically-cooled cavity for saturation spectroscopy at the quantum noise limit.

3.2 Cavity geometry

3.2.1 General description

Fabry-Pérot resonators occur in various geometries, distinguished by their mirror curvature(s) and length. The primary requirement for these designs is to meet the stability criterion, ensuring that the light beam remains confined within the cavity across infinite reflections. This stability criterion is defined as [99, 100]:

$$0 \leq \left(1 - \frac{L}{R_1}\right) \left(1 - \frac{L}{R_2}\right) \leq 1. \quad (3.1)$$

Here, L represents the cavity resonator length and R_1 , R_2 are the mirror radius of curvatures (ROC) of the first and second mirrors, respectively. This criterion can be simplified by defining the stability parameter g_i as

$$g_i = 1 - \frac{L}{R_i}, \quad (3.2)$$

leading to a more concise stability criterion:

$$0 \leq g_1 g_2 \leq 1. \quad (3.3)$$

Among the variety of geometries that yield stable configurations, the equal-radius concave-concave (abbreviated c.c.) and the plano-concave, also known as hemispherical (abbreviated p.c.), geometries are most commonly employed in cavity-enhanced (saturation) spectroscopy. For these two geometries, the stability criterion simplifies to $0 \leq g^2 \leq 1$ and $0 \leq g \leq 1$, respectively. From these criteria, it can be readily solved that a stable cavity can be obtained when $R \geq L/2$ for the c.c. geometry and for $R \geq L$ for the p.c. geometry. Typically, the radius of curvature of the mirrors in both designs is chosen to be significantly larger than the cavity length as this minimizes beam size variation along the cavity length. A homogeneous beam size is especially important with saturation spectroscopy, as it ensures constant intensity and time-of-flight interaction over the whole interaction zone. While both configurations provide stable cavity configurations, there are some key features to each geometry that are important to consider.

In order to make a meaningful comparison between both geometries it is important to normalize the significant properties and parameters. Obviously, the cavity length must be set equal, as this determines the

equivalent path length of interaction, defines important parameters such as the free spectral range (FSR) and also dictates several of the cavity's mechanical properties. However, the ROC of the mirrors can be set as a free parameter. This allows for normalization of the average beam waist of both designs. This is crucial, as the mode volume determines both the possible interaction volume of molecules and the average intensity of the light within the cavity, both important properties of saturation spectroscopy. In order to find for which ROC the mode volume is equal for both geometries, we must first define the beam propagation within both designs.

The Gaussian TEM₀₀ mode within the cavity evolves as

$$w = w_0 \sqrt{1 + \frac{z^2}{z_0^2}}, \quad (3.4)$$

where w_0 is the minimum waist size at the focus and z_0 the Rayleigh range, which is in turn given by

$$z_0 = \frac{\pi w_0^2}{\lambda}. \quad (3.5)$$

This in turn also gives an expression for the minimum waist size, which can be expressed through

$$w_0 = \sqrt{\frac{z_0 \lambda}{\pi}} \quad (3.6)$$

and allows substitution of w_0 in Eq. (3.4), which in turn becomes

$$w = \sqrt{\frac{z_0 \lambda}{\pi}} \sqrt{1 + \frac{z^2}{z_0^2}}. \quad (3.7)$$

In order to solve both Eq. (3.6) and Eq. (3.7), we first must define the boundary conditions of both the c.c. and p.c. geometries. For both geometries, the Gaussian beam wavefront curvature has to match the ROC of both mirrors at the position of the mirror surface. Secondly, the waist of the Gaussian beam is located at the center of the cavity for the c.c. design and at the position of the flat mirror for the p.c. design. To proceed we first define the wavefront curvature (R_G) of a Gaussian beam, which is given by

3. VIBRATION INSENSITIVE CRYOGENIC CAVITY DESIGN FOR CAVITY-ENHANCED SATURATION SPECTROSCOPY

$$R_G = z + \frac{z_0^2}{z}. \quad (3.8)$$

From this equation we can determine the Rayleigh range as a function of the cavity length and mirror ROC from the known boundary conditions of both geometries. For the c.c. geometry, the waist is located at the center of the cavity; thus, at distance $z = L/2$ the wavefront curvature must be equal to the mirror ROC. For the p.c. geometry the waist is located at the flat mirror; thus here the wavefront curvature must match the ROC of the concave mirror when $z = L$.

Since now the Rayleigh length is defined in terms of known parameters, we can proceed to calculate the mode volume of both geometries by performing a volume integral in cylindrical coordinates. The volume integrals are defined through

$$V_{cc} = \int_{-L/2}^{L/2} \int_0^{2\pi} \int_0^{w_{cc}(z)} r \, dr \, d\phi \, dz \quad (3.9)$$

$$V_{pc} = \int_0^L \int_0^{2\pi} \int_0^{w_{pc}(z)} r \, dr \, d\phi \, dz \quad (3.10)$$

If we now execute both integrals, substitute all variables to known parameters, set L to unity and solve $V_{cc} = V_{pc}$ for R_{cc} , we acquire a function of R_{cc} as function of R_{pc} for equal mode volume. The result is plotted in Fig. 3.1.

This shows that in the limit of large ROC, both geometries have an equal mode volume when $R_{cc} = 2R_{pc}$. For more common and practical R/L ratios (in between $2 \leq R_{pc} \leq 20$) a deviation up to 15% from $R_{cc} = 2R_{pc}$ is observed. For obvious reasons, the ROC ratio will be fixed to 2 as typically only integer value ROC mirror substrates are available commercially. The effect of fixing the ratio to $R_{cc} = 2R_{pc}$ for all values of R_{pc}/L on the mode volume ratio V_{cc}/V_{pc} is plotted in Fig. 3.1, which shows that the mode volume difference is at most 4%. This concludes that fixing the ROC ratio between the c.c. and p.c. geometries to two is a valid approximation.

Despite theoretical advantages for the c.c. geometry, other experimental and practical arguments are in favor for the p.c. design. The first practical argument is that the p.c. design only needs one mirror replaced if one desires to change the cavity beam size. By locating the concave

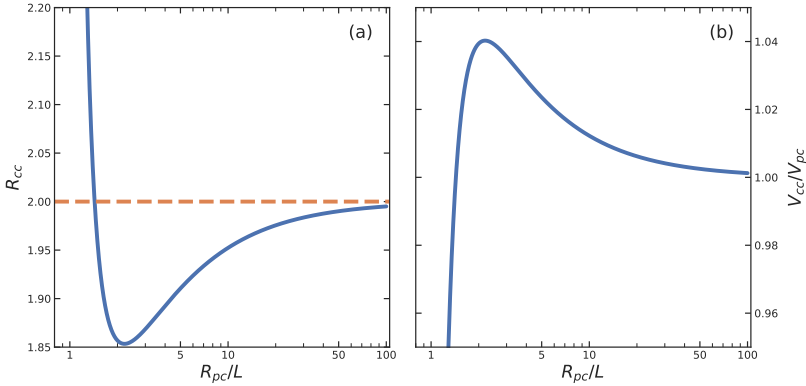


Figure 3.1: Mode volume comparison between the concave-concave and plano-concave geometries. Panel (a) shows the ROC of the c.c. design as a function of the ROC of the p.c. design for equal mode volume. Panel (b) shows the mode volume comparison for when the ROC ratio is set to $R_{cc} = 2R_{pc}$.

mirror at the transmission or exit side of the cavity, a mirror swap can be more easily performed, as the beam optics at the incident side can remain in place and aligned with the resonator mode. Another advantage is that the piezo-activated mirror preferably has a significant pre-compression force to load the piezo for better linear and hysteresis-free operation. A larger flat contact area of the plane mirror is more suited to compress against the piezo surface and avoids any unwanted stresses within the substrate or possible deformation of the mirror surface.

Another argument is that a plane mirror can be produced with better surface tolerances than a curved mirror. A curved mirror might have small variations in the ROC along the surface and possibly have a slight cylindrical deformation. Also, the focal point might be slightly off with respect to the center axis of the mirror substrate. All these possible deviations can lead to a break of the (cylindrical) symmetry of the cavity in the case of the c.c. geometry, which can result in non-degenerate higher-order transverse modes and thus a higher chance of higher-order mode collisions. The effects of this will be extensively discussed in the next subchapter.

While there are advantages and disadvantages for both geometries, the remainder of the chapter will cover both geometries where possible. Also, note that the cavity design itself is compatible with both geometries as the mirrors can be readily changed to any desired configuration.

3.2.2 Paralellism tolerance

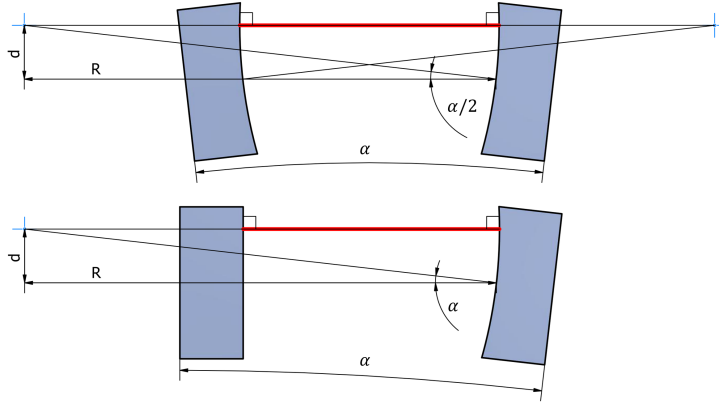


Figure 3.2: Dramatic representation of the effect of a small angle (α) between the cavity mirrors for the c.c. (top) and p.c. (bottom) geometries. The displaced laser mode (red) is projected orthogonally on both mirror surfaces. The focal point of the curved mirror(s) is indicated by the blue mark. The ROC is indicated with distance R , and the resulting lateral offset of the laser mode with the center of the cavity is indicated by distance d .

Linear (enhancement) cavities are often designed without any possibility of re-alignment of the cavity mirrors, thereby fully relying on the parallelism of the mirror-supporting surfaces. A residual angle due to tolerances in the parallelism causes a mostly lateral shift of the carrying fundamental mode within the resonator. A lateral shift from the center is tolerable as long as the beam remains sufficiently clear from any clipping elements between the cavity mirrors. From goniometric analysis, illustrated in Fig. 3.2, we can deduce that the allowable angular tolerance is given by $\alpha = 2 \arctan(d/R_{cc})$ for the c.c. geometry and $\alpha = \arctan(d/R_{pc})$ for the p.c. geometry. Here, α is the maximum, d is the allowable lateral shift inside the resonator, and R the ROC of the curved mirror(s). For the limit $R \gg d$, which holds for most practical situations, the above equations converge to $\alpha = 2d/R_{cc}$ and $\alpha = d/R_{pc}$ for the c.c. and p.c. geometries respectively. Note that for equal mode volume $R_{cc} = 2R_{pc}$, thus both geometries have an identical tolerance dependency for the limit of large ROC. The maximum allowable value for d can be determined by calculating the allowable loss of the Gaussian laser mode through an aperture (Eq. (3.16)) to not significantly decrease the finesse of the cavity, which is discussed in the following section.

3.3 Higher-order mode collisions

3.3.1 Introduction

Optical cavities can be operated at various resonant Gaussian transverse electromagnetic (TEM) modes, but are mostly driven at their fundamental TEM₀₀ Gaussian mode. The higher-order modes occur as cylindrical transverse modes (TEM_{pl}) or as rectangular transverse modes (TEM_{mn}), depending on the resonator symmetry. For most cavity configurations these transverse modes are located at different operating frequencies, which allows selection and operation on each individual transverse mode. The fundamental TEM₀₀ mode is selected by means of mode-matching of the fundamental Gaussian beam incident into the cavity, which leads to suppression of the higher-order transverse modes due to poor spatial coupling. This ordinarily results in reliable operation and locking on the TEM₀₀ mode as error signals from the higher-order modes are typically insufficient in amplitude to serve as stable locking points.

However, a degeneracy with a higher-order mode might still be present and can be caused by unwanted instabilities in both locking and signal acquisition [101]. This occurs when a higher-order mode is simultaneously resonant with the TEM₀₀ mode on which the carrier of the laser is stabilized, or if a higher-order mode is resonant with one of the two sidebands used for the Pound-Drever-Hall (PDH) stabilization. These so-called mode collisions can result in disturbances in the locking stability through either coupling power to this higher-order mode in question or through a shift of the PDH lock point due to disruption of the error signal. When using NICE-OHMS as the detection technique, these collisions can lead to an apparent dispersion and/or absorption if either the carrier or one of the NICE-OHMS heterodyne sidebands collide with a higher-order mode. This can be observed as transition-like features or 'ghost signals' and when the detection sensitivity approaches the photon-shot noise limit even the smallest disturbance to the delicate stability can lead to an unwanted increase in noise levels. It is therefore crucial to design a cavity where higher-order mode collisions are both avoided and suppressed. Both strategies will be discussed extensively in the following sections.

3.3.2 Higher-order mode avoidance

The first strategy is to reduce the number of possible higher-order mode collisions by exploiting the fact that higher-order transverse modes are generally located at different frequencies compared to the fundamental TEM₀₀ mode. The specific operating frequency and spacing between the higher-order modes depend on both cavity length and mirror ROC, which can be selected to have the least chance of collisions. The general expression for the resonance frequency of any particular longitudinal mode (both rectangular and cylindrical) is given by

$$\nu_{qmn} = \frac{c}{2L} \left[q + \frac{1}{\pi} (m + n + 1) \arccos \sqrt{g_1 g_2} \right]. \quad (3.11)$$

Here, c is the speed of light, L is the cavity resonator length, q is the longitudinal mode number, and m and n are used as the index for the higher order modes as used as the rectangular transverse modes TEM _{mn} , but can be readily replaced by p and l for the cylindrical modes. Finally, g_1 and g_2 are the stability parameters for both individual cavity mirrors, which depend in turn on mirror radius R_i and L .

An important observation is that the higher-order modes can be grouped when the sum $m + n$ is constant, as these sub-groups of modes are located at the same frequency position. Thus it is logical to define the higher-order mode group index k , which describes all possible combinations of higher-order modes for which $m + n = k$ and $p + l = k$, for the rectangular and cylindrical modes respectively. This mode group will here be indicated with label TEM _{k} . Using this and further simplification of Eq. (3.11) by dividing through the FSR, and offsetting the now relative frequency by $\frac{1}{\pi} \arccos \sqrt{g_1 g_2}$, we acquire

$$\gamma_{qk} = q + \frac{k}{\pi} \arccos \sqrt{g_1 g_2}. \quad (3.12)$$

Here, the FSR is set to unity and the last term $\frac{k}{\pi} \arccos \sqrt{g_1 g_2}$ is the higher-order mode spacing as a fraction of the FSR. In general, the smaller the higher-order mode spacing, the less chance of relevant mode collisions, as there will be fewer occurrences when a TEM _{k} mode overlaps with the TEM₀₀ mode. From Eq. (3.12) the higher-order mode spacing can be directly calculated and compared for both the p.c. and c.c. geometries. This shows that there is a slight preference for the c.c. design for small R/L ratios, but disappears for the limit of large ROC.

To analyze a possible mode collision we are not interested in the absolute frequency of the possible (higher-order) longitudinal modes, but in the relative frequency with respect to a TEM₀₀ mode at frequency $\nu_{q_i,00}$. This can be obtained by solving for solutions when $\nu_{q_i,00} \neq \nu_{q_j,k}$, where q_j can be any longitudinal mode. Equating this gives

$$0 \neq q_j - q_i + \frac{k}{\pi} \arccos \sqrt{g_1 g_2}. \quad (3.13)$$

Thus we must find solutions for which this condition is ensured until a large number k , for which straightforwardly many solutions can be found. However, one must consider both tolerances in length and the ROC of the mirror(s), which leads to an uncertainty of the stability parameter g_i , leading to an uncertainty of the higher order mode spacing. The uncertainty Δg_i can be found using first-order Taylor expansions of g_i in both L and R , which are $\frac{\partial g_i}{\partial L} = -\frac{1}{R_i}$ and $\frac{\partial g_i}{\partial R_i} = \frac{L}{R_i^2}$ respectively. The uncertainties ΔL and ΔR are typically linearly dependent on the total value itself and are often expressed as a percentage of the total value. Thus rewriting the two partial derivatives and substituting for $\Delta L = \alpha_L L$ and $\Delta R = \alpha_R R$ gives $\Delta g_{i,\Delta L} = \frac{L}{R_i} \alpha_L$ and $\Delta g_{i,\Delta R_i} = \frac{L}{R_i} \alpha_R$. This can be combined to the total uncertainty $\Delta g_i = \frac{L}{R_i} (\alpha_R + \alpha_L)$. Finally, using the first-order Taylor expansion of Eq. (3.11) in terms of g_i results in the following first-order error for the prediction of the higher-order mode positions as a fraction of the FSR for both the c.c. and p.c. geometries respectively:

$$\Delta \gamma_{qk,cc} = \frac{k}{\pi \sqrt{1 - g_{cc}^2}} \frac{L}{R_{cc}} (\alpha_R + \alpha_L) \quad (3.14)$$

$$\Delta \gamma_{qk,pc} = \frac{k}{2\pi \sqrt{(1 - g_{pc})g_{pc}}} \frac{L}{R_{pc}} (\alpha_R + \alpha_L) \quad (3.15)$$

Note that for the c.c. geometry we assume that both mirrors are identical, such that $g_1 = g_2$. From these equations, it is directly observable that the error grows linearly with the mode group number k , making it ultimately impossible to accurately predict the locations of the higher-order modes when the error becomes larger than the higher-order mode spacing. The results for two cases of R/L for the c.c. geometry and a typical ROC uncertainty of 1% are plotted in Fig. 3.3. From these two cases, it can be seen that the situation in Fig. 3.3(a) is undesired as

3. VIBRATION INSENSITIVE CRYOGENIC CAVITY DESIGN FOR CAVITY-ENHANCED SATURATION SPECTROSCOPY

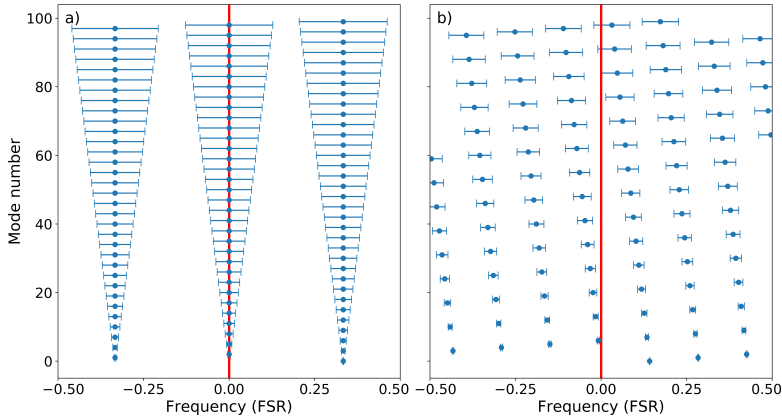


Figure 3.3: Higher-order mode position progression for the first 100 mode groups. Panel a) shows the result of a c.c. geometry cavity of 500 mm length, 1 m ROC mirrors, and 1% uncertainty, leading to a high chance of degeneracies. Notable is also the large higher-order mode spacing of 1/3rd of the FSR due to the large $L_{\text{cav}}/\text{ROC}$ ratio, leading to a possible mode collision for 1 out of every 3 higher-order modes. Panel b) shows the calculation of a 371 mm p.c. geometry with 2 m ROC mirrors, and 1% uncertainty, a possible configuration for our design. The mode progression is such that degeneracy with the TEM₀₀ is unlikely until a large value of k . If a collision occurs, this is isolated to a single incident due to the slope of the progression. The mode spacing is also much more favorable at roughly 1/7th of the FSR.

this can lead to a high chance of collision with the fundamental mode as one in every 3 modes could interfere with the fundamental mode. The situation in Fig. 3.3(b) is much more favorable as the higher-order mode spacing is smaller compared to situation (a). Moreover, the general trend or the higher-order mode progression is off with respect to the fundamental mode. This means that if a collision occurs, it is typically isolated to a single mode group. However, it must be noted that small deviations of the mirror surface from its spherical design might lead to either a spherical deformation of the cavity or possibly a change of the effective ROC depending on the beamsize. This in turn causes a lift of the mode group degeneracy, causing a spread in frequency of these higher-order modes. We have observed this effect in an early version of a c.c. cavity (used in the first version of our HD experiment, described in Chapter 4) which was prone to mode collisions, where closely spaced band structures of an isolated mode group were observed very identical to the observations in Silander *et al.* [101].

For accurate prediction of the higher-order mode positions, one could extract both the FSR and higher-order mode spacing when the cavity is operational. This can be done by using a broadband EOM to scan sidebands over the various higher-order mode positions, which significantly reduces the initially assumed uncertainty. Ultimately, one could use precise thermal control of the cavity resonator to exploit the thermal expansion of the material to fine-tune the length to an area free of mode collisions and maintain this point of operation.

3.3.3 Higher-order mode dampening

Higher-order mode collisions are ultimately unavoidable due to the unpredictability of the higher-order mode positions from tolerances present in both cavity length and mirror radius. On top of that, there is a high chance that higher-order modes become non-degenerate, further increasing the possibility of collisions. Despite the fact that there is little spatial overlap of these higher-order modes with respect to the fundamental mode both incident on and inside the cavity, strong coupling can still be observed [101]. Therefore, it is suspected that the scattering of light from mirror surfaces can be a significant source for these higher-order modes [102]. Thus higher-order mode dampening is another crucial element to further reduce the effect of these collisions when they occur or, preferably, suppress the effect below the detection limit of the setup.

Dampening can be achieved by exploiting the fact that higher-order modes significantly grow in size for increasing mode number and thus can be effectively attenuated by an effective aperture. This aperture can be an actual pinhole inside the cavity, which was used in the study of Silander *et al.*, but any cavity already contains a certain smallest effective aperture such as the cavity bore diameter, the inner diameter of the ring piezo, or ultimately the mirror surface diameter as an upper limit. Besides the effect of higher-order mode dampening, it is crucial to consider that the effective aperture must be sufficiently large to not dampen the TEM₀₀ mode as this will affect the finesse of the cavity. This is also important to consider when choosing the minimum bore diameter of the cavity. Therefore, we first analyze the beam attenuation of the TEM₀₀ mode through a circular aperture, which is given by

$$\frac{P_T}{P_0} = 1 - e^{-2r_a^2/w^2}. \quad (3.16)$$

3. VIBRATION INSENSITIVE CRYOGENIC CAVITY DESIGN FOR CAVITY-ENHANCED SATURATION SPECTROSCOPY

Here P_T/P_0 is the fraction of power transmitted through the aperture, r_a is the radius of the aperture, and w is the radius of the beam size at the location of the aperture. This equation can be rewritten to the fraction of power lost through the aperture and by substituting for the aperture-to-waist ratio $a = r_a/w$

$$\frac{P_L}{P_0} = e^{-2a^2}. \quad (3.17)$$

As reflectivities of mirrors in state-of-the-art cavities approach or even surpass the level of 5 nines ($R = 0.99999$), such as the mirrors used for our H₂ quadrupole studies, the expected roundtrip losses are at the low ppm level. To not significantly alter the finesse of such cavities, the added loss due to the aperture should not exceed 10 ppt, or around two orders of magnitude lower than the expected minimum roundtrip losses. Solving Eq. (3.17) for 10 ppt gives an aperture-to-waist ratio of 3.03, meaning that the aperture must be at least three times larger than the expected beam size. Note that this assumes that the beam passes the aperture exactly through the center, but expected angular tolerances of the mirrors typically shift the beam laterally inside the resonator. This possible lateral shift must be included as an additional circular tolerance zone to the required minimum aperture size.

Transverse modes in a cavity can either occur in cylindrical or rectangular form as discussed in the previous section. While in theory a Fabry-Perot cavity has cylindrical symmetry, which predicts cylindrical longitudinal modes to occur, in reality often only the rectangular modes are observed when the cavity is resonant at a higher-order mode. This might come from the fact that the symmetry is broken due to small tolerances in the mirror ROC or a slight preference for a certain polarization state. Another reason can be that a rectangular mode typically has the highest overlap with the incident beam and thus the highest gain or feedback to the stabilization loop, which forces operation to such a mode and overclasses a 'weaker' cylindrical mode. Nevertheless, both transverse modes must be treated equally as they all may disturb the resonator stability when these mode collisions occur.

Before calculating the attenuation of the higher-order modes, we first define both cylindrical and rectangular modes in cylindrical coordinates for ease of integration over the circular aperture. The cylindrical transverse modes are expressed by

$$I_{pl} = I_0 \left(\frac{2r^2}{w^2} \right)^{|l|} [L_p^{(|l|)} \left(\frac{2r^2}{w^2} \right)]^2 \cos^2(l\phi) e^{-\frac{2r^2}{w^2}}, \quad (3.18)$$

with L_p^l representing a Laguerre polynomial. The rectangular transverse modes can in turn expressed by

$$I_{mn} = I_0 \left(\frac{w_0}{w} \right)^2 \left[H_m \left(\frac{\sqrt{2}r \cos \phi}{w} \right) \exp \left(\frac{-r^2 \cos^2(\phi)}{w^2} \right) \right]^2 \times \left[H_n \left(\frac{\sqrt{2}r \sin \phi}{w} \right) \exp \left(\frac{-r^2 \sin^2(\phi)}{w^2} \right) \right]^2. \quad (3.19)$$

where $H_{n,m}$ are Hermite polynomial functions.

The attenuation from the aperture on the higher-order modes is calculated by performing numerical integration. This is done by first calculating the total power by integrating until a large radius-to-waist ratio (e.g. $r = 25w$) and subtracting this by the integration until the aperture-to-waist radius a . As we are only interested in the fraction of attenuated power by the aperture, both expressions can be further simplified by dividing out the constants and by setting the waist size to unity. To simplify further, the expression for the cylindrical transverse modes is first analytically integrated over the term depended on ϕ , which gives $\int_0^{2\pi} \cos^2(l\phi) d\phi = \pi + \frac{\sin(4l\pi)}{4l}$. As l is an integer, the outcome of this integral will always be π (or 2π for $l = 0$) and can be neglected. The remaining function is strongly divergent for increasing numbers of p and l . To counteract the strong divergence, a normalization factor is included which somewhat counteracts this behavior and makes the integral better behaved. The remaining integral to calculate the transmission through an aperture then becomes

$$\int_0^a \frac{(2r_w^2)^l}{\Gamma(\sqrt{p} + l + 1)} (2r_w^2)^l [L_p^{(|l|)}(2r_w^2)]^2 e^{-2r_w^2} r_w dr_w, \quad (3.20)$$

where r_w is the new variable scaled by the waist size and the Euler gamma function is the empirically found normalization factor. The Hermite polynomials in the expression for the rectangular transverse modes exhibit similar divergent behavior, for which also a normalization prefactor is included

$$\int_0^a \int_0^{2\pi} \frac{1}{(m+n+1)!} \left[H_m \left(\sqrt{2}r_w \cos \phi \right) \right]^2 \times \left[H_n \left(\sqrt{2}r_w \sin \phi \right) \right]^2 e^{-2r_w^2} d\phi dr_w. \quad (3.21)$$

Numerical integration is performed on both expressions and results within a certain mode group are compared. It is expected that the least attenuated mode within a specific mode group will give the largest disturbance, and thus may be the dominating mode within this mode group. Thus the minimum attenuated mode is used as the output of the calculation for comparison between different levels of the aperture-to-waist ratio a . Results for the first 200 modegroups are shown in Fig. 3.4. The results are as expected; for smaller values of a the higher-order modes are attenuated more quickly. It also shows that an aperture-to-waist ratio close to 10, which equals having the full working diameter of a 1/2-inch mirror exposed to the cavity, is highly unrecommended as even mode groups as high as $k = 100$ are not sufficiently attenuated. While it is obvious from these calculations that the smallest allowable value of a is preferable for maximum higher-order mode dampening, it must be noted that this aperture size is often impractical to use due to slight tolerances and expected beam deviations from the center of the cavity, which might lead to significant attenuation of the fundamental mode.

3.4 Cryogenic cavity design for high roundtrip powers

3.4.1 Introduction

In this section, we will discuss the design of a full-cryogenic cavity suitable for high-power and high-resolution saturation spectroscopy. By 'full' we mean that the entire cavity, including the mirrors, will be cryogenically cooled. While technically more challenging than only having a cryogenic volume inside a room-temperature cavity, the advantage is having a more compact and mechanically rugged design which ultimately leads to a more stable design. This stability is required to reduce the linewidth of the cavity to levels where the contribution to the observed lineshapes becomes insignificant, which is warranted in high-resolution spectroscopy.

3.4. Cryogenic cavity design for high roundtrip powers

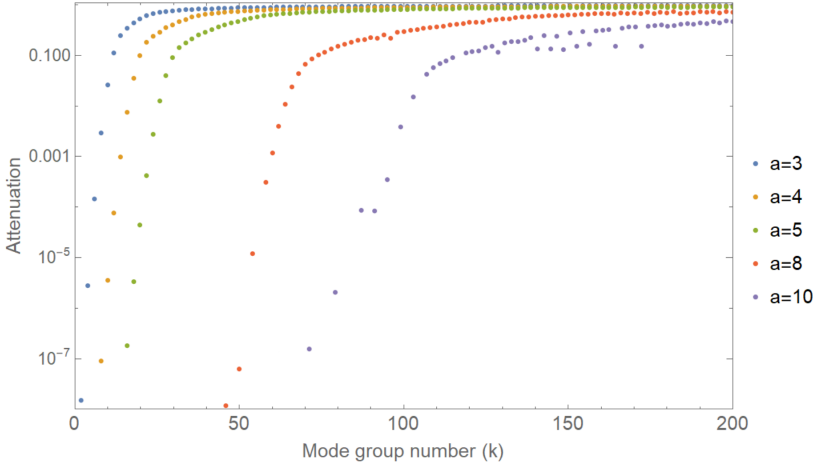


Figure 3.4: Calculated mode attenuation for mode-group TEM_k for each even number of k for varying values of the aperture-to-waist ratio a . Some calculated results deviate slightly from the expected trend due to numerical errors from the highly oscillating integrand.

The unique combination of high-roundtrip power with cryogenic temperatures is a new challenge as the heat dissipation from the laser becomes significant and deviates from the cryogenic implementations to cavities so far. It must be noted that the cryogenic regime is a broad range, where systems performing at 4 K (e.g. [98, 103]) will have other challenges and considerations than the 50 K limit on which this cavity is based. We will discuss some cryogenic and high-power design considerations before proceeding to the cavity design itself.

3.4.2 Material selection

Metals are a preferred choice over other common and suitable cavity materials such as Zerodur[®] or ultra-low expansion glass due to the ease of machinability and the requirement of bolt connections due to the necessary vacuum sealing at the cavity level. Therefore, we will mainly focus on metals in the discussion.

Some physical properties of materials can change drastically when cooled down to cryogenic temperatures, which will have direct consequences on the design choices and render some materials unsuitable for cryogenic use. The first important observation for metals is that only metals exhibiting a face-centered cubic structure are cryogenically compatible, as

3. VIBRATION INSENSITIVE CRYOGENIC CAVITY DESIGN FOR CAVITY-ENHANCED SATURATION SPECTROSCOPY

these metals do not have a ductile to brittle transition temperature [104]. Metals that do carry this property can become brittle and fail when stressed, thus being unreliable under cryogenic conditions. This mostly holds for some alloys of stainless steel, but most common metals such as iron, copper, aluminum, and austenitic stainless steel are suitable for cryogenic use.

Thermal expansion is another mechanical property to consider, which becomes significant for most materials at cryogenic temperatures. Most materials contract when cooled down, but there is a strong variety of the total integrated thermal expansion along the different materials. For example within metals, where the alloy Invar has a total contraction of only 0.02%, while aluminum experiences a contraction of up to 0.4%. Perhaps more important is the differential thermal expansion between different materials, which can lead to unexpected changes in stress or loosening of components. A common example of this effect is the loss of bolt tension, where the bolt contracts less than the material it is bolted to. This will happen when using stainless steel bolts with copper and aluminum, but even minute differences in the composition of stainless steel alloys can cause this effect to occur. In our design, we apply spring disk washers at each bolt connection with sufficient spring constant and actuation length to counteract this effect.

Thermal properties of materials also undergo dramatic changes. The heat capacity of most materials will drop several orders of magnitude below 100 K, which can have consequences for thermal feedback loops or when relying on the heat capacity for dampening thermal fluctuations through a thermal low-pass filter. While the thermal conductivity of most materials reduces when cooled down, there are a few materials with very specific or opposite behavior. The most notorious example is pure oxygen-free high thermal conductivity (OFHC) copper, where the conductivity can increase over an order of magnitude at around 10 K compared to room temperature. However, the significantly more affordable electrolytic tough pitch (ETP)-copper performs only marginally less at our anticipated lower limit of 50 K. Also aluminum still has a decent performance at these temperatures, while alloys based on iron typically become very poor conductors and could be considered insulators.

At first glance, Invar seems preferable among the metals as a cavity material as it exhibits the lowest thermal expansion of all metals; an often desired property for any cavity. However, when considering the sometimes high roundtrip powers involved in saturation spectroscopy the

3.4. Cryogenic cavity design for high roundtrip powers

heat dissipation inside the cavity and thereby the thermal conductivity of the cavity becomes a crucial factor. Especially in our case where we anticipate up to 10 kW of roundtrip power, the heat dissipation of laser power in the mirrors and cavity resonator due to absorption and scattering losses become significant at up to a few 100 mW.

To better analyze the cavity material behavior and the consequence of sudden additional laser heating, we performed a finite element method (FEM) using Comsol Multiphysics[®]. Here, we define a simple cylindrical element of 75 mm diameter and 400 mm length, mimicking the anticipated cavity dimensions, with a heatsink connection defined at the bottom center of the cylinder which was set at 50 K. An anticipated heat load of 500 mW was divided into 50% bulk heating, mimicking scattering loss, and 25% heating at both ends of the cylinder, mimicking mirror absorption losses. A comparison between ETP copper, aluminum 6081, 304 stainless steel, and Invar was made. The simulation uses the material-specific thermal expansion, heat capacity, and conductivity at the simulated heatsink temperature of 50 K. First, a stationary solution was performed from which the expected total expansion of the cavity and the maximum temperature difference along the cavity were retrieved. Secondly, a time-dependent solution was performed to obtain information on the thermalization time by retrieving data on the thermal expansion as a function of time. This data was fitted by an exponential function, from which the derivative can be calculated to find when the drift rate drops below $1 \times 10^{-13} \text{ s}^{-1}$, which is equal to a drift rate of around 100 Hz/s in the optical domain. The results are listed in Table 3.1 below.

Table 3.1: Simulation results of the effect of induced laser heating of 500 mW on different possible materials for the anticipated cavity design of 400 mm length with a 50 K heatsink. Results show the total thermal expansion, the settling time before the cavity drift rate is less than $1 \times 10^{-13} \text{ s}^{-1}$, and the maximum temperature difference (ΔT) along the cavity resonator.

Material	Total expansion (μm)	Settling time ($\times 10^3 \text{ s}$)	ΔT (K)
ETP copper	7.9	21	0.06
Aluminum 6081	9	17	0.24
SS 304	29.2	89	9.9
Invar	6.6	100	16.5

3. VIBRATION INSENSITIVE CRYOGENIC CAVITY DESIGN FOR CAVITY-ENHANCED SATURATION SPECTROSCOPY

These results directly show that both copper and aluminum have a clear preference as materials for the cavity. Both stainless steel and Invar are affected by their reduced thermal conductivity, where the total thermal expansion of Invar even comes near that of aluminum and copper. The significantly longer settling times and large expected thermal gradients make them a less ideal choice. Noteworthy is that even though copper has a much higher thermal conductivity than aluminum, the higher heat capacity limits the total settling time. Note that the total expected expansion due to laser heating at high power exceeds the expected actuation length of the piezo at around $2\ \mu\text{m}$. This means that thermalization to a certain level is a required period before the experiment can start to operate at these power levels as the piezo is not able to compensate for this expansion. When looking for the time for when the remaining thermalization is less than $2\ \mu\text{m}$, we see that for both copper and aluminum, this is around 30 minutes, while for stainless steel this is nearly 6 hours. From this analysis, we conclude that aluminum is the preferred material for our anticipated use case. The cryogenic performance is close to that of copper, while it has clear advantages due to the reduced weight, ease of machinability, and durability due to the higher strength of the threaded holes.

3.4.3 Other cryogenic design considerations

Vacuum sealing at the cavity level is required to contain the molecular gas of interest inside the cavity and maintain a high-vacuum outside of the cavity. However, ordinary O-rings of rubber or Viton are unsuited for cryogenic use and a copper knife-edge seal is both too macroscopic in size and vulnerable due to the limited durability of aluminum. Therefore, we opt for indium wire sealing as this has been proven to be a reliable method of vacuum sealing under cryogenic conditions. As indium is significantly softer than aluminum, there is no risk of damaging the aluminum parts on which a direct vacuum seal is required. It has also been shown that indium can create reliable and vacuum-tight seals directly on glass surfaces.

Flexible thermal links are used to mechanically decouple the cryocooler from the cavity due to the thermal contraction of the cryogenic parts and to dampen the vibrations from the cryocooler. In total a series of 3 flexible links will be included at strategic points to have the desired decoupling while maintaining sufficient conductivity. The thermal straps

(Technology Applications Inc.) are constructed of OFHC copper with extremely flexible stranded copper wiring, providing flexibility along all degrees of freedom.

3.5 Cavity resonator design

3.5.1 Linear cavity

The linear cavity is in its essence a stable and parallel interconnection between both cavity mirrors. Typically any means of active alignment of the mirrors is avoided to increase the mechanical stability and reduce the complexity and size of the cavity. Depending on the anticipated mirror ROC and cavity length, this puts stringent requirements on the parallelism of the parts and connecting surfaces participating in referencing the high-reflective side of the mirrors with each other. To obtain the highest degree of parallelism, we opt for a configuration where the ring piezo will be at the front side of the mirror, thus located in between the two mirrors. In this configuration, only two parts are necessary between the two mirrors, the piezo and the cavity resonator itself. In our design, we include an additional spacer identical in size to the piezo at the un-actuated mirror side. This is for reasons of symmetry in the mechanical design and it allows some level of alignment if necessary by use of angled spacers.

The cavity itself is made of aluminum 6081 as this resulted as the best option from our material analysis. The general shape is a cylinder of 400 mm length of which the outer profile is of octagonal shape resulting from the intersection of a 77mm diameter circle with a 72mm square. The effective cavity length is 371 mm, with a cavity bore diameter of 10 mm. This length was chosen from a combination of mechanical size constraints on the optical table, analysis of the higher order mode avoidance and the 404 MHz FSR matched commercially available bandpass filters, which was convenient for the implementation of NICE-OHMS. The whole part was machined in a single continuous tooling path on a 5-axis milling machine using a single setup to obtain the required level of parallelism of less than 0.01° between the two mirror supporting and referencing surfaces. The cavity in its assembled form is displayed in Fig. 3.5.

The ring piezo is a custom assembly based on the standard PICMA

3. VIBRATION INSENSITIVE CRYOGENIC CAVITY DESIGN FOR CAVITY-ENHANCED SATURATION SPECTROSCOPY

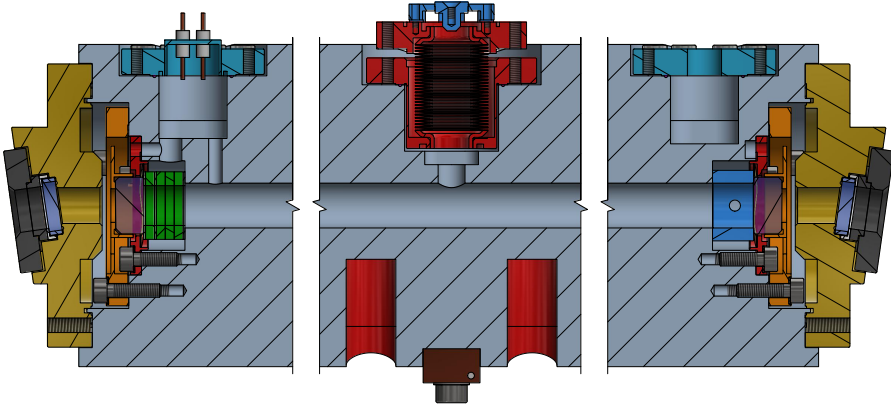


Figure 3.5: Technical illustration of a side-view midplane cut-through along the assembled cavity. The left (front) side of the cavity is piezo-actuated (piezo stack is colored green) and is outfitted with an electric feedthrough on top (cyan). The right (back) side of the cavity is un-actuated and consists of a spacer (blue) and is outfitted with a near identical feedthrough flange for symmetry reasons (blue). At both sides the piezo/spacer and mirrors are clamped against the cavity resonator using separate spring mounts (red and orange). The cavity is vacuum sealed at both ends with a windowed flange. At the top center the vacuum connection with a flexible bellow is situated (red). At the bottom center the thermal connection and temperature are situated (brown). Next to the thermal connection points are two material cut-outs (red) necessary to symmetrize the bending strength of the resonator for optimization of vibration sensitivity.

PD150.3x element from PI (Physik Instrumente). This ring element has an outer diameter of 15 mm, an inner diameter of 9 mm, and 2 μm actuation length at room temperature. The 9 mm inner diameter of the piezo is also the smallest aperture within the cavity roundtrip. Our custom assembly consists of two separate segments; a triple stack consisting of 3 PICMA elements for slower and coarse high-voltage control and a single stack for faster low-noise low-voltage control. Splitting these functions over two separate segments has advantages in terms of controlling the piezo as high-voltage amplifiers typically suffer from ripple and noise. In this segmented configuration, the HV amplifier is solely needed for an offset voltage and canceling slow drifts as faster locking and modulation are performed by the low-noise low-voltage amplifier. Therefore, the HV amplifier can be strongly low-pass filtered to reduce any residual noise and significantly improve the instantaneous linewidth of the cavity. Previous studies have shown that piezo-activated cavities through

this methodology can reach performances nearing the fixed ultra-stable cavities [105].

The tuning range of a piezo is given by $-\nu_c/2L\delta L$, where ν_c is the absolute frequency of the laser carrier wave, L the cavity length, and δL the actuation length of the piezo. For ease of operation, it is desired to have a piezo with an actuation length that can span at least 2 times the FSR of the cavity, as this will result in having two accessible resonant modes at all times. Thus for the desired actuation length of $2 \times \nu_{\text{FSR}}$, we can readily find that the actuation length needs to be 2 times the operation wavelength of the laser. The actuation length in this design is mostly determined by the triple-stack at around $6 \mu\text{m}$ actuation length at room temperature. However, the displacement length of a piezo changes significantly when cooled to cryogenic temperatures [106]. For the used PICMA actuator in our setup, the actuation length is reduced to around 35% at 77 K. Fortunately, from this temperature and lower this piezo is allowed to be driven in a bipolar configuration (-100 to 100 V), effectively doubling the reduced actuation length. As a result, even at temperatures as low as 20 K still about a third of the original actuation length can be covered using a bipolar drive. This is sufficient to recover the desired 2 times the FSR at common wavelengths of around 1500 nm for our selected piezo configuration.

The piezo element, consisting of two alumina end disks, is directly clamped onto the aluminum resonator using a soft so-called wave spring washer with an inner diameter larger than the mirror diameter (Fig. 3.6). This allows the removal of the cavity mirrors without the removal of the piezo itself and omits any glue bonding of the piezo with the cavity resonator. Electric connection is done through a cryogenic compatible 4-pole feedthrough (Ceramtec 9299-05-W), which is welded in a custom stainless steel flange for the necessary indium wire seal.

The cavity mirror is centered and clamped against the piezo through spring action from the custom mirror mount (Fig. 3.6). This has the advantage that permanent glue bonds are omitted and cavity mirrors can be readily interchanged. Next to the spring action of the mount, it also serves as a thermal link between the mirror substrate and the cavity resonator. This is necessary as heating can become significant as discussed in the previous section and the piezo itself is a poor thermal conductor.

The mirror mount is made from aluminum with a custom-designed spring element with an anticipated spring constant of around 300 kN/m,

3. VIBRATION INSENSITIVE CRYOGENIC CAVITY DESIGN FOR CAVITY-ENHANCED SATURATION SPECTROSCOPY

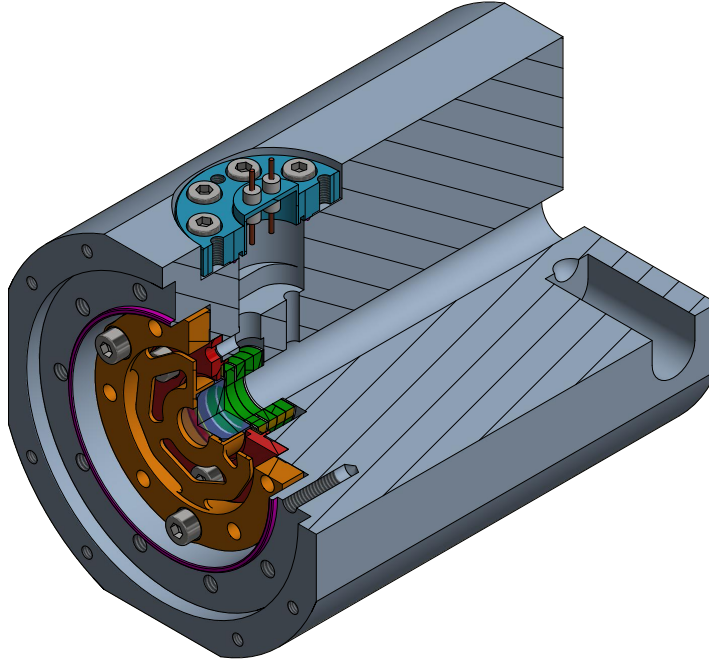


Figure 3.6: Technical illustration of a three-quarter cut-through of the piezo-activated side of the cavity without the windowed flange. The piezo stack is separately clamped to the cavity by a wave spring washer and a separate clamping disk (red). The mirror is clamped onto the piezo with a custom-made spring mount (orange). The ridge on the end of the resonator (magenta) is used for the indium wire vacuum sealing with the end flange. The material cut-out at the side is one of the four mounting support point of the cavity, which is at the midplane and near the center for reduced vibration sensitivity.

resulting in an expected clamping force of around 110 N. A modal analysis using a FEM simulation in Autodesk Inventor[®] of the mirror mount including the mass of the mirror, resulted in a first mechanical resonance at 1.9 kHz. This simulation excludes the possible effect of clamping against the piezo, from which we expect to further increase the resonance frequency. The expected locking feedback bandwidth and modulation frequency are significantly lower than this resonance frequency.

At the opposing non-actuated side of the cavity, a stainless steel spacer identical to the dimensions and mass of the piezo is included. This allows fine-tuning of the mirror angle by use of slightly angled spacers if necessary. It also symmetrizes the design, which is important for the concept of the vibration immune mounting method, discussed in the

following section. This symmetrization is continued by also including a flange identical in mass to the electric feedthrough flange for the piezo. A flexible vacuum connection is made at the top of the cavity. This consists of a custom flexible edge-welded bellow welded inside a stainless-steel flange for the indium wire seal. This assembly is embedded within the cavity to save space. On the opposing side at the bottom the flexible thermal link, temperature sensor, and an SMD heating resistor are situated at the center. Directly next to this, two material cut-outs are made to adjust the mechanical bending strength of the cavity to compensate for the loss in strength due to the opposing hole for the bellow assembly. This symmetrization was necessary to find an optimum support point that optimizes the vibration sensitivity in all directions. This will be further discussed in the following section.

The cavity is vacuum-sealed at both ends with a windowed flange consisting of an angled wedged AR-coated window of N-BK7 (Thorlabs WW11050-C), as fused silica has strong OH absorption bands at the anticipated working range for the HD spectroscopy studies. The window is indium wire sealed inside the end flange, which in turn is indium wire sealed to the cavity.

3.6 Vibration immune cavity mount design

An often overlooked aspect of the design of optical cavities, particularly within the field of cavity-enhanced spectroscopy, is the method of mounting the resonator to the surrounding environment. Most designs are based on a solid and straightforward interconnection between the cavity and the surrounding setup, where typically the cavity is supported from below. This way of mounting is often sub-optimal as vibrations within the setup directly transfer into the cavity causing quasi-static deformations of the cavity, leading to length and thus frequency fluctuations [94]. Reducing the linewidth of the cavity in such a configuration requires significant effort to reduce vibrations of the entire setup. An alternative solution would be to design a cavity that is immune to vibrations by design, which has been extensively researched within the field of ultra-stable reference cavities [93, 95, 98, 107], where support is performed on the symmetry planes of the cavity. However, many of these solutions rely on solutions that are impractical to incorporate in the more traditional cavity design used for cavity-enhanced spectroscopy

3. VIBRATION INSENSITIVE CRYOGENIC CAVITY DESIGN FOR CAVITY-ENHANCED SATURATION SPECTROSCOPY

and the acquired performances are beyond our requirements. Nevertheless, the progression of cavity-enhanced saturation spectroscopy towards higher-finesse combined with weaker and narrower transitions does benefit from narrow linewidth cavities. Especially when considering active cryo-cooling where vibrations from a cryocooler are unavoidable.

An alternative and simpler approach would be to only optimize the discrete support points of the cavity, which has been studied by Nazarova *et al.* [94]. As a cavity of cylindrical shape is often supported by four points, symmetrically mirrored along the two vertical planes, one could look for an optimum position along the cavity body for these specific points where a vertical acceleration does not induce a length change of the cavity. The consequence of supporting at discrete points compared to a whole support plane is that next to a length change also tilting of the mirrors along the support points must be considered as an effective length change. Through a FEM analysis, an optimal position can be found that minimizes both effects. Nazarova *et al.* found that this approach resulted in a reduction of the vertical acceleration sensitivity of two orders of magnitude compared to an already optimized support position from below where the cavity support was optimized to keep the mirrors parallel under vertical acceleration, the so-called Airy points [108]. Even larger effects can be expected for cavity designs that do not have any form of optimization present in their respective mounting solution. While the study was performed on a cavity that is highly symmetric, homogeneous, and straightforward in its design, the concept can be extended to a symmetric object of any shape.

A limitation of the original study [94] was that only optimization in one direction was performed due to the inflexibility of modifying the cavity shape. This led to having their support points below the horizontal plane, which is suboptimal for optimization of the acceleration sensitivity along both horizontal axes. Our approach is to fix the support point at the horizontal midplane and only vary the position along the axis of the cavity, while also varying the dimensions of a blind hole cut-out in the bottom of the cavity to vary the bending strength of the cavity and tune the mass distribution. By this approach, simultaneous optimization for the y and z -axis can be achieved as the support remains at the horizontal midplane. Another limitation in the study of Nazarova *et al.* [94] is that the support points are on the edge of the cavity cylinder and thus far from the center of the cavity. If one considers acceleration along the x -axis, the cavity is supported far from the midplane, and

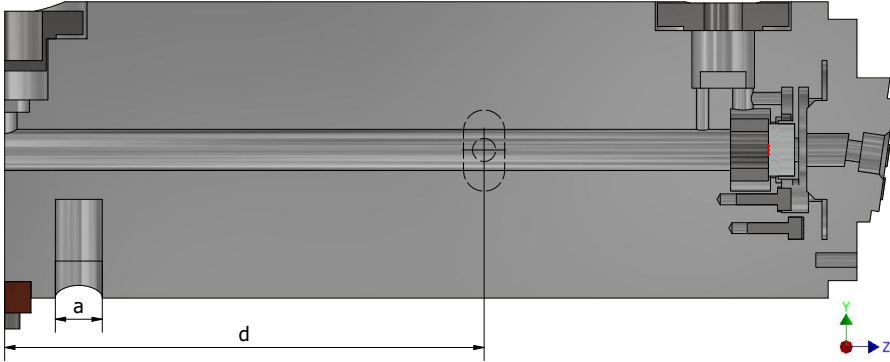


Figure 3.7: Technical illustration of the heavily simplified model used in the FEM simulation. All aluminum parts were combined into a single body. Small volumes were minimized while maintaining the mass distribution of the original design. The three indicated red points on the mirror were tracked in movement along the z -axis when undergoing acceleration along the y -axis, to investigate both expansion along the cavity axis (center point) and angular tilt of the mirror. Dimensions a and d were varied during the simulations to iteratively find the optimum parameters to minimize both the expansion and tilt.

significant acceleration sensitivity is expected along this direction. Our approach is to move the support points as close as possible to the optical axis to be closer to the yz -plane. Full optimization along the x -direction is difficult if not impossible to achieve through this way of mounting, but reduced sensitivity to acceleration along the x -axis should be expected. The method of mounting and supporting our cavity has been modified to the design of Nazarova *et al.* [94] to be suited for cryogenic operation and have more predictable support at the exact intended point as used and found in the simulations. In the original study, Viton hollow cylinders were used as the contact material between the spring wires and the upper half of the blind holes on the side of the cavity. Here, we use a half-circular cutout in which a smaller diameter half-circular dome from Polyether ether ketone (PEEK) is fitted (see Fig. 3.9). The PEEK supports are fitted on custom-made stainless steel spring rods and are pressed along the axis of the spring wire into the cavity to ensure contact and support close to the center of the half-circular cutout. A detailed description on the spring support can be found in the next section.

To perform the necessary FEM simulations (Comsol Multiphysics[®]), the 3D model needs drastic simplification to reduce the number of parts and simplify individual parts to avoid thin elements to simplify the mesh.

3. VIBRATION INSENSITIVE CRYOGENIC CAVITY DESIGN FOR CAVITY-ENHANCED SATURATION SPECTROSCOPY

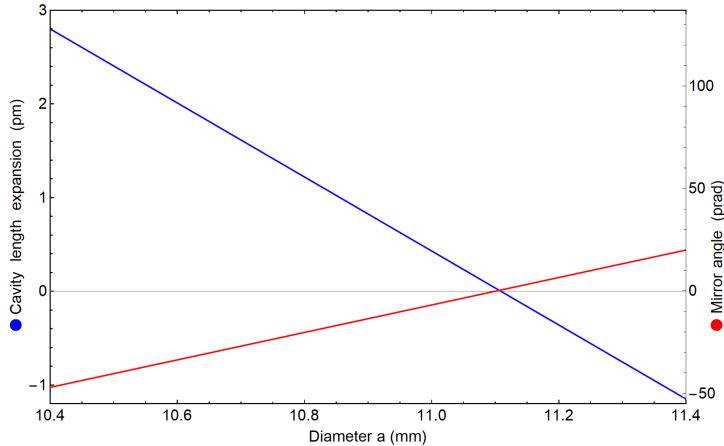


Figure 3.8: FEM simulation result of a parametric sweep of diameter a with $d = 116.44$ mm for both total cavity expansion and mirror angle at a static acceleration of -1 m/s² along the z -axis

However, care must be taken to keep the mass balance and size of the parts and assembly identical to the original counterparts to be able to translate the simulation result to the real design. All individual interconnected aluminum parts were merged into one solid to remove interconnecting boundary surfaces. Other parts were modified by removing sharp boundary edges to avoid the necessity of a small mesh size while maintaining the overall mass profile (Fig. 3.7).

To simulate the acceleration sensitivity of the cavity along the y -axis a similar approach was followed as in Ref. [94], where two vertical symmetry planes were identified to reduce the simulation to one-quarter of the cavity. Our cavity can be considered sufficiently symmetric along these planes as care was taken to symmetrize the design along the z -axis. As the two symmetry planes restrict any horizontal movement, only restriction along the y -axis by the remaining mounting point is required. Here it must be noted that the boundary surface defined in Ref. [94] over-constrains the simulation, as the whole upper half of the circular blind hole was restricted for vertical movement. This boundary condition restricts any rotation over the mounting points along the x and z -axis at the point of support, while this movement is unrestricted in the actual situation. In our simulation, we take a point as the support contact as this allows rotation along all directions and better replicates the actual

situation.

Before starting the simulations on our design, we first replicated the study of Nazarova *et al.* [94] by redrawing their cavity and performing similar simulations. We indeed found identical results, confirming the settings in the FEM simulation. In the simulation of our design, we defined 3 points on the mirror surface along the vertical midplane to track the movement along the z -direction when the cavity undergoes a static acceleration of -1 m/s^2 along the z -axis (Fig. 3.7). The support point was defined at the exact center point of the half-dome cut-out (Fig. 3.9). Optimum positions for dimensions $d = 116.44 \text{ mm}$ and $a = 11.11 \text{ mm}$ for when both cavity length expansion and mirror tilt are near zero were found by performing parametric sweeps iteratively (Fig. 3.8). However, these simulation results are unique to this specific design.

3.6.1 3-axis spring mount

To provide reliable and flexible support at the anticipated support points, a novel spring mount was designed which has flexibility and spring action along all degrees of freedom (Fig. 3.9). A custom-made conical spring rod of stainless steel provides spring action along the y -axis and z -axis, while a combination of two opposing compressed clover dome springs provides spring action and a compressive force along the x -axis. A constant compressive force along the x -axis is necessary as this guides and presses the PEEK supports into the center of the half-circular cut-out support point of the cavity, providing a reliable and well-defined mounting point. Secondly, when cooling to cryogenic temperatures, the differential thermal expansion of materials requires a level of flexibility at the supports. This is acquired by pre-loading the frontward-facing clover dome spring with a tension bolt, which pushes the plunger of the spring wire forward inside the barrel. An ordinary compression spring provides some initial compressive force during installation but becomes fully compressed and obsolete when the system is tuned.

To compensate for the expected bending of the spring rods after supporting the cavity with an expected deflection of nearly 0.5 mm , the spring wires are mounted at an upward angle of 1.5° . This results in a normal incident support angle to the cavity yz -plane at the end of the spring wires. Secondly, the spring rods are tilted inward horizontally with a 2.5° angle to avoid a point of instability as the stronger clover

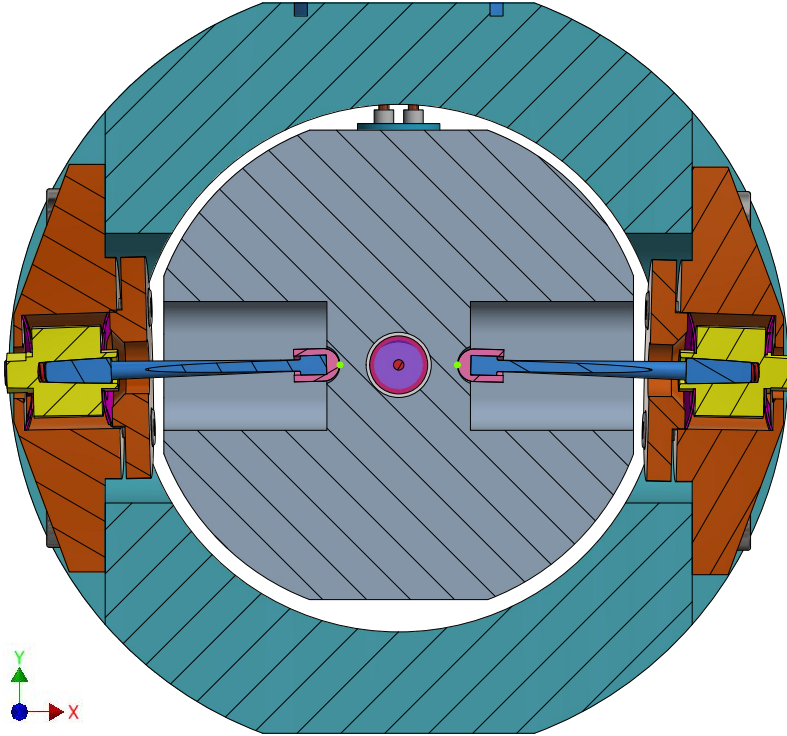


Figure 3.9: Technical illustration of a cut-through of both the cavity (light-blue) and primary-shield (turquoise) along the cavity supports. It shows the cavity in the center supported by the spring-mount design. The spring-mount base (orange) is mounted to the primary shield, in which two compressed cloverdome springs (magenta) holds the spring-rod mount (yellow). The stainless steel spring rod (blue) is pre-compressed with a compression spring (red) from the backside. At the tip of the spring rod is a circular PEEK spacer (pink), providing a smooth support contact with the cavity at its anticipated support point (green point).

dome springs can deflect the spring rods sideways when all supports are at normal incidence to the z -axis (Fig. 3.10).

3.7 Cavity shields and supporting structures

3.7.1 Primary shield

The cavity is housed inside a surrounding encapsulating structure called the primary shield (Fig. 3.9 and 3.10). The spring mounts are directly

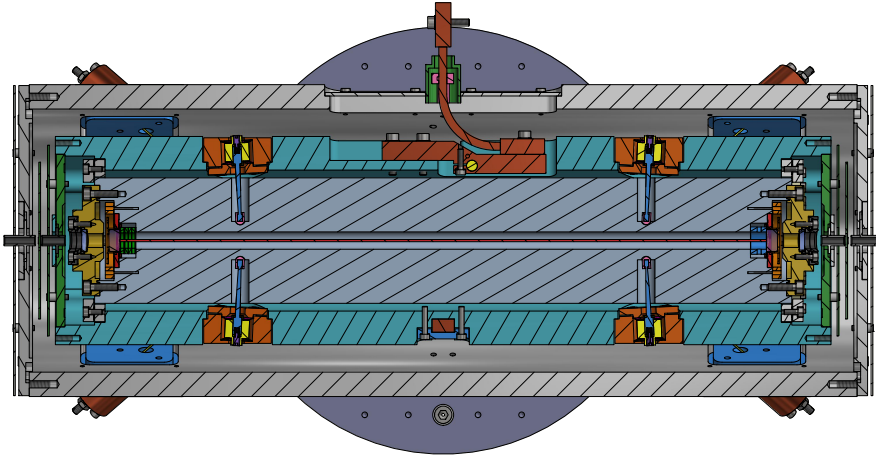


Figure 3.10: Technical illustration of a top-view midplane cut-through of the complete cavity assembly with supporting structure, consisting of the cavity, primary-shield, and secondary-shield. The 4 spring rods are facing slightly inwards. At the top side of the image is the thermal connection towards the cryo-cooler, consisting of a copper block with a thermistor and cartridge heater and flexible thermal link. The thermal link is clamped by a PEEK clamp (pink) to the secondary shield to dampen the remaining vibrations. Visible in the bottom half of the secondary shield are the four positioning rods with the eddy-current dampeners.

mounted onto this structure and cause the cavity to be fully lifted inside the primary shield, ensuring mechanical and thermal decoupling. The primary shield itself is a hollow cylinder of 120 mm in diameter, 450 mm in length, and made of aluminum. A flexible thermal link to the cavity is made at the right side in Fig. 3.11, where the connection towards the cryocooler is situated at the opposing end through a copper interconnection piece which houses both a PT100 temperature sensor and cartridge heater (see also top of Fig. 3.10). This interconnection point is also where the temperature stabilization will take place through a PID feedback loop. As the primary shield is situated in between the temperature-stabilized thermal interconnection point and the thermal linkage to the cavity, the heat capacity of the shield acts as a thermal low-pass filter for the cavity. The effect of this low-pass filtering is studied in the following section.

The flexible vacuum connection of the cavity is decoupled at the primary shield to a rotating flange before proceeding further with a second flexible bellow (Fig. 3.11). This angled flange of stainless steel is pressed

by a wave spring into a similarly angled bronze bushing and lubricated with Apiezon[®] N. The rotary mount provides mechanical decoupling of the cavity vacuum connection from the environment by a strong interconnection with the primary shield, while providing the necessary rotational degree of freedom along the axis of the bellow.

As the primary shield fully covers the cavity, except for the optical entrance and exit hole, it serves as a radiation shield from the room temperature environment. The whole primary shield assembly is wrapped in 5 layers of aluminum-coated mylar foil and polyester netting to provide separation between the mylar layers.

3.7.2 Secondary shield

The primary shield is mounted inside a secondary structure, called the secondary shield (Fig. 3.11 and 3.12). This structure is at room temperature but still acts as a low emissivity shield as the inward-facing surfaces are provided with a layer of highly reflective aluminum-coated mylar. The primary shield itself is levitated by two thin stainless steel rods of 1.5 mm diameter, acting simultaneously as a thermal insulator. These upward-facing rods are supported by two multiwave springs to provide additional dampening of the cavity assembly and mounting flexibility due to the significant thermal contraction of the primary shield and the stainless steel rods. Multiwave springs are specifically chosen for this situation as these exhibit a combination of a decent low spring constant with a long actuation length, while simultaneously being wider than their length; making them mechanically stable. The total weight of the primary shield is estimated at around 13 kg, which combined with the spring constant of 18.9 N/mm results in a mechanical resonance frequency of around 9 Hz for the vertical direction. Additionally, 4 multi-wave spring-loaded positioning rods facing downward with a 120° outward facing angle are included to have a higher degree of mounting accuracy as otherwise, the cryogenic assembly will move upwards under the thermal contraction. These additional downward-facing positioning rods also provide better positional accuracy as they restrict an otherwise undampened pendulum.

Common methods of dampening are incompatible as the original design intended to allow pre-cooling of the secondary shield with liquid nitrogen, which excludes the use of ordinary materials like Viton or Sorbothane. Next to that, the resulting contraction of the cryo-cooled

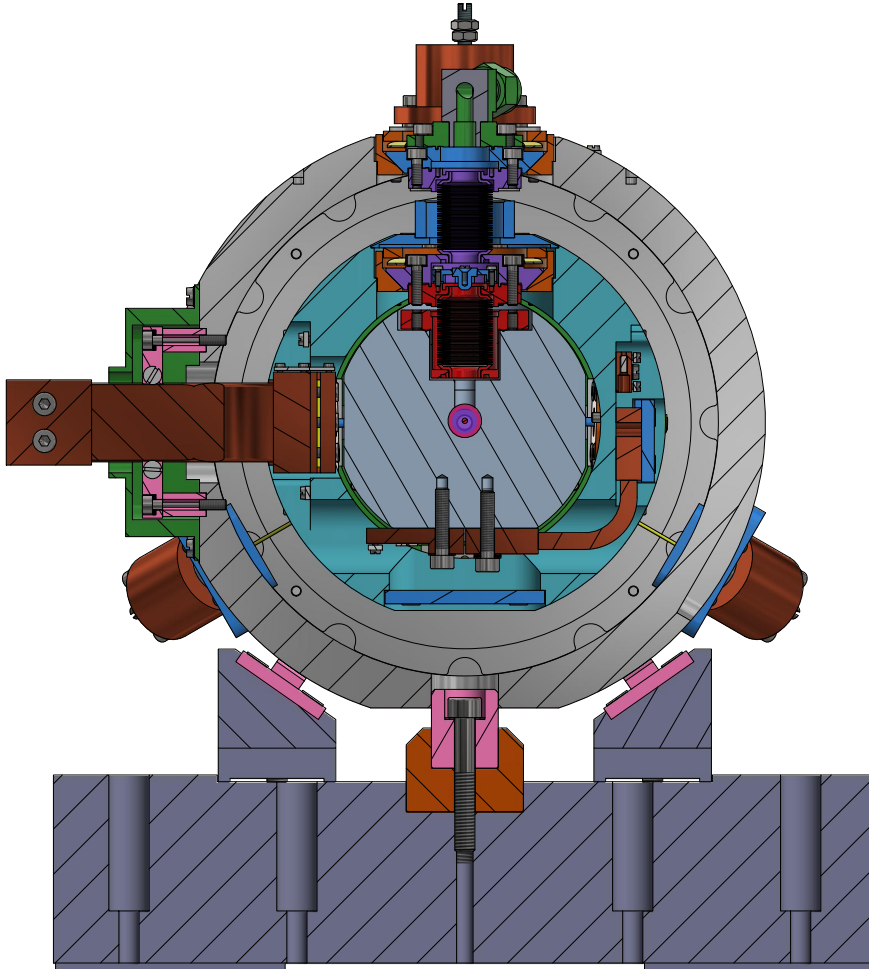


Figure 3.11: Technical illustration of a front-view midplane cut-through of the complete cavity assembly with supporting structure, consisting of the cavity, primary-shield, and secondary-shield. The whole assembly is supported at the bottom by a V-mount structure, consisting of 4 PEEK sliding pads (pink) and a central reference cylinder (pink). The two stage vacuum feedthrough is visible in the top center, consisting of a series of two flexible bellows and rotatable flange design to allow rotation along the bellow axis.

3. VIBRATION INSENSITIVE CRYOGENIC CAVITY DESIGN FOR CAVITY-ENHANCED SATURATION SPECTROSCOPY

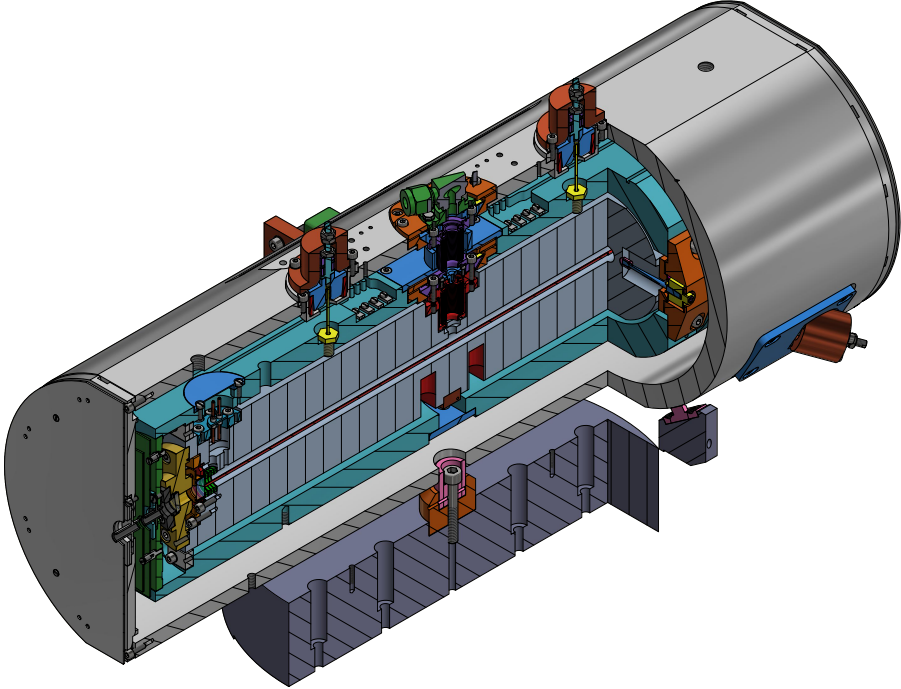


Figure 3.12: Technical illustration of a three-quarter view of the complete cavity assembly. Visible is the whole mounting structure down from the optical table level until the spring-rod mounted cavity.

assembly necessitates the use of a dampener that does not induce a force for a positional change. Therefore, we included custom-designed magnetic dampeners, which work by the eddy current effect induced in the conductor surrounding the moving magnet. These dampeners are particularly suited for cryogenic applications as typically the conductivity of the relevant conductor and the magnetic field of the permanent magnet both increase when cooling down. The two permanent neodymium magnets were mounted in line with the stainless steel rods and with the poles facing each other, as this creates a stronger outward-facing magnetic field toward the surrounding copper cylinder. No specific calculations were performed to design these dampeners, but from tests at room temperature using a high-speed camera, it was found that the decay time of the oscillation was roughly halved compared to the undamped situation.

The vacuum feedthrough towards the cavity is again decoupled at the

secondary shield by an identical rotation allowable mount. This gives the vacuum connection to the cavity full flexibility along all degrees of freedom, without inducing any disturbance or remaining net force from the rigid metal bellow hose connection to outside the main vacuum chamber.

3.8 Cryocooler assembly, vibration isolation and temperature control

The cryocooler used in this study is a thermo-acoustic sterling cryocooler (Rix Industries Qdrive 2S132K-FAR). While the single thermodynamic cycle only allows cooling down to 40 K as a limit, the advantage is the lack of vibrations and noise normally present with pulsed tube cryocoolers. The dual-opposed motor/piston design within the pressure wave generator is balanced, reducing vibration and noise, and is separated from the static coldhead by a flexible bellow hose to further reduce vibrations. Next to the reduced amplitude of vibration, the system operates at a relatively high frequency of 60 Hz. This allows for the convenient use of spring-mass dampeners to further reduce the remaining vibrations.

The cryocooler coldhead is situated on an external frame next to the setup and optical table (Fig. 3.13), while the cryocooler pressure wave generator is installed on a separate frame, which is dampened from the ground. The shared vacuum of the coldhead with the setup for the required insulation is vibrationally decoupled through two stages of bellow connections to acquire full flexibility in all degrees of freedom. The first bellow isolation stage is a combination of two opposite balanced bellows around a spring-levitated vacuum cube, situated vertically directly underneath the cryocooler coldhead. The second bellow below the vacuum cube is connected to the turbo pump (Pump speed - 80 l/s) responsible for maintaining the vacuum. As both bellows are identical, the force resulting from the vacuum cancels out and the centered cube becomes a spring-mass system solely determined by the four springs levitating the vacuum cube. The resulting resonance frequency is around 9 Hz, significantly reducing the transmission of the vibrations from the cryocooler. A second bellow isolation stage connects the spring-levitated vacuum cube with the main vacuum chamber on the optical table. The significant vacuum force is balanced by three compression springs situated

3. VIBRATION INSENSITIVE CRYOGENIC CAVITY DESIGN FOR CAVITY-ENHANCED SATURATION SPECTROSCOPY

around the bellow in between the vacuum cube and a custom-made flange of the main vacuum chamber. The custom-made flange, to which the compression springs and bellow are attached, is mounted with heavy brackets directly to the optical table as well as to the vacuum chamber. These heavy brackets ensure a direct and mechanical rigid connection to the optical table to ensure the whole mass of the table can be effectively utilized for the vibrational damping.

The thermal connection is achieved by use of flexible thermal links. A first link is present directly underneath the cryocooler coldhead to connect to a copper rod to ensure a proper thermal link to the main chamber, where it is connected to the primary shield by a second flexible thermal link. This copper rod is mounted inside an aluminum tube, providing a low-emissivity environment. The rod is strongly mounted to this aluminium tube, but allows free movement by the expected thermal contraction by PEEK sliders at the coldhead side, while keeping positional reference at the setup side.

The whole cryogenic assembly is within a shared vacuum of low 10^{-7} mbar pressure for thermal insulation, which is separate from the vacuum inside the cavity itself.

Direct temperature control of the cavity resonator itself is not possible if high-frequency stability at drift rates well below a kHz/s is desired, as typically thermal control and resolution is limited at the mK level. Therefore, we perform temperature control at the thermal connection point from the coldhead to the primary shield (Fig. 3.10), which is stabilized at mK level using a cryogenic PID controller (Cryocon 24c). This benefits from the thermal low-pass characteristics of the heat capacity of the primary shield with the limited thermal conductance to the cavity. FEM simulations in Comsol Multiphysics show that dampening is achieved to ensure stability well below 100 Hz/s drift rate. However, the effect of thermal drift of the outer environment such as the laboratory is not included in this simulation and could influence the thermal stability long-term.

3.8. Cryocooler assembly, vibration isolation and temperature control

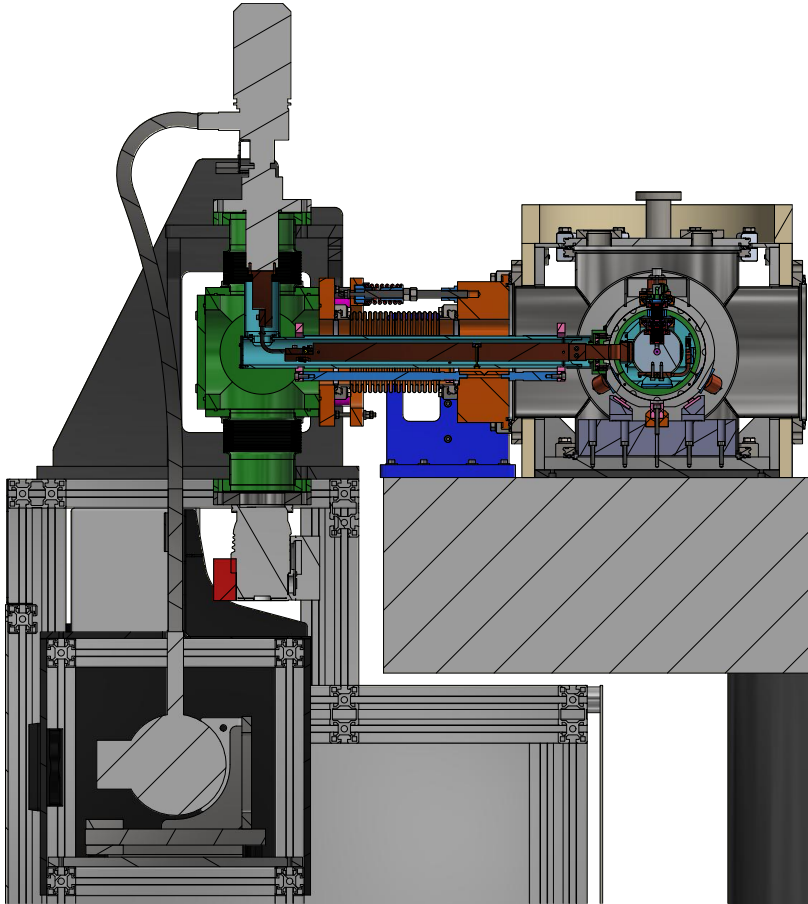


Figure 3.13: Technical illustration of a midplane cutthrough of the complete cavity setup including the cryocooler. Visible is the complete vibration isolation of the cryo-cooler from the optical table and setup. The first vibration isolation stage (green) consists of two opposing balanced bellows. The second vibration isolation stage (orange) is a combination of a flexible bellow, compression springs, and sorbothane dampeners (magenta) and is rigidly mounted to the optical table through a heavy bracket (blue). Both stages combined provides full flexibility and isolation in all degrees of freedom. The cryocooler motor is situated again in a separate frame detached from the cryo-cooler coldhead frame. The coldhead is connected to a copper conductive rod through a flexible copper strap. This long copper rod is housed inside a radiation shield (light-blue) which are all referenced and mounted with respect to the optical table side through a supporting frame (blue) and PEEK supports (pink).

3.9 Cavity operation and performance

3.9.1 Cryogenic performance

The complete mass of the cryogenic assembly is around 10 kg of mostly aluminum components. This results in a cool-down time of roughly three to four days, depending on the required level of thermalization and desired operating temperature. At maximum cooling power of the cryo-cooler the cavity can reach a lower limit of 55 K. However, a slow increase in temperature is observed over time in the course of weeks. It is suspected that water outgassing and permeation through the rubber sealings of the vacuum chamber slowly freeze down on the cold-shields, which is known to have a high emissivity already at monolayer levels [109]. However, when operating at an elevated temperature of around 70 K, the cooling capacity of the cryo-cooler is more than sufficient to maintain continuous operation for over a year.

3.9.2 Mirror substrates and coating

For saturation spectroscopy, both the enhancement factor (thus the finesse) and impedance matching must be considered. While an increase in the finesse directly corresponds to an increase in power and signal enhancement, it will also affect the impedance matching when the transmission through the high reflective coating is comparable to the summed roundtrip losses. The impedance matching is highest when the incoupling transmission matches the total roundtrip losses. However, for practical reasons, both mirrors within a linear cavity are often identical and therefore the roundtrip losses are always above the transmission of the incoupling mirror. Therefore, to maintain a reasonable incoupling efficiency it is important to minimize the additional roundtrip losses as much as possible.

When approaching or surpassing reflectivities of 99.999% the dominant loss becomes the scattering loss from the surface roughness of the substrates. This can be minimized by requesting super-polished substrates with the lowest surface roughness possible. For the anticipated H₂ experiment at 1190 nm, we requested such super-polished mirrors with a finesse of 250,000 (Layertec). Surprisingly, it was found that the finesse of the cavity even increased upon cooling to 50-70 K to a value of over

300 000 under cryogenic conditions. This led to incoupling efficiencies of up to 60% and provided round-trip powers of up to 10 kW.

Another optimization in mirror substrate selection can be found in choosing a wedged mirror design, where the backside of the mirror has a small angle compared to the mirror face as this can further suppress unwanted parasitic etalons. This is especially important when using measurement techniques such as NICE-OHMS, which are extremely sensitive to such parasitic etalons. However, it should be noted that a wedged design is only viable in a design where the front side of the mirror is used to reference its position, such as in our cavity design. Wedged substrates were incorporated in the H₂ studies.

3.9.3 Linewidth of cavity

The short-term frequency stability determines the instantaneous linewidth of the cavity, which is mainly dictated by vibrations and the electronic noise from the two piezo amplifiers. Unfortunately, no stable external reference was available to externally calibrate the cavity linewidth as this would allow straightforward discrimination between noise from vibrations and the piezo amplifiers. As an alternative solution, a molecular resonance was used to have an effective amplitude-to-frequency discriminator by using NICE-OHMS. For this measurement, we used the direct NICE-OHMS signal without any derivative detection, which results in a dispersive lineshape as shown in Fig. 2.1. As the operation of the piezo amplifier is necessary to tune the cavity to a resonance, discrimination between the two origins of noise is not straightforward. Fortunately, the operating frequency of the cryocooler is 60 Hz, while the dominating noise of the piezo amplifiers is expected at 50 Hz, allowing some level of discrimination.

The operating wavelength was limited in the range of 1140 - 1230 nm as the experiment was set up for measurements of the H₂ quadrupole during this calibration. Also the cavity was cooled down to 73 K, which limits the available benchmark molecules. Methane was the only viable candidate, of which we selected the strongest reachable transition for this calibration. Unfortunately, this range was outside the limit of the frequency comb, so no comb-calibrated spectrum of this specific transition is available. However, the frequency to signal amplitude slope was calibrated at 15 MHz/V by using the known response of the piezo.

3. VIBRATION INSENSITIVE CRYOGENIC CAVITY DESIGN FOR CAVITY-ENHANCED SATURATION SPECTROSCOPY

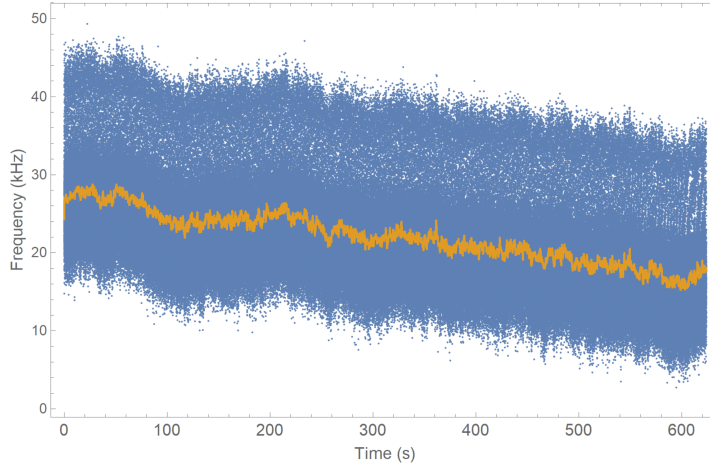


Figure 3.14: Determined frequency noise near the center of a sub-Doppler methane transition using the direct NICE-OHMS signal as an amplitude-to-frequency discriminator. The blue curve represents the raw data with a sampling rate of 900 Hz. The orange curve has a 1 Hz digital low-pass filter applied to the data.

For the linewidth measurement, the system was in a thermalized state and the piezo was tuned on the center of the methane resonance. The signal resulting from the free-running system was recorded for a period of 10 minutes with a sampling rate of 900 Hz to obtain sufficient data to determine the frequency noise and acquire a measure of the drift rate at the timescale of a few minutes (Fig. 3.14). From this time trace it is visible that the average drift during the 10 minute measurement was around 20 Hz/s. Notable is the noiseband of around 30 kHz peak-to-peak. The noise spectral density clearly shows the presence of 50 Hz noise and harmonics, which are probably due to insufficient low-pass filtering of the high-voltage piezo amplifier.

The recent rearrangement of moving both the 395 Hz dither frequency and frequency locking to the frequency comb to the single-stack piezo through the low-noise low-voltage amplifier will allow strong low-pass filtering of the high-voltage amplifier for future measurements. However, no 60 Hz vibrations are observable above the noise-floor within the spectrum. Also, no change to the noise spectral density occurred when the cryo-cooler was briefly switched off, proving that the vibration isolation worked sufficiently.

Applying a low-pass filter to the data to remove the suspected noise from

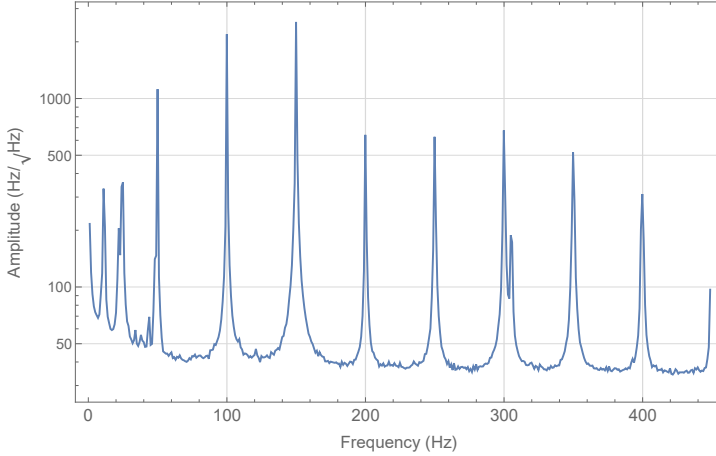


Figure 3.15: Frequency noise spectral density curve of the direct NICE-OHMS signal when tuned to the center of a calibrated Lamb dip of a transition measured in methane at 73 K.

the piezo amplifier results in a noise band of around 1 kHz in width, but this is limited by the amplitude noise of detection of the system and limits a better determination for now. Thus apart from the noticeable ripple and noise from the piezo amplifiers, the linewidth of the cavity itself is expected to be well below 1 kHz.

3.9.4 Frequency stability

The long-term frequency stability of the cavity under cryogenic condition (73 K) was determined by measuring the beat note frequency with the frequency comb. For this measurement, the cavity was first thermalized sufficiently over a day to avoid any remaining observable thermal drift on the system. After this warm-up period, the free-running cavity was logged over 17 hours total to observe the remaining drift rate during this time (Fig. 3.16). The counter was configured with a 1 second gate time, which averages any short-term noise of the cavity. However, the trend is still clearly observable where the maximum drift rate is determined at 33 Hz/s. The observed noiseband is solely determined by the frequency comb, which is known to have a short-term stability of around 10 - 20 kHz at second timescale. This clearly shows that the scanning resolution of the system is currently limited by the short-term stability

3. VIBRATION INSENSITIVE CRYOGENIC CAVITY DESIGN FOR CAVITY-ENHANCED SATURATION SPECTROSCOPY

of the frequency comb laser.

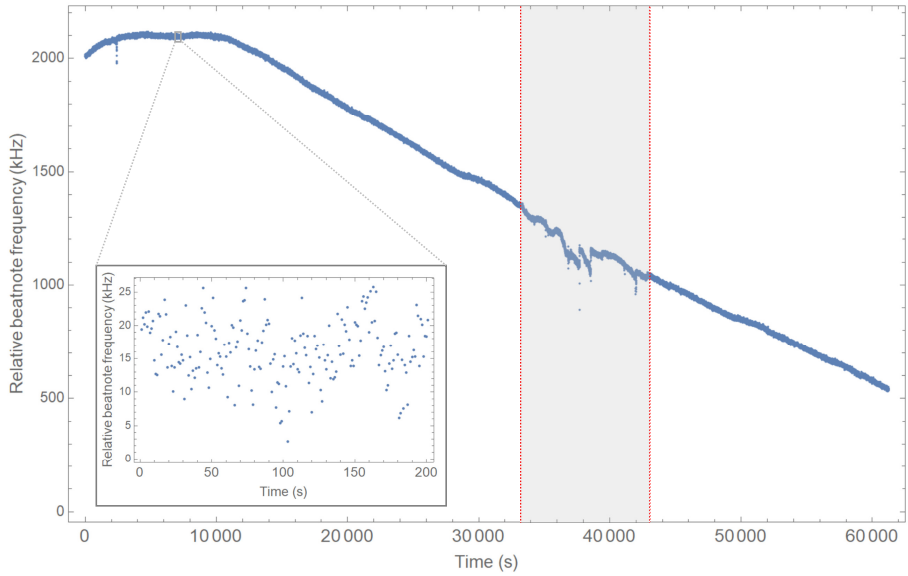


Figure 3.16: Measured drift rate of the free running cavity with respect to the stabilized frequency comb. The beatnote was measured by using a counter with a 1 second gate time. The grey marked area is a period when the frequency comb momentarily had a degraded output spectrum, resulting in lost counts. The inset shows the short-term instability of the comb of roughly 15 kHz peak-to-peak at 1 second of averaging.

Sub-Doppler frequency metrology in HD for test of fundamental physics

Abstract

Weak transitions in the (2,0) overtone band of the HD molecule at $\lambda = 1.38 \mu\text{m}$ were measured in saturated absorption using the technique of noise-immune cavity-enhanced optical heterodyne molecular spectroscopy. Narrow Doppler-free lines were interrogated with a spectroscopy laser locked to a frequency comb laser referenced to an atomic clock to yield transition frequencies [R(1) = 217 105 181 895 (20) kHz; R(2) = 219 042 856 621 (28) kHz; R(3) = 220 704 304 951 (28) kHz] at three orders of magnitude improved accuracy. These benchmark values provide a test of QED in the smallest neutral molecule, and open up an avenue to resolve the proton radius puzzle, as well as constrain putative fifth forces and extra dimensions.

This chapter is based on: *Sub-Doppler frequency metrology in HD for test of fundamental physics*, F.M.J. Cozijn, P. Dupré, E. J. Salumbides, E.J. Salumbides, K. S. E. Eikema and W. Ubachs, *Physical Review Letters* **120**, 153002 (2018)

4.1 Introduction

Molecular hydrogen, the smallest neutral molecule, has evolved into a benchmark quantum test system for fundamental physics now that highly accurate measurements challenge the most accurate theoretical calculations including relativity and quantum electrodynamics (QED) [2, 3], even to high orders in the fine structure constant (up to $m\alpha^6$) [110]. The measurement of the H_2 dissociation energy [111] was a step in a history of mutually stimulating advancement in both theory and experiment witnessing an improvement over seven orders of magnitude since the advent of quantum mechanics [112]. Accurate results on the fundamental vibrational splitting in hydrogen isotopologues [35], with excellent agreement between experiment and theory, have been exploited to put constraints on the strengths of putative fifth forces in nature [7] and on the compactification of extra dimensions [8].

A straightforward strategy to obtain accurate rovibrational level splittings in the hydrogen molecule is to measure weak quadrupole transitions, as was done for H_2 in the first [27] and second overtone band [26, 113], as well as in the fundamental [114] and overtone [32, 115] bands of D_2 . In the heteronuclear isotopologue HD, exhibiting a charge asymmetry and a weak dipole moment [116], a somewhat more intense electric dipole spectrum occurs, first measured by Herzberg [18]. The dipole moment of the (2,0) band is calculated at $20 \mu\text{D}$ [117], in reasonable agreement with experiment [30, 118]. Accurate Doppler-broadened spectral lines in the HD (2,0) band were reported using sensitive cavity ring down techniques [30]. These lines exhibit a width in excess of 1 GHz at room temperature, which challenges the determination of centre frequencies in view of various speed-dependent collisional broadening and shifting phenomena [119]. Careful line shape analysis has led to accuracies of ~ 30 MHz, in accordance with the *ab initio* calculated values [120].

4.2 Experiment

Here we report on the implementation of an absorption technique that combines the advantages of frequency modulation spectroscopy for noise reduction and cavity-enhanced spectroscopy for increasing the interaction length between the light beam and the sample. This extremely sen-

4. SUB-DOPPLER FREQUENCY METROLOGY IN HD FOR TEST OF FUNDAMENTAL PHYSICS

laser, and transfers the absolute accuracy of the frequency standard. The setup provides an intracavity power in the order of 100 W that is sufficient for saturating HD transitions, while the equivalent absorption path length amounts to ~ 40 km. The cavity itself is enclosed within a vacuum chamber, which can be pumped and filled with the HD gas sample, that is inserted through a liquid-nitrogen cooled trap for purification.

The laser source (ECDL, Toptica DL Pro) operating around $1.38 \mu\text{m}$ is mode-matched and phase-locked to the optical cavity. The laser beam is fiber coupled and split, with one part for the frequency calibration and metrology, while the main part is phase-modulated through a fiber-coupled EOM (Jenoptik PM1310), allowing for the simultaneous modulation of two frequencies $f_{\text{PDH}} \sim 20$ MHz and $f_{\text{FSR}} \sim 310$ MHz. The beam reflected from the cavity is collected onto an amplified photoreceiver, the signal of which is divided for locking both the laser frequency f_{opt} via the Pound-Drever-Hall (PDH) scheme [123] and the cavity free spectral range frequency f_{FSR} with the DeVoe-Brewer scheme [80]. The beam transmitted through the cavity is collected with another high-speed photoreceiver, with the amplified signal demodulated at f_{FSR} in a double-balanced mixer. The resulting dispersive NICE-OHMS signal is sent to a lock-in amplifier to extract the $1f$ signal component at the dither frequency $f_{\text{dith}} \sim 430$ Hz with a peak-to-peak amplitude of 80 kHz. The noise equivalent absorption for the setup is estimated to be $1 \times 10^{-12}/(\text{cm}\sqrt{\text{Hz}})$.

The long term frequency stability and accuracy of the system is obtained by beating the spectroscopy laser with a frequency comb (Menlo Systems FC1500-250-WG) stabilized to a Cs clock frequency standard (Microsemi CSIII Model 4301B). The acquired beatnote frequency f_{beat} is measured by an RF counter, and it is used to generate the steering signal for locking the cavity length, thereby tuning the laser frequency f_{opt} , which is determined via:

$$f_{\text{opt}} = f_{\text{ceo}} + n \times f_{\text{rep}} + f_{\text{beat}}, \quad (4.1)$$

where $f_{\text{ceo}} = 20$ MHz is the carrier-envelope frequency offset of the frequency comb laser, $f_{\text{rep}} \sim 250$ MHz is its repetition rate, and $n \sim 8.7 \times 10^5$ is the mode number. The absolute frequency of f_{opt} is determined with an accuracy better than 1 kHz.

4.3 Results and discussion

4.3.1 Measurements of the R(1), R(2), and R(3) lines

The R(1) transition was recorded at different pressures (see Fig. 4.2), where each curve is an average of 4 to 7 scans. A typical scan takes about 12 minutes, with frequency intervals of 12.5 kHz, and with each data point averaged over 6 seconds. Fig. 4.3 displays weaker resonances, where the R(2) spectrum is an average of 12 scans and that of R(3) an average of 5 scans.

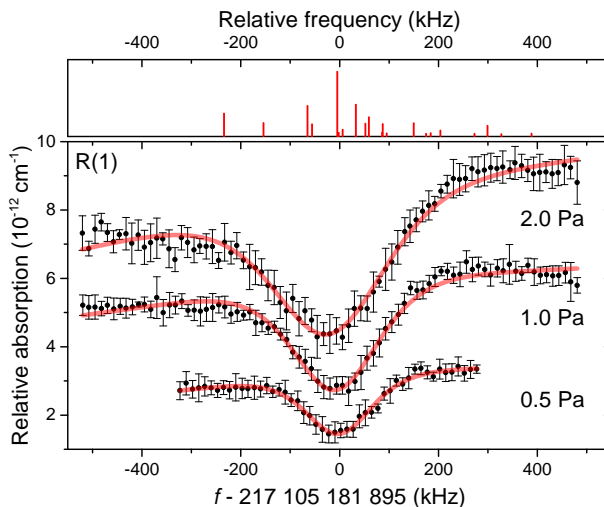


Figure 4.2: Recordings of the HD (2,0) R(1) line for three different pressure conditions averaging 5 scans for 2.0 Pa, 7 scans for 1.0 Pa, and 4 scans for 0.5 Pa. The solid (red) lines are fits using a line shape function based on a derivative of dispersion [43] while allowing for a baseline slope. The curves have been shifted in the vertical direction for clarity. In the upper panel a stick spectrum of the hyperfine structure of this transition is plotted, where the 0-value represents the center-of-gravity.

The assessment of systematic effects was performed primarily on the R(1) transition, where the signal-to-noise ratio is the highest. The R(1) transition frequency was measured at different pressures in the range 0.5 – 5.0 Pa (some shown in Fig. 4.2) displaying widths in the range 150 – 400 kHz (see Fig. 4.4(b)). This allowed the determination of a pressure-dependent shift coefficient at $-9(3)$ kHz/Pa (see Fig. 4.4(a)) and for extrapolation to a zero-pressure transition frequency for R(1). This collisional shift coefficient is an order-of-magnitude larger (but with

4. SUB-DOPPLER FREQUENCY METROLOGY IN HD FOR TEST OF FUNDAMENTAL PHYSICS

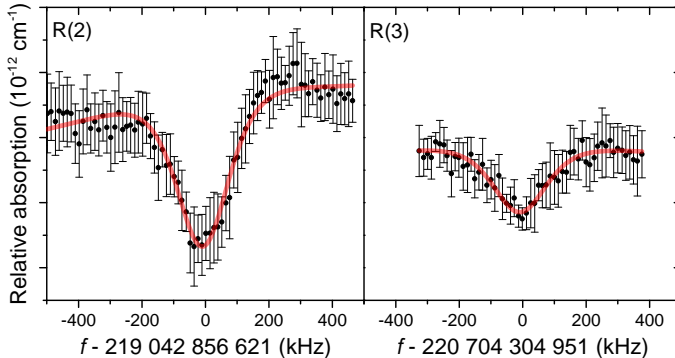


Figure 4.3: Saturation spectra of the R(2) and R(3) transitions of the HD (2,0) overtone band at 1 Pa pressure. [R(2): 12-scan average; R(3): 5-scan average]

similar sign) compared with coefficients for H_2 obtained from studies (e.g. [26]) involving pressures higher than kPa. For R(2) and R(3) transitions measured at 1 Pa, a pressure shift correction of -9 kHz was applied. This seems appropriate in view of the study on H_2 [113] and D_2 [32], where it was shown that the collisional shift parameters only slightly depend on rotational quantum number.

As seen in Fig. 4.2, there is an increase in line shape asymmetry with increasing pressure to which several effects, associated with line broadening can contribute. This asymmetry ultimately limits the present determination of the transition center to an accuracy of $\sim 1/5$ of the observed resonance width. We adopt a phenomenological approach to assess line shape profiles by Gaussian and Lorentzian functions, and a function based on a derivative of dispersion [43] (plotted in Figs. 4.2 and 4.3), as well as linear baseline fits. The baseline variation from scan-to-scan can be attributed to residual amplitude modulation. For the R(1) line, all fits converge to a transition center within 15 kHz from each other, while a convergence to 20 kHz is found for the weaker transitions.

4.3.2 Systematic effects

Saturation spectroscopy in a cavity leads to a photon recoil doublet that is symmetric to the recoil-free transition center [73]. For the HD (2,0) transitions at $1.38 \mu\text{m}$, the recoil shift is 34 kHz, resulting in a doublet splitting of 68 kHz but not producing a systematic shift. At half the

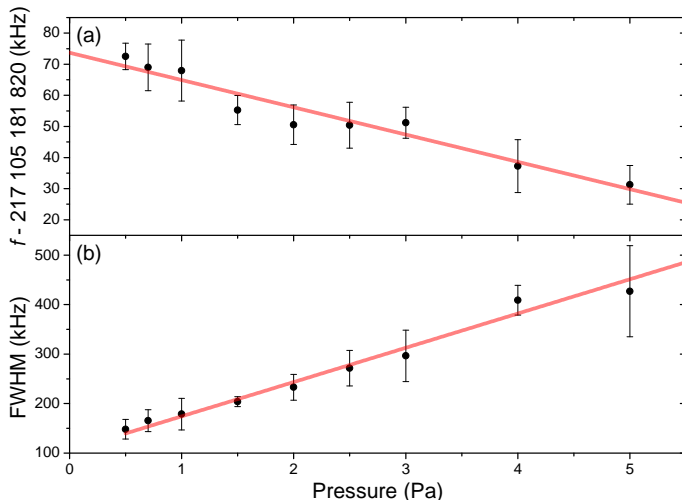


Figure 4.4: Pressure-dependent frequency shift (a) and broadening (b) of the R(1) transition in the 0.5 to 5 Pa pressure range. Note that for the broadening the apparent width is plotted, measured via $1f$ -modulation of the NICE-OHMS signal (see text).

intracavity laser power, no significant shift of the line center is observed, and we estimate an upper limit of 10 kHz for the power-dependent or ac-Stark shift. The second-order Doppler shift is calculated to be 1 kHz for a most probably velocity of 700 m/s (see below).

The collisional or pressure broadening, plotted in Fig. 4.4(b) for the R(1) line, follows a linear behavior with a slope of 70(7) kHz/Pa. It is remarkable that the linear trend extends even to the lowest pressure of 0.5 Pa at which the width is 150 kHz (FWHM). The linewidth of 150 kHz and the values presented in Fig. 4.4(b) correspond to widths that are artificially narrowed by the 430 Hz frequency modulation and the associated detection of the $1f$ derivative on the lock-in detector. Modeling of this phenomenon confirms that the recorded width of 150 kHz translates to a true FWHM linewidth of around 300 kHz for the absorption feature. The recoil doublet splitting of 68 kHz, a Rabi frequency of 20 kHz for the different transitions at peak intensity [124, 125], and the hyperfine sub-structure must contribute to this linewidth. The latter also contributes to the asymmetry (see Fig. 4.2 and text below). An absorption width of 300 kHz is more than three times less than the transit-time rate (FWHM) of 1.3 MHz for HD molecules at room temperature and for the laser beam waist of 450 μm [124, 125]. Similar observations of

4. SUB-DOPPLER FREQUENCY METROLOGY IN HD FOR TEST OF FUNDAMENTAL PHYSICS

Table 4.1: List of corrections Δf and uncertainty estimates σ_f in units of kHz for the transition frequencies.

Contribution	R(1)		R(2), R(3)	
	Δf	σ_f	Δf	σ_f
line fitting	0	15	0	20
pressure shift ¹	0	3	-9	6
2nd-order Doppler	1	1	1	1
ac-Stark shift	0	10	0	10
frequency calibration	0	< 1	0	< 1
subtotal systematic	1	19	-8	23
statistics	0	10	0	15
total	1	20	-8	28

strongly reduced linewidths below the transit-time rate have been shown in methane [126, 127] and acetylene [43], where it was attributed to the dominant contribution of slow-moving molecules in the saturation signal. Even if the entire width of 300 kHz is attributed to transit-time broadening, this would correspond to a most probable speed of 720 m/s. However, in view of the other linewidth contributions discussed above, the most probable velocity may be even lower.

The hyperfine structure of the $v = 0$ levels in HD was investigated by Ramsey and coworkers using molecular beam resonance techniques [128, 129]. Ab initio calculations of hyperfine constants for $v = 2$ and $v = 0$ levels in HD [130], at most differing at 6.5% between vibrational levels, are found to be in good agreement with experiment for $v = 0$ [128]. Based on this the hyperfine sub-structure of the R(1) transition, composed of 21 components, was calculated and represented by a stick spectrum plotted in the upper panel of Fig. 4.2. While the entire hyperfine structure covers a range of 500 kHz, the three most intense hyperfine components fall within a span of 100 kHz around the centre-of-gravity, demonstrating that the observed effective linewidth of 300 kHz is compatible with the hyperfine sub-structure. From this clustering of strongest components around the zero position (see Fig. 4.2) we conclude that the hyperfine structure does not shift the centre frequency of the transition significantly. However, some asymmetry of the line shape, and possibly the back-ground slope, might be due to the unresolved hyperfine structure [131].

¹R(1) has been extrapolated to zero pressure, while for R(2) and R(3) a correction is applied based on pressure-shift coefficient of R(1).

Table 4.2: Comparison of R-branch transition frequencies in the HD (2,0) band obtained from the present study with previous experimental determination Δ_{exp} [30], and with most accurate *ab initio* calculations Δ_{calc} [120]. Values are given in MHz with uncertainties in units of the last digit indicated in between parentheses. See text for a discussion of the theoretical uncertainty.

Line	Study	Ref.	Δ_{exp}	Theory	Δ_{calc}
R(1)	217 105 181.895 (20)	217 105 192 (30)	-10	217 105 180	2
R(2)	219 042 856.621 (28)	219 042 877 (30)	-20	219 042 856	1
R(3)	220 704 304.951 (28)	220 704 321 (30)	-16	220 704 303	2

Table 4.1 lists the error budget of the present study. The statistics entry demonstrates the reproducibility of measurements performed on different days, in some cases after realignment, with the best statistics at 10 kHz obtained for R(1). We estimate a total uncertainty, including systematics, of $\sigma_f = 20$ kHz for the R(1) transition frequency, and $\sigma_f = 28$ kHz for the R(2) and R(3) resonances. Resulting transition frequencies of the R(1), R(2), and R(3) lines are listed in Table 4.2. These values are compared to results of the previous experimental determination by Kassi and Campargue [30] obtained under Doppler-broadened conditions, showing good agreement, with the present results representing a three order of magnitude improvement in accuracy. Theoretical level energy calculations by Pachucki and Komasa [120] were claimed to be accurate to 30 MHz, but values were provided to 3 MHz (10^{-4} cm $^{-1}$) accuracy. Since we compare with the energy splittings between $v = 0$ and $v = 2$, the theoretical transition frequencies in Table 4.2 should be more accurate because of cancellations in various energy contributions. This assessment of the calculation uncertainty is supported by the excellent agreement between our measurements and the theoretical values that is better than 2 MHz.

4.4 Conclusion

The 30-kHz absolute accuracy (10^{-10} relative accuracy) achieved in this study constitutes a thousand-fold improvement over previous work and demonstrates the first sub-Doppler determination of pure ground state transitions in HD, and in fact in any molecular hydrogen isotopologue. The experimental results challenge current investigations in first prin-

4. SUB-DOPPLER FREQUENCY METROLOGY IN HD FOR TEST OF FUNDAMENTAL PHYSICS

ciples relativistic and QED calculations of the benchmark hydrogen molecules [3, 110, 120, 132]. When such calculations reach the same accuracy level as the experiment there is a potential to constrain theories of physics beyond the Standard Model, as was shown previously [7, 8]. The finite size of the proton contributes ~ 300 kHz to the H_2 (3,0) overtone transition [133] and a similar contribution is expected for the HD transitions investigated here. If theory and experiment reach the kHz accuracy level, this will allow for a determination of the proton size to 1% accuracy. Along with complementary investigations in the electronic [134] and muonic hydrogen atoms [135], neutral and ionic molecular hydrogen [136], the HD overtone determinations may contribute towards the resolution of the conundrum known as the proton-size puzzle.

Note added in revision. After submission of this manuscript we were informed about the outcome of a measurement of the HD R(1) line by Lamb-dip cavity ring down spectroscopy by the Hefei group [50], deviating by 900 kHz from our result. In an attempt to find the origin of this discrepancy, both groups measured a stronger R(4) line in C_2H_2 , yielding 217 043 458 139 (6) kHz at Amsterdam and 217 043 458 146 (8) kHz at Hefei. This agreement demonstrates that the discrepancy is not due to differences between spectroscopic techniques, nor in metrology issues like locking of lasers or beat-note measurements. In our laboratory we found no difference, when the C_2H_2 line was measured with and without the option of low-frequency modulation and lock-in detection, thus demonstrating that this mode of operation has no effect on the line center frequency. In addition, the measurement of the HD R(1) transition with linear and with circular polarization in the cavity, resulted in the same transition frequency, proving that optical pumping does not play a role.

The authors wish to thank Prof. J. Gauss (Mainz) for a calculation of hyperfine constants in HD $v = 0$ and $v = 2$ levels. PD is supported by the CNRS. WU acknowledges the European Research Council for an ERC-Advanced grant under the European Union's Horizon 2020 research and innovation programme (grant agreement No 670168).

Rotational level spacings in HD from vibrational saturation spectroscopy

Abstract

The R(1), R(3) and P(3) ro-vibrational transitions in the (2-0) overtone band of the HD molecule are measured in Doppler-free saturation using the technique of NICE-OHMS spectroscopy. For the P(3) line, hitherto not observed in saturation, we report a frequency of 203 821 936 805 (60) kHz. The dispersive line shapes observed in the three spectra show strong correlations, allowing for extraction of accurate information on rotational level spacings. This leads to level spacings of $\Delta_{(J=3)-(J=1)} = 13\,283\,245\,098$ (30) kHz in the $v = 0$ ground state, and $\Delta_{(J=4)-(J=2)} = 16\,882\,368\,179$ (20) kHz in the $v = 2$ excited vibration in HD. These results show that experimental values for the rotational spacings are consistently larger than those obtained with advanced ab initio theoretical calculations at 1.5σ , where the uncertainty is determined by theory. The same holds for the vibrational transitions where systematic deviations of 1.7 - 1.9σ are consistently found for the five lines accurately measured in the (2-0) band.

This chapter is based on: *Rotational level spacings in HD from vibrational saturation spectroscopy*, F.M.J. Cozijn, M.L. Diouf, V. Hermann, E.J. Salumbides, M. Schlösser and W. Ubachs, *Phys. Rev. A* **105**, 062823 (2022)

5.1 Introduction

The spectroscopic investigation of the hydrogen molecule and its isotopologues has played a crucial role in the advancement of quantum mechanics in the molecular domain. The HD isotopologue, observed via its vacuum ultraviolet spectrum immediately after its production and purification [16, 137], undergoes breaking of inversion symmetry, also referred to as $g - u$ symmetry breaking, giving rise to spectroscopic phenomena that are not observed in the homo-nuclear species H_2 and D_2 [138]. One of the special features is the occurrence of a dipole-allowed absorption spectrum in HD in connection the small dipole moment arising from a charge asymmetry in the molecule. Wick was the first to calculate the intensity of this dipole-allowed vibrational spectrum [139] and Herzberg first observed overtone lines combining high-pressure cells with multi-pass absorption [18]. The vibrational spectra of the fundamental [140] and overtone bands [21] were later investigated in more detail and at higher accuracy. In the past decade cavity-enhanced techniques in combination with frequency-comb calibration were employed to investigate the spectrum of the (2-0) band of HD [30]. For a literature compilation of the vibrational spectra of HD we refer to Ref. [141]. The pure rotational spectroscopy of HD, also connected to the dipole moment, was first probed by Treffer and Gush [142], while later more precise spectroscopic measurements were performed [23, 24, 143, 144]. Recently, saturation spectroscopy of R-lines in the (2-0) overtone band was demonstrated [50, 145], to yield linewidths much narrower than in the Doppler-broadened spectroscopies performed previously. These studies led to accuracies at the 20 kHz level, but the modeling of observed lineshapes appeared to be a limiting factor. In the Amsterdam laboratory subsequent measurements with the NICE-OHMS (Noise-Immune Cavity-Enhanced Optical-Heterodyne Molecular Spectroscopy) technique were carried out and the dispersive-like line shape was interpreted in terms of an Optical Bloch equation (OBE) model including underlying hyperfine structure and crossover resonances in the saturation spectrum [51, 146]. The Hefei group extended their studies on the observation of a dispersive line shape, which was interpreted as a Fano line shape [52]. The uncertainties associated with the observed line-shape remain to be a dominating factor and hinder full exploitation of the extreme resolution of the saturation technique, and the determination of transition frequencies at the highest accuracy. The molecular-

beam double-resonance study of the R(0) line of the (1-0) fundamental of HD by Fast and Meek [36] does not suffer from this short-coming, yielding a vibrational splitting in HD at the level of 13 kHz, the most accurate to date. Vibrational splittings in the (1-0) fundamental have also been determined via laser-precision studies in molecular beams and the measurement of combination differences in Doppler-free electronic spectra [147]. The Caserta group applied cavity-enhanced methods for linear absorption spectroscopy of the R(1) line in (2-0). Even though the line is of GHz width an accuracy of 76 kHz is obtained through advanced modeling of the Doppler-broadened line shape [148, 149].

The goals of precision spectroscopy on the hydrogen isotopologues have surpassed the targets of molecular physics. These smallest neutral molecular species have become benchmark systems for probing physics beyond the Standard Model [6], searching for fifth forces of various nature [7, 150] and for higher dimensions [8]. The searches for new physics depend on the availability of highly accurate ab initio computations of the level structure of the hydrogen molecules. In the past decade the boundaries in this area have been pushed, and currently highly accurate level energies are produced in 4-particle fully variational calculations of the relativistic motion in the molecules, augmented with calculation of quantum-electrodynamic corrections up to level $m\alpha^6$ [5, 151, 152]. The results of the ab initio calculations are available through the H2SPECTRE on-line program [153].

A comparison between the recent accurately measured vibrational transition frequencies with those computed from the H2SPECTRE code reveals a systematic offset of 1 MHz for the (1-0) band and 2 MHz for the (2-0) band. The deviations extend very much beyond the uncertainties established in the experiments, but remain at the level of 1.7σ , when the uncertainty of the calculations is taken into account. In order to investigate the origin of these discrepancies we target measurements, by means of saturation spectroscopy, of combination differences between vibrational lines in the (2-0) band.

5.2 Experiment and results

5.2.1 NICE-OHMS experimental layout

In the experiment, the NICE-OHMS setup at the Amsterdam laboratory is used to perform saturation spectroscopy of the R(1), R(3) and P(3) lines of HD at wavelengths near $1.4\ \mu\text{m}$. Details of the setup were described in previous papers on the spectroscopy of HD [51, 145, 146] and specific settings of the present experiment are similar. A noteworthy detail is that a new diode-laser and high-reflectivity mirrors are used to reach the P(3) wavelength, while the measurements of the R(1) and R(3) lines are performed with existing components. The essentials remain identical with an intracavity circulating power at the central carrier frequency f_c of about 150 W, while the sidebands at $f_c \pm f_m$ are modulated at $f_m = 404\ \text{MHz}$ delivering circulating powers of 2 W. The diode-laser is locked to the high-finesse cavity (150,000) via Pound-Drever-Hall stabilization, where the cavity is locked to a Cs-clock stabilized frequency-comb laser. This locking sequence leads to a line-narrowing of the diode laser to around 20 kHz at second time scale caused by short term vibration-noise and thermal drift of the cavity. Ultimately, the absolute frequency of the complete measurement data averages down to below kHz precision due to long term measurements of over a few hours. This stability allows for effectively averaging over multiple scans to obtain reasonable signal-to-noise levels. Averages of around 60 scans with a total measurement time of over 10 hours were taken to record a spectrum of the weakest P(3) line.

The generic signals produced in direct NICE-OHMS spectroscopy under saturation exhibit a dispersive lineshape, as a result of the sideband frequency-modulation applied [58, 63]. The application of an additional low-frequency dither modulation to the cavity length (at 415 Hz) and demodulation at $1f$ by a lock-in amplifier, in principle results in a line shape taking the form of a derivative of a dispersion-like function. Such symmetric line shapes were indeed detected for saturated lines of C_2H_2 [51] and of H_2O [154] in the same setup. In Fig. 5.1 representative spectra of an HD line, in this case the R(1) line in the (2-0) overtone band, are compared with spectral recordings of a water line. This comparison was performed for both $1f$ and $2f$ demodulation of the modulated signal. Details of the applied modulation scheme has been presented earlier for the $1f$ signal channel [51], but the used lock-in am-

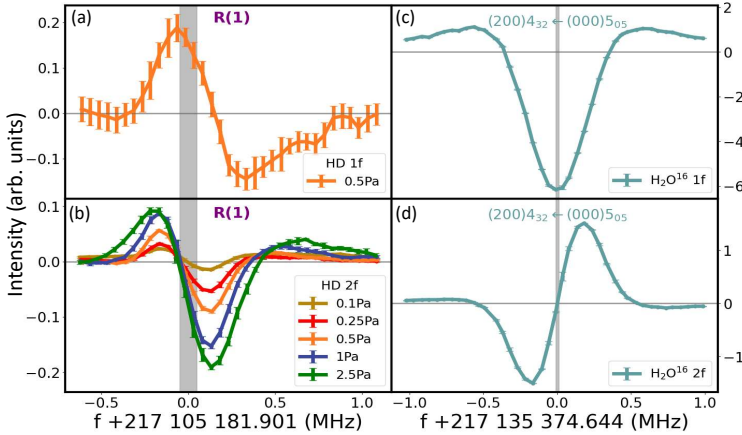


Figure 5.1: Spectral recordings of the R(1) line in the (2-0) overtone band of HD in saturated absorption employing the NICE-OHMS technique. Pressures as indicated in units of Pa. Recordings are performed using (a) $1f$ and (b) $2f$ demodulation. A comparison is made with the recording of a water line, also at (c) $1f$ and (d) $2f$ demodulation settings. Note the strong difference in line shape, where the water line represents the generic NICE-OHMS signal shape. The (gray) vertical bar in (a) and (b) represents the transition frequency of the R(1) line of HD as determined in a previous experimental saturation study via modelling of the spectral line shape based on underlying hyperfine structure and including cross-over resonances [51]. The 0.0 value represents a frequency of 217105181.901 (0.050) MHz for HD and 217135374.644 (0.005) MHz for the H_2O^{16} line.

plifier (Zurich Instruments HF2LI) can be expanded with an additional parallel demodulation channel allowing simultaneous measurements of the $1f$ and $2f$ signal channels. This capability has been used in previous work to detect the $1f$ and $3f$ demodulation channels simultaneously, which resulted in resolving the hyperfine structure of H_2^{17}O [79].

5.2.2 Asymmetric lineshapes of rovibrational lines in HD

These spectra and the comparison between HD and H_2O resonances as measured in saturation demonstrate two important aspects. Firstly, the line shape of the HD resonance in the $1f$ -recording is asymmetric, unlike the shape of the water resonance that follows the expected pattern for NICE-OHMS signals [154]. Similar asymmetric line shapes are observed for the R(3) and P(3) lines, as presented in Fig. 5.2. This phenomenon of

5. ROTATIONAL LEVEL SPACINGS IN HD FROM VIBRATIONAL SATURATION SPECTROSCOPY

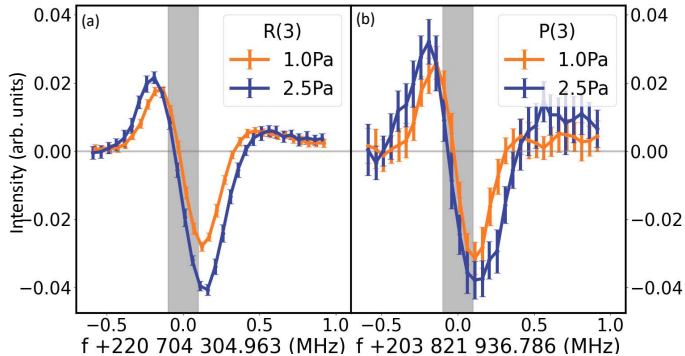


Figure 5.2: Recordings of saturated spectra of the R(3) and P(3) (2-0) overtone lines in HD with NICE-OHMS at $2f$ -demodulation for pressures of 1 Pa and 2.5 Pa. The (gray) bars indicate the estimated spin-averaged transition frequencies and their uncertainties of 100 kHz.

observing unexpected atypical line shapes was discussed in previous papers on the saturation spectroscopy of HD, either using $1f$ -demodulation in NICE-OHMS [51, 145], cavity-ring-down spectroscopy [50], or a variety of cavity-enhanced techniques [52]. Secondly, the experimental data show that the $2f$ -demodulation spectra exhibit a better signal-to-noise ratio (SNR) than the $1f$ -demodulated spectra, while the $1f$ spectra display a much better SNR than the direct NICE-OHMS spectra. For these reasons the comparisons and the detailed analyses of rotational line shifts is based on $2f$ demodulated spectra in the following.

In Fig. 5.1 the transition frequency of the R(1) line and its uncertainty are indicated by the (gray) vertical bar. A result for the R(1) transition frequency was initially reported from a NICE-OHMS study only considering the Lamb-dip feature and fitting its line center; this procedure resulted in a value then considered to be accurate to 20 kHz [145]. However, in a competing study using cavity-ring-down spectroscopy a strongly deviating transition frequency was reported [50]. For this reason a systematic study was performed in which the observed complex line shape, consisting of Lamb-peak and Lamb-dip contributions, was computed via an Optical Bloch Equation (OBE) model from which results a spin-averaged transition frequency of 217 105 181 901 kHz with an uncertainty of 50 kHz [51]. This is the result displayed by the (gray) vertical bar in Fig. 5.1. It shows that the modeled center frequency coincides

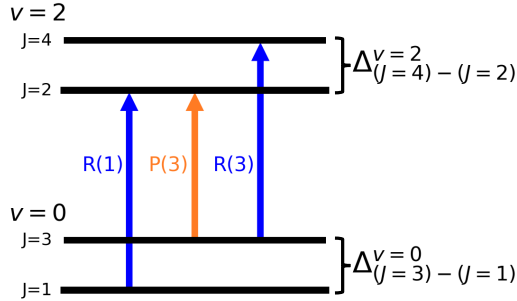


Figure 5.3: Level scheme of HD showing how the three lines R(1), R(3) and P(3) correspond to rotational level spacings in the $v=0$ ground and $v=2$ excited vibrational level.

rather accurately with the Lamb-peak feature in the $1f$ NICE-OHMS signal channel, and with the zero-crossing in the $2f$ signal channel.

For the R(3) line an accurate result was reported in a previous study [145], but this was not substantiated with an explicit OBE-model computation. The P(3) line in the (2-0) overtone band has not been reported before from a saturation experiment. Based on the finding that the line shapes of the R(1), R(3) and P(3) lines exhibit similar line shapes (this paper) it is assumed that the central spin-averaged transition frequencies are all in close proximity of the zero-crossing point in the $2f$ spectral features at the lowest pressures. In view of this assumption the transition frequencies of R(3) and P(3) lines in the observed $2f$ spectra are extracted from the zero-pressure extrapolated $2f$ crossings, displayed in Fig. 5.2, with an uncertainty bar estimated conservatively at 100 kHz. Based on the measurements performed at 1.0 and 2.5 Pa, pressure shifts of -23 kHz/Pa for R(3) and -26 kHz/Pa for P(3) are determined. This leads to values of 220 704 304 963 (100) kHz for R(3) and 203 821 936 786 (100) kHz for P(3).

5.2.3 Extracting rotational level spacings

In Figs. 5.1 and 5.2 it is documented that recorded saturation spectra for the HD resonances deviate from expected and generic line shapes in NICE-OHMS. However, visual inspection indicates that the line shapes

5. ROTATIONAL LEVEL SPACINGS IN HD FROM VIBRATIONAL SATURATION SPECTROSCOPY

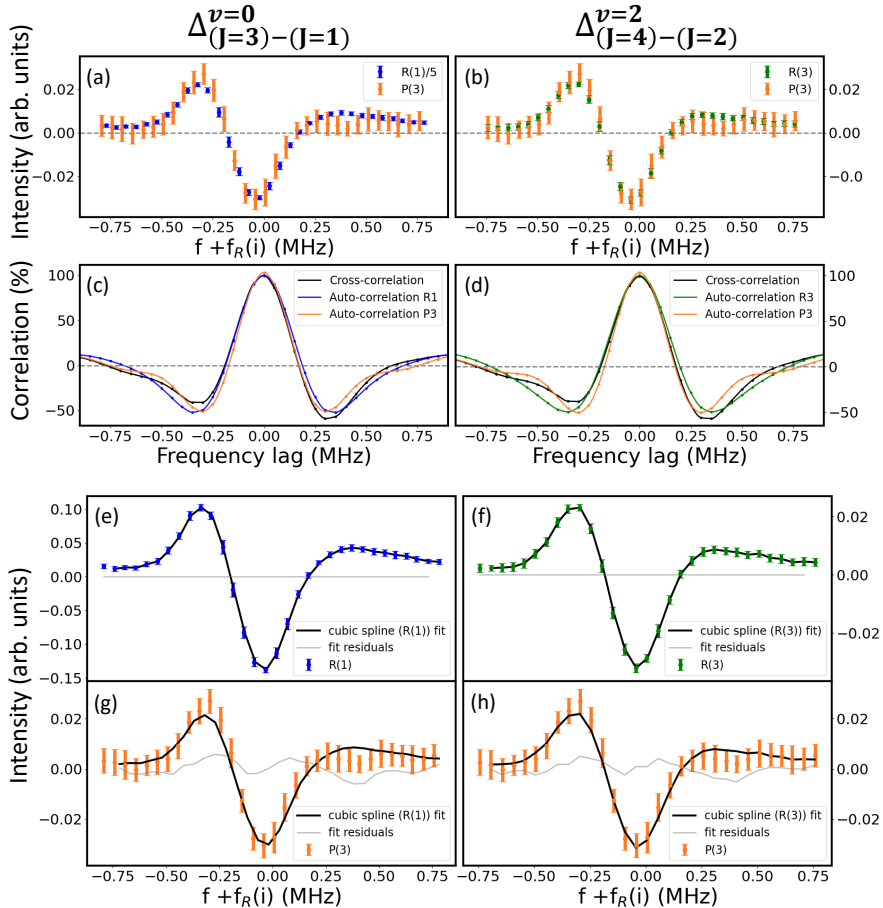


Figure 5.4: Comparison of the $2f$ demodulated saturation spectra for three lines in the (2-0) overtone band of HD, all recorded at a pressure of 1 Pa; (a) Comparison for the pair R(1) and P(3); (b) Comparison for the pair R(3) and P(3). Note that the amplitudes for the corresponding spectra are adapted to match each other. (c) Results of auto-correlation and cross-correlation calculations for the R(1)-P(3) pair and (d) for the R(3)-P(3) pair. In panels (e) and (f) fits are made using a cubic spline interpolation for which residuals are computed and plotted (thin gray line). The resulting cubic spline functional form is then fitted to the line shapes of the P(3) lines in (g) and (h). Residuals of the latter are again plotted in gray.

of the R(1), R(3) and P(3) lines are very similar. This forms the basis for extracting information on rotational level spacings as illustrated in Fig. 5.3.

In Fig. 5.4 recordings of $2f$ -demodulated spectra for the three HD lines are compared. For quantifying the similarities auto-correlation functions are computed as well as cross-correlation functions [155] for the pairs R(1)-P(3) and R(3)-P(3). The resulting cross-correlation curves are found to mimic the auto-correlations in a near-perfect fashion, with a peak overlap of 95%. The cross-correlation computations yield values for the frequency differences Δ between the line pairs R(1)-P(3) and R(3)-P(3) representing rotational line spacings in the $v = 0$ and $v = 2$ levels.

Because the computation of the cross-correlation does not straightforwardly deliver an uncertainty to the values for the line spacing, the $2f$ modulated spectra for the R(1) and R(3) lines were subjected to a standard cubic spline interpolation [156] to produce a functional form closely representing the data. The cubic spline curves and plotted residuals in Fig. 5.4(e) and (f) show that such cubic splines indeed accurately represent the experimental data for the R(1) and R(3) lines. These resulting functional forms, $g(f)$, were then used to fit the third P(3) line in both cases. Aside from adjustment parameters for the amplitude (A) and zero-level (B) a frequency shift term Δ between the R(1)/P(3) and R(3)/P(3) pairs was included, which results in a general fitting function $A \cdot g(f + \Delta) + B$. The latter fits then delivers values for Δ as well as an uncertainty:

$$\begin{aligned}\Delta_{(J=3)-(J=1)}^{v=0} &= 13\,283\,245\,098\,(5)\text{ kHz} \\ \Delta_{(J=4)-(J=2)}^{v=2} &= 16\,882\,368\,179\,(5)\text{ kHz}\end{aligned}$$

in the $v = 0$ ground and $v = 2$ excited vibrations in HD. While the results for Δ are similar as in the computations of the cross-correlations (deviations as small as 2 kHz and 3 kHz found, respectively), the procedure based on cubic-spline fitting delivers a statistical uncertainty as small as 5 kHz for the spacing between the corresponding line pairs.

Systematic effects should be considered that contribute to the error budget for the frequency spacings between lines. The results presented in Fig. 5.4 pertain to measurements at a pressure of 1 Pa. A similar analysis was performed for data sets obtained at 2.5 Pa leading to values for combination differences Δ within 2 kHz. Indeed, the pressure effects

5. ROTATIONAL LEVEL SPACINGS IN HD FROM VIBRATIONAL SATURATION SPECTROSCOPY

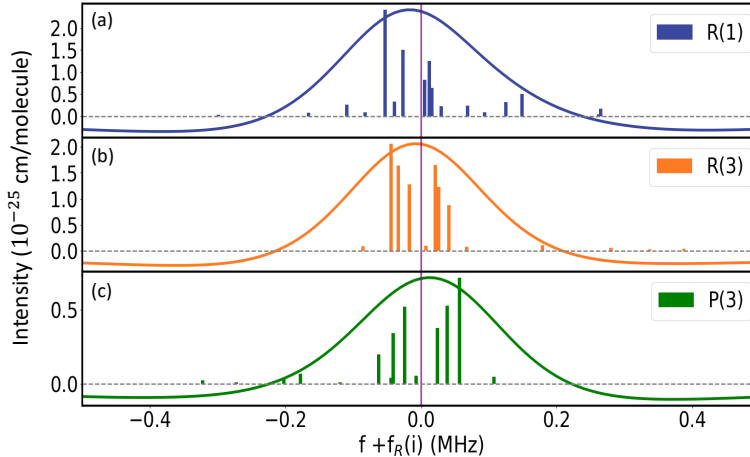


Figure 5.5: Stick spectra of hyperfine components for (a) the R(1) line, (b) the R(3) line; and (c) the P(3) line in the (2-0) overtone band of HD based on the computations of Ref. [157]. These stick spectra were convolved with $1f$ -NICE-OHMS spectral features for each component to yield the curves as plotted.

on level spacings between rotational lines are expected to be small in view of common-mode cancellation of collisional shifts in the combined transitions.

In the previous study [145] it was established that power broadening does play a role in the saturated NICE-OHMS spectroscopy of HD, but power shifts are constrained to < 1 kHz. Also the frequency calibration reaches kHz accuracy.

The observed composite line shapes, consisting of Lamb-peaks and Lamb-dips, were in our previous studies interpreted as resulting from underlying hyperfine structure and cross-over resonances for which a quantitative model was developed based on optical Bloch equations (OBE) [51]. Such an analysis supported by OBE modeling was developed for the R(1) line. In the derivation of the frequency spacings Δ it is assumed that underlying hyperfine structure does not affect the accuracy of this treatment. To assess a possible shift caused by differences in the hyperfine structure of the three lines the underlying hyperfine structure of all three lines is compared, based on the computations of Ref. [157]. In Fig. 5.5 stick spectra of hyperfine components in the spectra of R(1), R(3) and P(3) lines are displayed, convolved with a $1f$ -demodulated NICE-OHMS function (a $1f$ derivative of a dispersive line shape) to produce a final

width commensurate with the width ($\Gamma = 400$ kHz FWHM) obtained in the auto-correlation functions in Fig. 5.4(c,d). For each of these convoluted functions it is computed in how far the line center deviates from the center-of-gravity of the hyperfine structure, *i.e.* the deviation for the spin-averaged frequency. From these calculations it follows that the center frequencies are shifted from the center-of-gravity of the hyperfine structure by -20 kHz, -10 kHz and +10 kHz for the R(1), R(3) and P(3) lines respectively. These shifts are included as systematic uncertainties in the error budget for the pure rotational line spacings. Hence for the P(3)/R(3) line pair a contribution of 20 kHz, and for the P(3)/R(1) pair a contribution of 30 kHz is included as a systematic uncertainty. These estimates on the uncertainty arising from the underlying hyperfine structure make this contribution the dominant one.

Having established values for the combination differences between the pair P(3)/R(1), including uncertainty, this result can be combined with the accurate result for the transition frequency of the R(1) line based on the OBE-model [51], yielding the transition frequency 203 821 936 805 (60) kHz for the P(3) line, deviating some 19 kHz from the estimate based on the $2f$ crossing point. Further combining the pair P(3)/R(3) then delivers a transition frequency for the R(3) line, yielding 220 704 304 984 (65) kHz, deviating 21 kHz from the estimates from the $2f$ crossing point. These frequency separations, obtained via two distinct methods, are in agreement with each other within 0.3σ . The values obtained through the combination differences, considered to be most accurate, are included in Table 5.1.

5.3 Discussion and Conclusion

In the present study the vibrational transitions R(1), R(3) and P(3) in the (2-0) overtone band of HD were measured in saturation via the NICE-OHMS technique. These results are compiled in Table 5.1 including all precision measurements on ro-vibrational and purely rotational transitions hitherto performed. Older data on Doppler-broadened spectroscopy of vibrational overtone transitions [21, 30, 141] are not included. While for the transition frequency of the R(1) line the result based on the systematic study of the line shape, at an accuracy of 50 kHz, was taken [51], results in the present study of R(3) and P(3) are accurate to 65 and 60 kHz, respectively. The experimental results are

5. ROTATIONAL LEVEL SPACINGS IN HD FROM VIBRATIONAL SATURATION SPECTROSCOPY

Table 5.1: Comparison between experimental data on purely rotational and ro-vibrational data on transitions frequencies for HD with results of computed results using H2SPECTRE [153]. All frequencies given in MHz. Differences are presented in terms of MHz and in terms of the combined standard deviation (σ) of experiment and theory. For the entries assigned with "T" the deviations are entirely determined by the theoretical values from H2SPECTRE.

Band	Line	Exp. (MHz)	Ref.	H2SPECTRE (MHz)	Diff. (MHz)	Diff. (σ)	
(0-0)	R(0)	2 674 986.66 (0.15)	[23]	2 674 986.071 (0.022)	0.59 (0.15)	3.9	
		2 674 986.094 (0.025)	[144]	2 674 986.071 (0.022)	0.023 (0.033)	0.7	(T)
	R(1)	5 331 560.6 (4.8)	[24]	5 331 547.053 (0.045)	13.5 (4.8)	2.8	
	R(2)	7 951 729.9 (5.1)	[24]	7 951 697.887 (0.066)	32 (5)	6.4	
	R(3)	10 518 306.8 (3.6)	[24]	10 518 308.641 (0.087)	-1.8 (3.6)	-0.5	
	R(6)	17 745 695.9 (9.0)	[143]	17 745 686.540 (0.140)	3.8 (6.6)	1.0	
(1-0)	S(1) ^a	13 283 245.098 (0.030)	Present	13 283 244.944 (0.110)	0.15 (0.11)	1.4	T
(1-0)	Q(0) ^a	108 889 433.0 (6.6)	[147]	108 889 429.2 (0.5)	3.8 (6.6)	0.6	
	R(0)	111 448 815.477 (0.013)	[36]	111 448 814.5 (0.6)	1.0 (0.6)	1.6	T
	Q(1) ^a	108 773 832.4 (6.6)	[147]	108 773 828.4 (0.5)	4.0 (6.6)	0.6	
(2-0)	P(1)	209 784 242.007 (0.020)	[146]	209 784 240.1 (1.0)	1.9 (1.1)	1.7	T
	P(3)	203 821 936.805 (0.060)	Present ^b	203 821 935.0 (1.0)	1.8 (1.0)	1.8	T
	R(1)	217 105 181.901 (0.050)	[51]	217 105 180.0 (1.1)	1.9 (1.1)	1.7	T
		217 105 182.111 (0.240)	[52]	217 105 180.0 (1.1)	2.1 (1.1)	1.9	T
		217 105 181.901 (0.076)	[149]	217 105 180.0 (1.1)	1.9 (1.1)	1.7	T
	R(2)	219 042 856.621 (0.025)	[145] ^c	219 042 854.7 (1.1)	1.9 (1.1)	1.7	T
R(3)		220 704 304.951 (0.028)	[145] ^c	220 704 303.0 (1.1)	1.9 (1.1)	1.7	T
		220 704 304.984 (0.065)	Present ^b	220 704 303.0 (1.1)	1.9 (1.1)	1.7	T
(2-2)	S(2) ^a	16 882 368.179 (0.020)	Present	16 882 367.976 (0.140)	0.20 (0.14)	1.5	T

^aDerived from a spacing between lines, or a combination difference.

^bResults from vibrational transitions in the present study.

^cResults from fitting center frequency of a Lamb-dip without considering the complex line shape.

compared with values obtained via advanced ab initio calculations as in the H2SPECTRE program suite [153]. In this program some level energies and transitions are computed via non-adiabatic perturbation theory (NAPT) [151], while for some specific levels the non-relativistic part is computed via pre-Born-Oppenheimer or 4-particle variational calculations [5, 152]. The theory entries included in Table 5.1 are partly based on the more accurately computed values, although some matrix elements and the Bethe-logarithm were computed on a BO-basis [158]. Inspection of the Table shows that for the vibrational transitions there are a large number of entries marked by 'T', where the experimental values are more accurate than the theoretical ones and where the uncertainty is fully determined by theory. Although the deviations are all in the range 1.6 - 1.9σ , or at 10 ppb, it is remarkable that the offsets are so consistently equal and of the same sign. This may be considered as an indication that the ab initio calculations of H2SPECTRE systematically underestimate the vibrational level spacings in HD. Also in the D₂ molecule a recent study yielded a similar underestimate of the theoretical value for the S(0) (1-0) vibrational ground tone frequency by 1.2σ [37]. Also in that case, with an experimental accuracy of 17 kHz, the uncertainty was fully determined by theory [159].

For the measurements of pure rotational transitions performed so far there is only a single experimental result claiming the same accuracy as that of theory: a measurement of the R(0) line reported in Ref. [144]. For this result the experimental value is again higher by 0.7σ of the combined uncertainties. The present measurements of rotational level spacings, deduced from combination differences of measured transition frequencies, represent equally accurate determinations, with their 20-30 kHz systematic uncertainties.

So when comparing the most accurate experimental data with the most advanced ab initio calculations, including relativistic and QED effects [110, 151, 159] the body of experimental data, both vibrational and rotational, are some 1.5 - 1.9σ larger than theory. This might be viewed as an offset scaling with energy. However, that finding cannot be extrapolated to results on dissociation energies of the H₂ molecule, where the most accurate experimental result [10] is found to be in excellent agreement with theory [5, 152]. A recent experimental value for the dissociation energy of the D₂ species [11] was found to be off from theory [5] by 2 MHz, corresponding to 1.6σ , but here the uncertainty contributions from experiment and theory were the same. As for the case of the dissociation

energy of the HD isotopologue the current experimental value [160] is off from theory [5] by 2.7σ . While this might be viewed as another discrepancy for the HD species, where $g - u$ symmetry-breaking plays a role, it should be considered however, that in this case the uncertainty is fully determined by experiment.

Inspection of results from the H2SPECTRE on-line program [153] reveals that the uncertainties for the rotational splittings on the theoretical side fully depend on the uncertainty in the evaluation of the $E^{(5)}$ leading order QED-term. For the $\Delta_{(J=3)-(J=1)}^{v=0}$ splitting the uncertainty in $E^{(5)}$ amounts to 107 kHz, compared to a full uncertainty over all terms of 110 kHz. For $\Delta_{(J=4)-(J=2)}^{v=2}$ this is 137 kHz out of 140 kHz uncertainty contributed from $E^{(5)}$. These uncertainties in the rotational splittings imply already strong cancellation of common-mode contributions, where the uncertainties in the $E^{(5)}$ -term in the binding energies of HD-levels ($v = 0, J = 1$ and 3) amount to 5.5 MHz [153]. For specific low-lying levels the $E^{(5)}$ contributions to their binding energy are much more accurate, like for the H_2 ($v = 0, J = 0$) ground level where $E^{(5)}$ is accurate to 5 kHz [4], while for HD ($v = 0, J = 0$) the $E^{(5)}$ -term is accurate only to 120 kHz [5]. This reflects the higher level of computation pursued for H_2 , an approach that might resolve the presently found discrepancies between experiment and theory for the HD molecule. In this sense the presently determined splittings in HD form a test bench theory for the further development of theory for the hydrogen molecular species.

The authors thank IHM van Stokkum (VUA) for fruitful discussions on the data analysis. The research was funded via the Access Program of Laserlab-Europe (Grant Numbers 654148 and 871124), a European Union’s Horizon 2020 research and innovation programme. Financial support from the European Research Council (ERC-Advanced Grant No. 670168) and from the Netherlands Organisation for Scientific Research, via the Program “The Mysterious Size of the Proton” is gratefully acknowledged. M. Schlösser wants to thank the Baden-Württemberg Foundation for the generous support of this work within the Elite-Postdoc-Fellowship.

Saturation spectroscopy of R(0), R(2) and P(2) lines in the (2-0) band of HD

Abstract

Lamb-dips of R(0), R(2) and P(2) ro-vibrational transitions in the (2-0) overtone band of the HD molecule are measured at cryogenic temperatures using the technique of NICE-OHMS spectroscopy. Resulting transition frequencies are 214 905 335 240 (100) kHz for R(0), 219 042 856 794 (150) kHz for R(2), and 206 898 802 150 (150) kHz for P(2). Small, but systematic deviations (at 1.7σ level) are found from advanced ab initio calculations, supporting results from previous studies probing other lines in the (2-0) band. From a combination difference between the R(0) and P(2) lines an accurate value for rotational level spacing in the $v = 0$ ground state is determined, of $\Delta_{(J=2)-(J=0)} = 8\,006\,533\,168(26)$ kHz, well in agreement with theory (at 0.6σ). Based on the observation of the dispersive line shape of R(0) the status of proposed models for the elusive line shapes of saturated transitions in HD is discussed.

This chapter is based on: *Saturation spectroscopy of R(0), R(2) and P(2) lines in the (2-0) band of HD*, F.M.J. Cozijn, M.L. Diouf, and W. Ubachs, *Eur. Phys. J. D* **76**, 220 (2022)

6.1 Introduction

Precision spectroscopy of the hydrogen molecule is a favoured avenue for testing molecular quantum electrodynamics and to search for new physics [6]. One of the targets has been the determination of the dissociation energies of various isotopologues, where developments on the experimental side [10, 11, 111] and on the theoretical side [2, 4, 5] have gone hand-in-hand in a mutually stimulating fashion. The theoretical development [151] has led to the public availability of a program suite delivering binding energies of all rovibrational states in all hydrogen isotopologues at high accuracy [153].

The vibrational spectroscopy of HD is another preferred target for precision studies, since the small dipole moment in this heteronuclear species gives stronger absorption strength compared to that in homonuclear species, where only quadrupole transitions are allowed [18]. Cavity-enhanced techniques were employed to perform Doppler-broadened spectroscopies of the (2-0) band at a wavelength of $1.4 \mu\text{m}$ [30, 148]. Progress in precision was achieved, when saturation spectroscopy of R-lines in the (2-0) overtone band was demonstrated [50, 145]. These studies revealed unexpected asymmetric lineshapes for the saturated absorption features that hamper the precision at which transition frequencies can be determined. Thereafter a number of studies were performed on the dispersive-like line shapes for which various interpretations were postulated, ranging from underlying hyperfine structure and cross-over resonances [51, 146] to a Fano line shape resulting from discrete-continuum interaction in the excitation of HD [52]. Effects of the standing waves produced by the strong intracavity laser fields were also considered [53]. The R(0) line in the (2-0) band of HD had been inaccessible from spectroscopic studies since it is overlaid with a strong water vapor absorption line. However, in specially designed cryo-cooled intracavity measurement setups the R(0) could be measured under Doppler-broadened conditions [28, 91]. In the present study a cryogenic approach is combined in a noise-immune-cavity-enhanced optical-heterodyne molecular spectroscopy (NICE-OHMS) experiment in which the R(0) transition is saturated and measured under Doppler-free conditions. From similar measurements on the R(2) and P(2) lines accurate values for rotational level splittings are determined via combination differences. This work follows the method of a previous study that combined precision measurements of R(1), R(3) and P(3) lines [161].

6.2 Experiment

The NICE-OHMS setup at the Amsterdam laboratory is essentially similar to that used in previous experiments on HD [51, 145, 146, 161]. The novelty is that the optical cavity is rebuilt and attached to a cryo-cooler to reach temperatures in the range 50-300 K. Details of the cryo-cooled cavity design and operation will be communicated in a forthcoming paper [162]. For the spectroscopy a diode laser, running at $1.4\ \mu\text{m}$, is used. The laser is locked to the cavity for short-term stability and to a frequency-comb-laser for long-term stability and for setting the absolute frequency scale. By locking the comb to a Cs-clock the accuracy of the absolute frequency averages down to below kHz in long-term measurements. Another improvement is in the use of a free-space electro-optic modulator (EOM) with better transmittivity compared to the previously used fiber EOM, now yielding an intracavity circulating power at the central carrier frequency f_c of 450 W. Sidebands are generated at $f_c \pm f_m$ with $f_m = 404\ \text{MHz}$ for generating the NICE-OHMS signal and at $f_{PDH} = 20\ \text{MHz}$ for the Pound-Drever-Hall cavity lock. In addition slow wavelength dithering of the cavity length is applied at 395 Hz allowing for lock-in detection. Depending on the dither modulation amplitude, this dithering may induce broadening of the observed spectrum. In the present study only $1f$ demodulation is applied. In view of the better vibration isolation of the upgraded cavity and suppression of drifting background signal there is no need to use $2f$ demodulation for further noise removal. For further details we refer to previous reports [51, 145, 146, 161].

6.3 Results

6.3.1 Vibrational transitions

Results of recorded saturated spectra for the R(0) line in the (2-0) band of HD, measured at temperatures of 57 K and 180 K and for pressures in the range of 0.01 - 0.5 Pa, are presented in Fig. 6.1. At these low temperatures water vapor is completely frozen and indeed the strong $(10_1)2_{11}-(000)3_{12}$ water line at 214904335 MHz does not hinder the recording of R(0). The recorded spectra feature a combination of a 'Lamb-peak' at the low frequency side and a Lamb-dip at the high fre-

6. SATURATION SPECTROSCOPY OF R(0), R(2) AND P(2) LINES IN THE (2-0) BAND OF HD

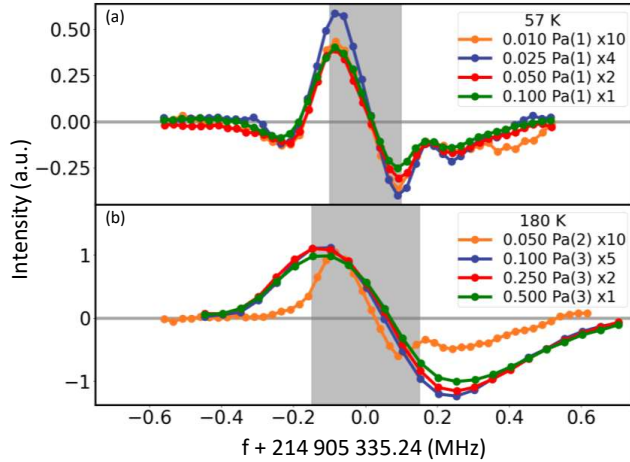


Figure 6.1: Spectrum of the R(0) line in the (2-0) overtone band of HD in saturated absorption employing the NICE-OHMS technique in the cryo-cooled setup using $1f$ demodulation. Spectra were measured at temperatures of 57 K (a) and 180 K (b) for pressures as indicated in the legend. The different indexes represent the broadening due to the dithering effect: (1) 10 kHz, (2) 50 kHz and (3) 200 kHz. The spectra have been scaled to their respective pressures with multiplication factors as indicated. The 0.0 value at the x -axis represents the deduced transition frequency of R(0): 214 905 335.240 (0.100) MHz.

quency side, resulting in a dispersive line shape as discussed before for other saturated lines in the HD (2-0) band [51–53, 161].

Here we note again, as in our previous study [161], that generic signals produced in direct NICE-OHMS spectroscopy exhibit a dispersive lineshape, as a result of the frequency modulation spectroscopy applied [55, 63]. A recording of a spectrum with an additional low-frequency dither modulation to the cavity length, as in the present study, and demodulation at $1f$ by a lock-in amplifier, typically produces a symmetric line shape. This was shown for measurements of Lamb dips in H_2O [154]. Hence, the present $1f$ demodulated spectra may be compared with results from cavity ring-down or cavity-enhanced spectroscopy. The observations displayed in Fig. 6.1 demonstrate that the R(0) line, measured in saturation, produces an intrinsically dispersive line shape, similar to the NICE-OHMS observations of R(1), R(3) and P(3) lines [161] as well as the observations in HD from other cavity-enhanced techniques [52].

The apparent asymmetry and the lack of a fully quantitative model for the observed line shape prohibits the determination of the transition frequency of the rovibrational R(0) line at an accuracy as high as for symmetric water lines [154]. Hence values for the transition frequency and its uncertainty are estimated by considering that the rovibrational frequency is contained in the most pronounced part of the line shape. The region of this estimate is indicated by the (grey) bars in Fig. 6.1. The example of the absorption feature at cryo-temperatures (57 K) gives rise to the narrowest feature, leading to a determination of the transition frequency of R(0) of 214 905 335.240 (0.100) MHz.

The spectra recorded at different pressures provide insight into the collisional shift of the R(0) line. In view of the conservative uncertainty estimate, as indicated by the grey bar, its contribution to the error budget (< 10 kHz) is much smaller than the uncertainty due to the dispersive line shape. Different modulation amplitudes of dithering have been used throughout this study. For the measurements at 57 K the smallest dithering amplitude was applied, giving rise to a broadening of 10 kHz. Larger modulation amplitudes have been used for the spectra acquired at 180 K, resulting in broadening effects of 50 kHz and 200 kHz, respectively. Fig. 6.1 clearly illustrates the effect of dithering amplitude, showing a larger impact on the spectral width than the variation of pressure.

Recordings of $1f$ -demodulated NICE-OHMS spectra of R(2) and P(2) lines in the (2-0) band are displayed in Fig. 6.2. These measurements were performed at a temperature of 180 K. At the 57 K setting the population in the $J = 2$ ground level was too small for obtaining good quality spectra. Again, an estimate of the uncertainty of the P(2) and R(2) vibrational transition frequencies is made commensurate with the grey bar covering the resonance. In these cases, of broader lines, the uncertainty is estimated at 150 kHz.

6.3.2 Rotational level separations

Inspection of Figs. 6.1 and 6.2 reveals that the saturation spectra for the three HD resonances as recorded via $1f$ -demodulated NICE-OHMS exhibit asymmetric line shapes that deviate from expected line shapes in NICE-OHMS. However, the dispersion-like line shapes of the R(0), R(2) and P(2) are rather similar to each other as well as to line profiles of the previously investigated R(1), R(3) and P(3) lines [161]. Again combi-

6. SATURATION SPECTROSCOPY OF R(0), R(2) AND P(2) LINES IN THE (2-0) BAND OF HD

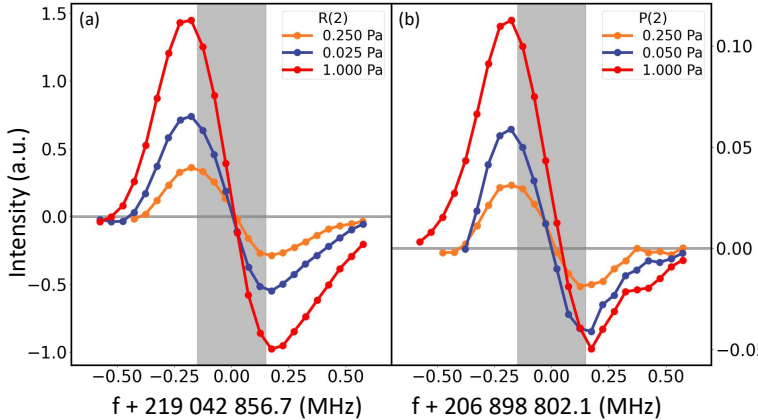


Figure 6.2: Spectra of (a) R(2) and (b) P(2) lines in the (2-0) band of HD in saturated absorption employing the NICE-OHMS technique in the cryo-cooled setup using $1f$ demodulation. Spectra were measured at temperatures of 180 K for pressures as indicated in the legend. The broadening effect induced by the dithering amplitude is estimated at up to 200 kHz.

nation differences will be used to extract information on rotational level spacings as illustrated in Fig. 6.3, in this case the spacings $\Delta_{(J=2)-(J=0)}$ in the ground vibrational $v = 0$ level, and $\Delta_{(J=3)-(J=1)}$ in the $v = 2$ vibrational level.

In Fig. 6.4 spectra of $1f$ -demodulated spectra for the three HD lines, all recorded at 180 K, are compared. The procedure for comparison is similar as previously described [161]. Auto-correlation and cross-correlation functions for the pairs R(0)-P(2) and R(2)-P(2) demonstrate quantitatively the similarity between the spectra, with a peak overlap of 85% and 95% for the cross-correlated pairs, respectively. Fitting of standard cubic spline interpolations is employed to produce a functional form closely representing the line shapes of the strong R(0) and R(2) lines as shown in panels (e) and (f). These resulting functional forms are then used to fit the weak P(2) line in both cases. In this final step a frequency shift term Δ is determined, delivering frequency shifts between the R(0)/P(2) and R(2)/P(2) pairs. This procedure results in combination differences between the line pairs, and therewith rotational level spacings $\Delta_{(J=2)-(J=0)}^{v=0}$ and $\Delta_{(J=3)-(J=1)}^{v=2}$ at a statistical accuracy of 12 kHz and 5 kHz, respectively.

Underlying hyperfine structure of the resonance lines may cause a sys-

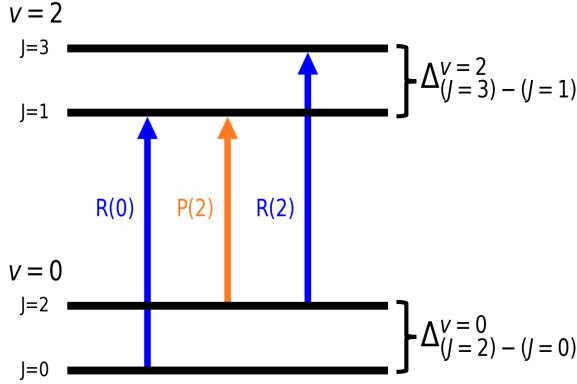


Figure 6.3: Level scheme of HD showing how the three lines R(0), R(2) and P(2) correspond to rotational level spacings in the $v=0$ ground and $v=2$ excited vibrational level.

tematic effect on the determination of the combination differences. The hyperfine structure of all three lines is evaluated based on the computations of Ref. [157]. Computed intensities of individual hyperfine components are convolved with a $1f$ derivative of a dispersive line shape function to produce a width commensurate with the width ($\Gamma = 700$ kHz FWHM) obtained in the spectra observed at 180 K. This allows for a computation of the shift of line center from the center-of-gravity of the hyperfine structure, resulting in shifts of 0 kHz, 0 kHz and +10 kHz for the R(0), R(2) and P(2) lines, respectively. The shifts for the P(2) line is included in the error budget for the pure rotational line spacings.

The shift due to the the pressure has been systematically investigated in Fig. 6.5. Using a linear regression, the pressure free position has been extracted as well as the slopes for the individual rotational level spacings. The pressure shift slopes have been estimated at -18.5 (28) kHz/Pa for the R(0)/P(2) pair and -19.8 (2) kHz for R(2)/P(2) pair, while the extracted uncertainties of 22 kHz and 2 kHz have been included in the error budget.

6. SATURATION SPECTROSCOPY OF R(0), R(2) AND P(2) LINES IN THE (2-0) BAND OF HD

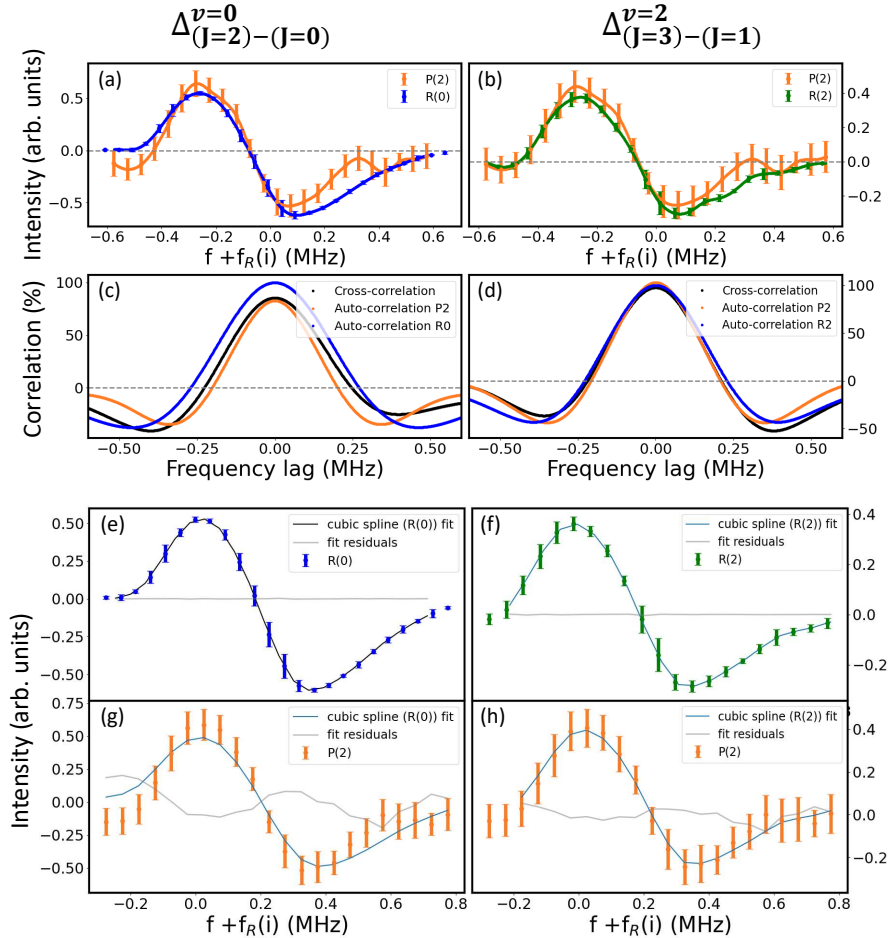


Figure 6.4: Analysis of combination differences from comparison of the saturation spectra for three HD lines in the (2-0) overtone band, all recorded at a pressure of 0.25 Pa, temperature of 180 K, and at $1f$ demodulation of the NICE-OHMS signal. (a) Comparison for the pair R(0) and P(2); (b) Comparison for the pair R(2) and P(2). Note that the amplitudes for the corresponding spectra are adapted to match each other. (c) Results of auto-correlation and cross-correlation calculations for the R(0)-P(2) pair and (d) for the R(2)-P(2) pair. In panels (e) and (f) fits are made using a cubic spline interpolation for which residuals are computed and plotted (thin grey line). The resulting cubic spline functional form is then fitted to the line shapes of the P(2) lines in (g) and (h). Residuals of the latter are again plotted in grey.

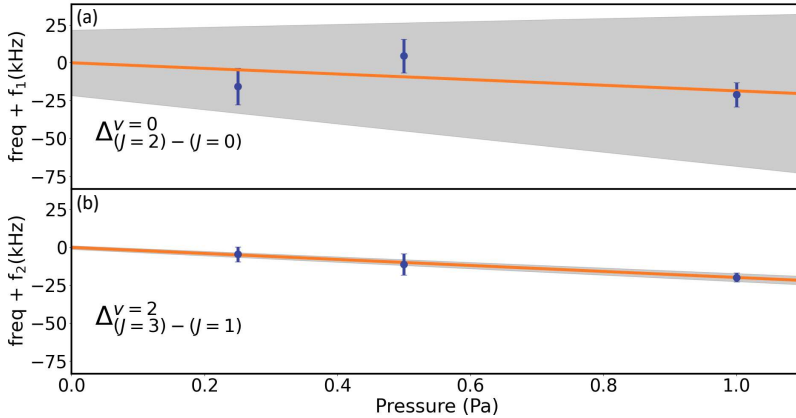


Figure 6.5: Pressure effect on the rotational splitting. (a) Effect on $S(0)$ in the $v = 0$ ground state; (b) $S(1)$ in $v = 2$. The shaded grey areas represent the uncertainties of a linear regression fit used. The extracted slopes represent the pressure coefficients with their respective uncertainties yielding (a) $-18.5 (28)$ kHz/Pa and (b) $-19.8 (2)$ kHz/Pa. The pressure free values have also been extracted with uncertainties of 22 kHz (a) and 2 kHz (b) respectively.

Taking all uncertainty contributions into account values for the rotational level spacings are determined for $\Delta_{(J=2)-(J=0)}^{v=0} = S^0(0) = 8\,006\,533\,168 (26)$ kHz and $\Delta_{(J=3)-(J=1)}^{v=2} = S^2(1) = 12\,144\,054\,660 (20)$ kHz.

6.4 Discussion

6.4.1 Comparison with QED calculations

The present results for the vibrational transition frequencies of the $R(0)$, $R(2)$ and $P(2)$ in the $(2-0)$ overtone band of HD, as obtained via NICE-OHMS saturation spectroscopy, are listed in Table 6.1 with all previously obtained precision measurements for this band. The content of Table 6.1 is limited to experimental values for which the precision exceeds that of quantum electrodynamic (QED) calculations from the H2SPECTRE program (version 7.3) [153] with neglect of older less precise data [161]. The present frequency determinations corroborate the findings discussed in the study on $R(1)$, $R(3)$ and $P(3)$ lines [161], as well as the recent very

6. SATURATION SPECTROSCOPY OF R(0), R(2) AND P(2) LINES IN THE (2-0) BAND OF HD

Table 6.1: Comparison between experimental data, from the present work and literature, and computed results using H2SPECTRE [153] for ro-vibrational transition frequencies in the (2-0) band of HD with results. All frequencies given in MHz. Differences are presented in terms of MHz and in terms of the combined standard deviation (σ) of experiment and theory.

Band	Line	Exp. (MHz)	Ref.	H2SPECTRE (MHz)	Diff. (MHz)	Diff. (σ)
(2-0)	P(1)	209 784 242.007 (0.020)	[146]	209 784 240.1 (1.0)	1.9 (1.1)	1.7
	P(2)	206 898 802.150 (0.150)	Present	206 898 800.2 (1.0)	1.9 (1.1)	1.8
	P(3)	203 821 936.805 (0.060)	[161]	203 821 935.0 (1.0)	1.8 (1.0)	1.8
	R(0)	214 905 335.220 (0.020)	[28]	214 905 333.3 (1.1)	1.9 (1.1)	1.7
	R(1)	214 905 335.240 (0.100)	Present	214 905 333.3 (1.1)	1.9 (1.1)	1.7
		217 105 181.901 (0.050)	[51]	217 105 180.0 (1.1)	1.9 (1.1)	1.7
		217 105 182.111 (0.240)	[52]	217 105 180.0 (1.1)	2.1 (1.1)	1.9
		217 105 181.901 (0.076)	[148]	217 105 180.0 (1.1)	1.9 (1.1)	1.7
	R(2)	217 105 181.934 (0.020)	[28]	217 105 180.0 (1.1)	1.9 (1.1)	1.7
		219 042 856.621 (0.025)	[145] ^a	219 042 854.7 (1.1)	1.9 (1.1)	1.7
		219 042 856.794 (0.150)	Present	219 042 854.7 (1.1)	2.1 (1.1)	1.9
	R(3)	220 704 304.951 (0.028)	[145] ^a	220 704 303.0 (1.1)	1.9 (1.1)	1.7
	220 704 304.984 (0.065)	[161]	220 704 303.0 (1.1)	1.9 (1.1)	1.7	

^aResults from fitting center frequency of a Lamb-dip without considering the complex line shape, leading to an underestimate of the uncertainty.

Table 6.2: Comparison between experimental precision data and computed results using H2SPECTRE [153] for rotational transition frequencies and level splittings in the $v = 0$ ground level of HD. All frequencies given in MHz. Differences are presented in terms of MHz and in terms of the combined standard deviation (σ) of experiment and theory.

Band	Line	Exp. (MHz)	Ref.	H2SPECTRE (MHz)	Diff. (MHz)	Diff. (σ)
(0-0)	R(0)	2 674 986.094 (0.025)	[144]	2 674 986.071 (0.022)	0.023 (0.033)	0.7
	S(0) ^a	8 006 533.168 (0.026)	Present	8 006 533.126 (0.066)	0.042 (0.070)	0.6
	S(1) ^a	13 283 245.098 (0.030)	[161]	13 283 244.944 (0.110)	0.158 (0.114)	1.4
(2-2)	S(1) ^a	12 144 054.660 (0.020)	Present	12 144 054.520 (0.099)	0.140 (0.101)	1.4
	S(2) ^a	16 882 368.179 (0.020)	[161]	16 882 367.976 (0.140)	0.200 (0.141)	1.5

^aDerived from a combination difference.

6. SATURATION SPECTROSCOPY OF R(0), R(2) AND P(2) LINES IN THE (2-0) BAND OF HD

precise measurement of the R(0) transition under Doppler-broadened and cryo-cooled conditions [28]. For the present and all previous precision measurements on lines in the (2-0) band the experimentally determined frequencies are consistently higher than theory by 1.9 ± 0.1 MHz, corresponding to 1.7σ . This further strengthens the indication that the ab initio calculations of H2SPECTRE (version 7.3) systematically underestimate the vibrational frequencies in HD, even though these calculations are only accurate to 1.1 MHz.

The results on pure rotational transitions and the measurements of rotational level splittings are compiled in Table 6.2. Again only the results for which the experimental accuracy exceeds that of the theory are included. There is only a single experimental result for a pure rotational transition, that of the R(0) line [144], performed at a similar accuracy as that of theory. The present measurement of the S(0) level spacing and that of the previous S(1) separation [161] are somewhat more accurate than theory. Focusing on the $v = 0$ ground level of HD there are now three accurate experimental data points for comparison with theory. On average experiment and theory are in agreement within 1σ although the experimental values are consistently at higher frequencies than the theoretical ones. These results provide a challenge for future calculations of HD level energies, beyond the state-of-the-art of H2SPECTRE version 7.3, which is limited by the computation of the $E^{(5)}$ term in the QED expansion [110, 151, 159].

6.4.2 Dispersive lineshape of R(0)

A discussion has arisen in literature on the observed line shapes of vibrational transitions in the (2-0) band of HD as measured in saturation after the first reports in 2018 [50, 145]. The observation of asymmetric line shapes, for which no fully quantitative model is yet formulated, hinders the determination of a very accurate frequency. In principle transition frequencies can be determined to sub-kHz precision in case of unproblematic line shapes, therewith fully exploiting the capabilities of frequency-comb-locked saturation spectroscopy, as was shown for the example of CO₂ [163, 164].

Various models have been proposed for the dispersive nature of the line shapes of saturated lines as observed in HD. The Amsterdam group proposed a model based on the effect of underlying hyperfine structure and the associated cross-over resonances. A computation of the line shape

with optical Bloch equations (OBE) yielded a good representation for the R(1) line [51]. In this approach parameters for collisional deexcitation and coherence dephasing were included in the model by fitting to the observed line shape. This model generally predicts a dispersive-like line shape for all transitions in the (2-0) band of HD except for the cases of the P(1) and R(0) lines, where the level scheme is such that either the hyperfine components in the excited state or in the ground state are very close to degeneracy. Note that for $J = 0$ levels in HD hyperfine doublets are of order 50 Hz [165]. In the case of the P(1) line the OBE-model predicts a pure Lamb peak as was indeed observed in experiment [146]. The OBE-model predicts a symmetric pure Lamb dip for the R(0) resonance. Inspection of Fig. 6.1 reveals that the saturated absorption spectrum of the R(0) line exhibits a dispersion-like line shape, in contradiction with that prediction.

The Hefei group proposed a model identifying the observed profile of the R(1) line as a Fano line shape [52] representative of an interference between a transition to a discrete and a continuum level. The discrete resonance would then be represented by the weak vibrational transition in the (2-0) band, while the continuum would be represented by the Lorentzian tail of the $B^1\Sigma_u^+ - X^1\Sigma_g^+$ electronic band system. This proposal would, however, also predict a similar Fano-type interference for the P(1) line, where it was not observed [146]. In addition, this mechanism should also apply to the case of the measurement of the R(0) line in the (1-0) band measured in a molecular beam [36] as well as in the observations of the R(0) line in the (2-0) band under conditions of cryo-cooling and reduced Doppler width [28, 91]. These examples are seemingly in contradiction to the Fano interference mechanism producing dispersive line shapes in HD.

More recently the Hefei group proposed a mechanism based on the standing wave produced inside the cavity from the strong circulating laser power, affecting the resonant molecules in the interaction path [53]. Spectra of two transitions of $^{13}\text{C}^{16}\text{O}_2$ were recorded in saturation. Whereas a relatively strong line with an Einstein coefficient of $A = 7 \times 10^{-4} \text{ s}^{-1}$ exhibits a symmetric line profile, a much weaker line with $A = 2 \times 10^{-5} \text{ s}^{-1}$ gives rise to a dispersive line shape [53, 166]. This is indicative of the fact that the distortion of the line shape, from symmetric to dispersion-like, sets in for very weak lines. Indeed for the R-lines in the (2-0) band of HD an Einstein coefficient of $A = 2.5 \times 10^{-5} \text{ s}^{-1}$ was measured [30], of similar magnitude as for the weakest of the two

6. SATURATION SPECTROSCOPY OF R(0), R(2) AND P(2) LINES IN THE (2-0) BAND OF HD

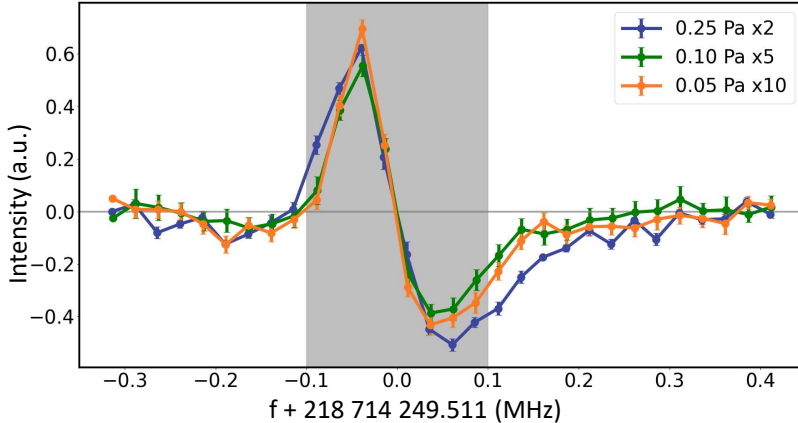


Figure 6.6: Spectrum of the R(14e) line in the band $(4\ 0\ 0\ 15) \leftarrow (0\ 0\ 0\ 01)$ of $^{12}\text{C}^{16}\text{O}_2$ measured in saturated absorption employing the NICE-OHMS technique using $1f$ demodulation. The spectra were recorded at 180 K for pressures as indicated in the legend. The broadening effect due to the dithering amplitude amounted to 20 kHz. The spectra have been scaled to their respective pressures with multiplication factors as indicated. The 0.0 value represents a frequency of 218 714 249 511 (100) kHz, deduced in the present study.

$^{13}\text{CO}_2$ lines.

In our laboratory, we have observed a similar dispersive line shape for a line of $^{12}\text{C}^{16}\text{O}_2$. The spectrum shown in Fig. 6.6 represents the R(14)e line in the vibrational band $(4\ 0\ 0\ 15) \leftarrow (0\ 0\ 0\ 01)$ [167]. At an Einstein coefficient of $A = 6 \times 10^{-6} \text{ s}^{-1}$ this is the molecular absorption line with the smallest transition moment ever detected in saturation spectroscopy. Of relevance for the present discussion is that $^{12}\text{C}^{16}\text{O}_2$ has no hyperfine substructure, so the dispersive line shape is observed for a species without underlying substructure. An additional peculiarity of this spectrum is that the observed linewidth is much narrower than the transit-time broadening of 290 kHz FWHM at 180 K.

6.5 Conclusion

The present experimental study reports accurate results for transition frequencies of the R(0), R(2) and P(2) lines in the (2-0) band of HD. The obtained accuracies face a limitation due to the fact that asymmet-

ric line shapes are observed for which no quantitative model exists, so the potential accuracy of frequency-comb-locked saturation spectroscopy could not be exploited. The findings nevertheless support earlier conclusions that the advanced fully ab initio calculations from version 7.3 of the H2SPECTRE program [153] deviate in a systematic fashion from experiment. Combination differences between observed vibrational frequencies can be translated into rotational level spacings in the $v = 0$ and $v = 2$ vibrational levels of HD at an accuracy better than for most direct measurement in purely rotational spectroscopy.

The observation of a dispersive line shape for the R(0) line contradicts the expectation of a predicted symmetric Lamb dip for that line from a model based in which the asymmetry is considered as resulting from underlying hyperfine structure and cross-over resonances. Alternative models as presented in literature are discussed. A quantitative model is however not yet developed. Therewith, a full and quantitative explanation of the line shape of saturated molecular transitions under high-power intracavity conditions remains a challenge for precision spectroscopy.

Financial support from the Netherlands Organisation for Scientific Research, via the Program “The Mysterious Size of the Proton” is gratefully acknowledged.

Lamb Dip of a Quadrupole Transition in H₂

Abstract

The saturated absorption spectrum of the hyperfineless S(0) quadrupole line in the (2-0) band of H₂ is measured at $\lambda = 1189$ nm, using the NICE-OHMS technique under cryogenic conditions (72 K). It is for the first time that a Lamb dip of a molecular quadrupole transition is recorded. At low (150-200 W) saturation powers a single narrow Lamb dip is observed, ruling out an underlying recoil doublet of 140 kHz. Studies of Doppler-detuned resonances show that the red-shifted recoil component can be made visible for low pressures and powers, and prove that the narrow Lamb dip must be interpreted as the blue recoil component. A transition frequency of 252 016 361 164 (8) kHz is extracted, which is off by -2.6 (1.6) MHz from molecular quantum electro-dynamical calculations therewith providing a challenge to theory.

This chapter is based on: *Lamb Dip of a Quadrupole Transition in H₂*, F.M.J. Cozijn, M.L. Diouf, and W. Ubachs, *Physical Review Letters* **131**, 073001 (2023)

7.1 Introduction

The hydrogen molecule has been a test ground for the development of molecular quantum mechanics for almost a century [168]. In the recent decade the level of precision has been accelerated in benchmark experimental studies focusing on its dissociation and ionization energies [9, 10], now reaching perfect agreement with first principles calculations based on four-particle variational calculations and including relativistic and quantum electrodynamic (QED) effects [4, 5]. The target of activity has in part shifted to measurements of the vibrational quantum in the hydrogen molecule. In the HD isotopologue vibrational transitions were measured in Doppler-broadened studies [28, 31] taking advantage of the weak dipole moment in this heteronuclear species. Lamb dip spectroscopy of HD vibrations could be performed at high precision [50, 145]. However, in the latter saturated absorption studies a problem of extracting rovibrational transition frequencies surfaced. Observed asymmetric lineshapes were interpreted in various ways, in terms of underlying hyperfine structure and cross-over resonances [51], of Fano-type interferences [52], and of effects of standing waves in the optical cavity [53]. This situation, imposing unclarity on the extraction of energy separations between quantum levels, has halted further progress in the precision metrology of HD, although a focused activity remains [161, 169].

In the homonuclear H₂ species selection rules govern that only quadrupole transitions are allowed and those are two orders of magnitude weaker than the dipole absorption transitions in HD [30]. Magnetic dipole transitions are allowed as well, although not in excitation from the $J = 0$ ground level [170]. Vibrational transitions in H₂ have been probed in Doppler-broadened spectroscopy [19, 25, 27], through combination differences of Doppler-free electronic transitions [35], and recently via stimulated Raman scattering [29]. While all rovibrational levels in HD are subject to complex hyperfine structure induced by the magnetic moment of both H and D nuclei, H₂ has the advantage that the levels in para-H₂ exhibit no hyperfine substructure. Until today no saturation spectroscopy has been performed on quadrupole transitions, neither in H₂ nor in any other molecule.

For performing saturation spectroscopy of an extremely weak quadrupole transition a novel setup was built as an upgrade from the setup used for the HD experiments [51, 145]. The optical cavity is redesigned to sup-

press vibrations and attached to a cryo-cooler to reach temperatures in the range 50-300 K. At the typical operation range of 72 K a larger fraction of the population is condensed into the H_2 $J = 0$ ground level, while the transit-time through the intracavity laser beam is increased, resulting in a smaller transit-time broadening. The laser, an external-cavity diode laser with a tapered amplifier running at 1189 nm, is locked to the cavity for short-term stability and to a frequency-comb-laser for sub-kHz accuracy in long-term measurements, thus also providing the absolute frequency scale. This stability allows for long time averaging over multiple scans. The 371 mm hemispherical resonator is equipped with highly reflective ($R > 0.99999$) mirrors of which the concave mirror has a radius-of-curvature of 2 m. This yields a finesse of 350,000, an intracavity circulating power of up to 10 kW, and a beam waist of 542 μm . Further details on the cryogenic noise-immune cavity-enhanced optical heterodyne molecular spectroscopy (NICE-OHMS) spectrometer will be given in a forthcoming publication [162].

7.2 Experiment

Detection is based on the technique of NICEOHMS [43, 56, 58] using sideband modulation of the carrier wave, at frequency $f_c \pm f_m$ with $f_m = 404$ MHz, matching the free-spectral-range (FSR) of the cavity for generating the heterodyne NICE-OHMS signal. The carrier and the two generated sidebands are locked to the cavity with Pound-Drever-Hall and DeVoe-Brewer [80] stabilization, respectively. Consequently, the three beams counterpropagate inside the cavity and interact with the molecules present, giving rise to various sub-Doppler spectroscopic signals from which two possible schemes are shown in Fig. 7.1. In panel (a), where the carrier is set on top of the resonance center, the counterpropagating carrier beams burn a hole in the center of the velocity distribution (at $v_z = 0$) and generate the generic Lamb dip signal. Additionally, saturation conditions are formed by the red/blue sidebands interacting simultaneously on molecules with velocities $k \cdot v_z = \pm f_m$ (k the wave vector of the light beam) and burning holes at their respective positions [171]. This effect is typically negligible for the weakly saturating regime and for conditions of low sideband power [55, 68].

In panel (b), on the other hand, the laser is detuned from the molecular resonance by $f_m/2 = 202$ MHz (or $\text{FSR}/2$). Here, one of the

7. LAMB DIP OF A QUADRUPOLE TRANSITION IN H₂

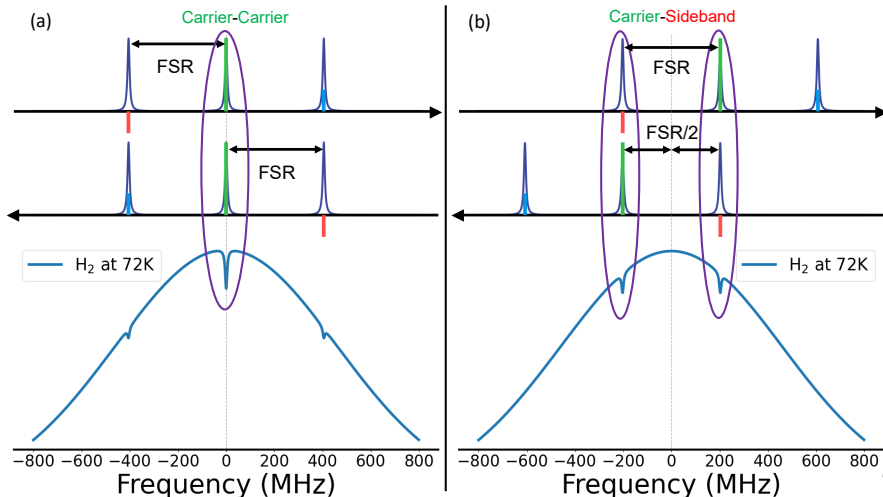


Figure 7.1: Possible interactions of the three fields (carrier and two sidebands) inside the cavity with a molecular resonance. Panel (a) represents the generic Lamb dip generated by the counterpropagating carrier beam on resonance. Additional holes are burned in the Doppler broadened profile with the combined interaction of the red/blue sidebands. In panel (b), the carrier is detuned off resonance by $f_m/2$ (or FSR/2). In that condition, one of the sidebands (in this example red) interacts with the counterpropagating carrier and consequently burns holes at $\pm FSR/2$.

sidebands (the red sideband in this example) in combination with the counterpropagating carrier beam interact with molecules with velocities $k \cdot v_z = \pm f_m/2$. As for this velocity class both beams are in resonance, a pump-probe scheme is formed, resulting in Doppler-detuned saturation signals. Since the required detuning is exactly known and the resulting Doppler-shift is equal, it can be seen as an alternative scheme for Doppler-free spectroscopy as only the known detuning needs to be considered to extract the transition frequency. The novelty of this scheme is that the ordinary on-resonance strong standing wave, present for the usual carrier-carrier saturation, is now converted to mostly a travelling wave due to the low intensity sideband. This allows to mitigate possible effects of the strong on-resonance standing wave.

In addition to the sideband modulation for the heterodyne signal, slow modulation of the cavity length is applied at 395 Hz with a peak-to-peak amplitude of 50 kHz. The resulting method of wm-NICE-OHMS allows for lock-in detection, where demodulation at the first derivative ($1f$) is

applied. The $1f$ profile function is defined as a (frequency) derivative of a typical dispersive Lorentzian profile [172]

$$f(\nu)_{1f} = \frac{4A[\Gamma^2 - 4(\nu - \nu_0)^2]}{[\Gamma^2 + 4(\nu - \nu_0)^2]^2}, \quad (7.1)$$

where the adjustable parameters are the line position ν_0 , the line intensity A , and the width Γ .

7.3 Results

7.3.1 Lamb dip of a quadrupole transition

Measurements of the S(0) (2-0) line were performed in the cryo-NICE-OHMS setup under a variety of conditions of intracavity power and pressure. Since the quadrupole transition is extremely weak, with a line strength $S = 1.6 \times 10^{-27}$ cm/molecule, and Einstein coefficient $A = 1.3 \times 10^{-7}$ s $^{-1}$ [27], it was anticipated that extreme powers would be required to obtain a saturation signal. At high power the spectra recorded displayed complex lineshapes, as shown in panel (a) of Fig. 7.2, reminiscent of the dispersive line profiles observed in HD [51–53, 146]. Surprisingly, by lowering the power, the complex lineshapes at 2.0 kW turn to an asymmetric dispersive-like profile at 1.0 kW, to finally a symmetric profile at 150 W. Panel (b) and (c) show the symmetric Lamb dip obtained at the lower powers of 150 W and 200 W, where each individual measurement was obtained after 12 hours of averaging. A $1f$ dispersive Lorentzian (Eq. 7.1) fit was then used on the symmetric profiles so as to extract relevant parameters such as the Lamb dip position and the linewidth.

Large sets of data were obtained, mainly at 150 W, 200 W, and 300 W, where symmetric lines were observed, but also at higher powers. The extracted positions of the Lamb dip were treated in a multivariate analysis yielding a transition frequency extrapolated to zero-pressure and zero-power of $f = 252\,016\,361\,234.4$ (7.3) kHz, which we will refer to as the ‘generic Lamb dip’ in the following. Some subsets of pressure-dependent (at 150 W) and power-dependent (at 0.25 Pa and 0.10 Pa) curves are shown in Fig. 7.3.

Extrapolating the extracted widths to zero pressure yields a linewidth limit of 205 kHz (FWHM) for 150 W, which still overestimates the ac-

7. LAMB DIP OF A QUADRUPOLE TRANSITION IN H₂

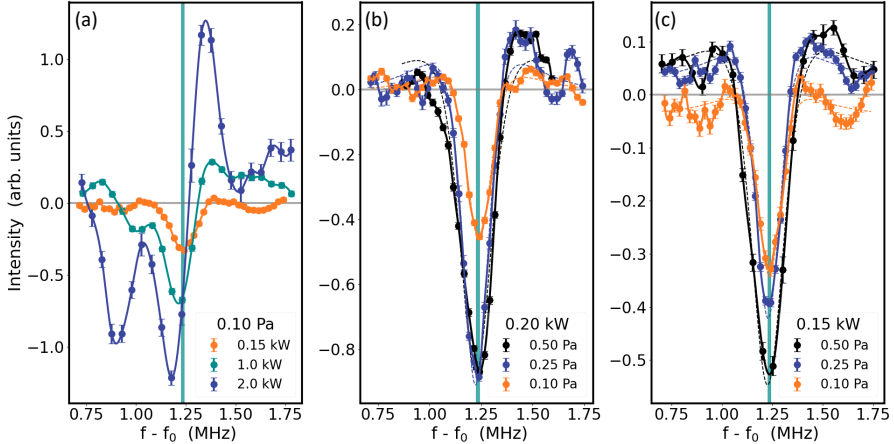


Figure 7.2: Recorded spectra of the measured Lamb dip for the S(0) (2-0) quadrupole transition in H₂ at 72 K at (a) 0.10 Pa for different circulating power as indicated. Panel (b) and (c) respectively show the measured spectra at the lower circulating powers of 150 Watt and 200 Watt for different pressure indicated. A $1f$ dispersive Lorentzian (Eq. 7.1) was superimposed on the measured spectra. The absolute frequency scale is given via $f_0 = 252\,016\,360$ MHz.

tual limit as dithering effects are not removed. These values are considerably smaller than the calculated 471 kHz transit-time width (for 72 K) [173] and can be attributed to the selection of cold molecules in the weakly saturating regime [74], as observed in our previous work on HD [145]. The observed width corresponds to a most probable velocity of $v_{\text{mp}} = 335$ m/s and temperature of around 13 K.

In order to accurately extract the transition frequency one needs to consider and correct for the known Doppler shifts and the resulting recoil from conservation of momentum. The total energy carried by a photon for making a transition or released from emission is expressed as [76]

$$E_{\text{photon}} = h\nu_0 \pm \frac{h\vec{k} \cdot \vec{v}}{2\pi} \pm \frac{(h\nu_0)^2}{2mc^2} - \frac{(h\nu_0)v^2}{2c^2}. \quad (7.2)$$

Here, $h\nu_0$ is the energy difference between quantum levels. The second term is the first order Doppler shift and is equal to zero under conditions of saturation ($\vec{k} \cdot \vec{v} = 0$ for the generic Lamb dip). The third term is the recoil shift, where the plus/minus sign refers to the case of absorption/stimulated emission. The final term represents the second-order

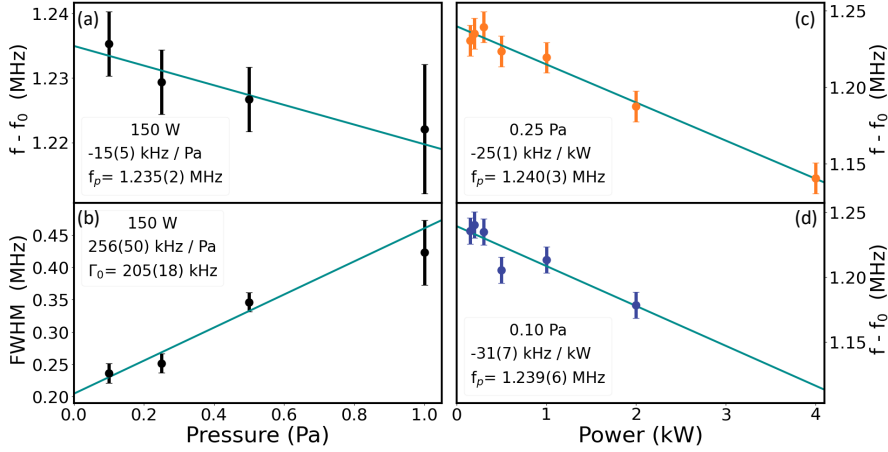


Figure 7.3: Extracted positions of the S(0) Lamb dip at different powers and pressures and extrapolation to zero values (f_p). (a) Pressure dependence and shift at $P = 150$ W; (b) Pressure dependent width at 150 W (FWHM); (c) and (d) Power-dependent shifts at $p = 0.25$ and 0.1 Pa. The pressure- and power-dependent slopes are as indicated. The absolute frequency scale is given via $f_0 = 252\,016\,360$ MHz.

(relativistic) Doppler effect, which is as small as 160 Hz (for 13 K).

7.3.2 Recoil doublet in saturation spectroscopy

In saturation spectroscopy two recoil components are associated with each quantum transition due to conservation of momentum [174]. A high-frequency (blue-detuned) component occurs for absorption from ground-state particles, and a low-frequency (red-detuned) component for stimulated emission from excited-state particles (Fig. 7.4). Both components will form individual Lamb dips as a characteristic recoil doublet, split at twice the recoil shift and centered around the resonance center. Despite the significance of recoil on extracting the transition frequency, it is often neglected in saturation spectroscopy as typically the observed linewidths are significantly larger than the recoil doublet splitting and thereby making the recoil doublet unresolvable. Nevertheless, there have been studies in which the recoil doublet has been successfully resolved in atoms [175–178] and in molecules [73–75, 179].

For the present case of H_2 and the transition frequency of the S(0) line this recoil amounts to 70 kHz and a total splitting of 140 kHz. As this is

7. LAMB DIP OF A QUADRUPOLE TRANSITION IN H₂

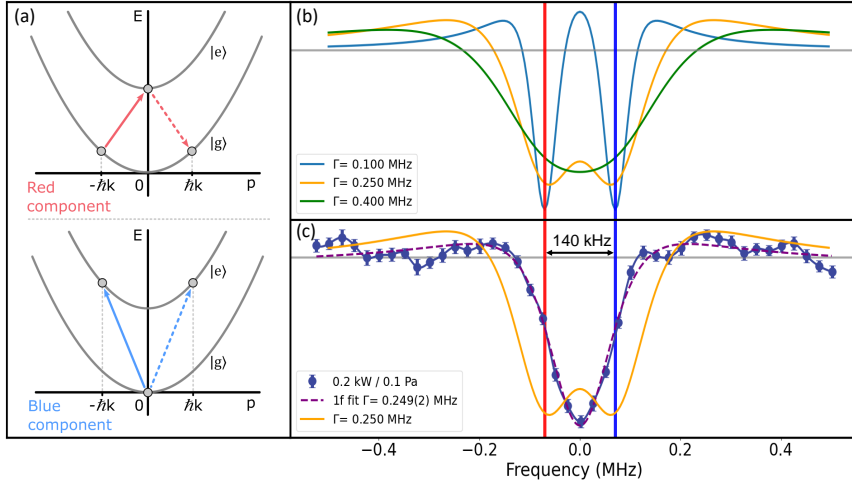


Figure 7.4: (a) Schematic of the blue (absorption) and red (stimulated emission) recoil components when the two counterpropagating lasers are close to a resonant transition $|e\rangle \leftarrow |g\rangle$. (b) Modeled profiles of a recoil doublet for the expected recoil splitting of 140 kHz and for varying levels of broadening. (c) A measurement of a 'generic Lamb dip' at a pressure 0.1 Pa, intracavity power of 0.2 kW and temperature 72 K. The observed symmetric lineshape cannot be modeled by any of the simulated profiles that include the 140 kHz recoil splitting while the simple $1f$ dispersive Lorentzian fit produces perfect agreement.

only marginally smaller than the observed linewidth of 230 kHz, effects of the recoil splitting are expected to be visible on the observed lineshape. Model calculations are presented for the known recoil doublet splitting and a variety of widths that each component may obtain (Fig. 7.4). Comparison of simulated profiles with measurements reveals that the observed lineshape cannot be composed from both recoil components. In fact, in Fig. 7.4(b), a distinction is clearly seen as the measured Lamb dip does not display any hint of an unresolved recoil doublet and is perfectly fitted by a $1f$ Lorentzian profile composed of a single transition. This leads to the conclusion that the observed generic Lamb dip at low power cannot consist of both recoil components and that suppression of one of the recoil components has occurred.

There have been studies on suppression on both the red-shifted [176] and blue-shifted [177] recoil components. In either case this was performed by depopulating the upper-state or ground-state respectively through (optical) pumping. Also in an early observation of the resolved recoil

doublet unequal intensity components were found, in which the red-shifted component exhibited decreased intensity under some conditions [73]. In the theoretical derivation from Kol'chenko et al. [174] it was found that the ratio of the depths of the recoil components are determined by the lifetimes of the states involved. From these observations and findings it can be reasoned that due to the two-step process of the stimulated emission scheme and the typical lower lifetime of the excited state, the red-shifted recoil component is more easily suppressed.

In the case of H_2 the natural lifetimes of states are non-restrictive and other effects of relaxation must be considered. Collisional effects, the finite transit times and effects of the strong standing wave can all be considered as effective methods of depopulation or dephasing. Compared to the previous studies where the recoil doublet was successfully resolved, our present study operates at around one to two orders of magnitude higher pressure. The most striking difference between this study and the previous studies on the CH_4 molecule is the use of extreme laser intensities to saturate the weak quadrupole transition. In our study, up to 10-12 orders of magnitude higher power densities [74, 75] are present which can lead to significant standing wave effects in the optical resonator.

Effects of a strong standing wave on neutral molecules had been theoretically explored in the past by Letokhov and Chebotayev [78]. The finite polarizability of molecules leads to an axial striction force due to the strong electric field gradient, imposing axial velocity modulation, or ultimately, even axial trapping of molecules. The resulting velocity modulation can easily lead to effective dephasing of resonant molecules and can be considered as a depopulation effect. For the condition on resonance, which is usually the case for saturation spectroscopy, the striction force can be severely enhanced as the dynamic polarizability changes significantly near the molecular resonance. Recently the effect of standing waves on the vibrational spectrum of HD [53] and H_2 [180] was considered.

7.3.3 Carrier-Sideband saturation spectroscopy

In order to mitigate the possible effects of the on-resonance strong standing wave and simultaneously prolong the transit time through the intracavity laser beam, Doppler-detuned measurements were performed at $\text{FSR}/2$ detuning, as shown in Fig. 7.1(b). A direct overlap of the two

7. LAMB DIP OF A QUADRUPOLE TRANSITION IN H₂

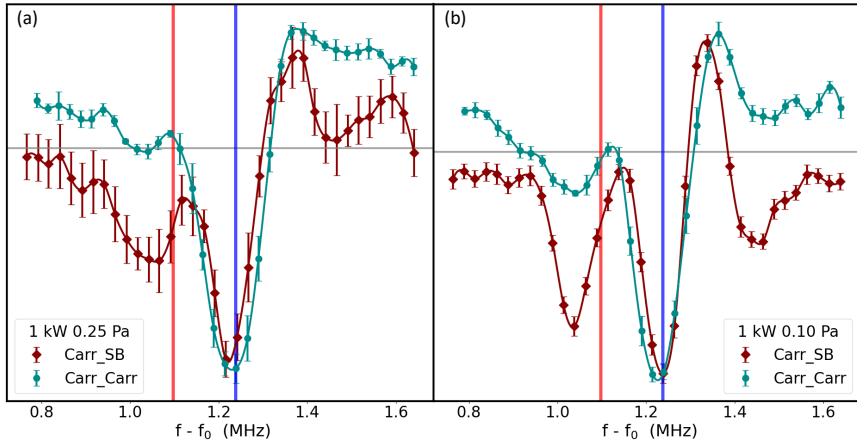


Figure 7.5: Comparison of NICE-OHMS signals for Carrier-Carrier and Carrier-Sideband (FSR/2 detuned) schemes at 1 kW intracavity power and at (a) 0.25 Pa and (b) 0.10 Pa. The sideband (probe) has been kept to a low power of 5 W, equivalent to 0.5% of the carrier (pump) power. Note that the blue line corresponds to the measured frequency of the generic Lamb dip as in Fig. 7.2.

different NICE-OHMS signals (the central carrier-carrier resonance and the FSR/2 detuned carrier-sideband) is accomplished by correcting for the detuning frequency (Fig. 7.5). Comparison between both measurement schemes are made and a blue and red marker for the supposed recoil positions are added, where the blue line indicates the extracted frequency position for the 'generic Lamb dip'. This shows that under reduced probe (sideband) powers the red recoil component increases in amplitude, from which can be concluded that the 'generic Lamb dip' at low powers is composed of the blue recoil component only. Moreover, at reduced pressure and very low sideband amplitude, the red recoil component is nearly fully recovered. Note that at the powers of 1 kW the line shapes of individual components become asymmetric. The summation of the unequal intensity recoil components then causes an apparent frequency shift of the weakest (red) component.

From these systematic studies we conclude that the observed generic Lamb dip corresponds to the blue recoil shifted component. Correcting for the recoil shift of 70 kHz, and taking into account the contributions to the overall uncertainty (7.3 kHz statistical, with pressure and power effects included, and calibration 1 kHz) the frequency of the S(0)

(2-0) quantum transition in H_2 is determined at 252 016 361 164 (8) kHz, with a relative precision of 3×10^{-11} representing the most accurate determination of a vibrational splitting in a hydrogen isotopologue [36].

7.4 Conclusion

Comparing with the best theoretical result for the $S(0)$ transition frequency, obtained via the approach of non-adiabatic perturbation theory (NAPT) [159] and computed with the H2SPECTRE code [181] the experimental result is higher by 2.6 MHz. The uncertainty from this NAPT approach is 1.6 MHz, hence the deviation between experiment and theory is at 1.6σ , and determined by the $E^{(5)}$ leading order QED-term. Part of this $E^{(5)}$ term was recently recomputed [182] but the issue of systematic discrepancies for vibrational splittings in HD, at the level of 1.9σ , was not resolved. Now deviations of a similar size are found for the homonuclear H_2 species. For the binding energy of two particular levels in H_2 , $J = 0, 1$ in $v = 0$, separate and dedicated calculations of relativistic and QED corrections were carried out employing nonadiabatic explicitly correlated Gaussian wave functions, yielding an accuracy of 0.78 MHz [4]. The present experimental results pose a challenging test bench for such advanced theoretical approach.

As an outlook we note that the lifetimes of all rovibrational levels in the H_2 electronic ground state exceed 10^5 s [183], thus allowing in principle for metrology of 20-digit precision if the natural lifetime limit can be reached. This will push tests of the computational approaches to molecular quantum electrodynamics and searches for physics beyond the Standard Model [6] to the extreme. The present experiment signifies a step in that direction.

Financial support from the Netherlands Organisation for Scientific Research (NWO), via the Program “The Mysterious Size of the Proton” is gratefully acknowledged. We thank several members of the Quantum Metrology & Laser Applications group at VU Amsterdam (Edcel Salumbides, Max Beyer, Kjeld Eikema, Jeroen Koelemeij, Yuri van der Werf, Hendrick Bethlem) for helpful discussions.

Hyperfine structure in a vibrational quadrupole transition of ortho-H₂

Abstract

A Lamb dip spectroscopic measurement of the Q(1) transition in the (2-0) overtone band of ortho-H₂ is performed with the ultra-sensitive NICE-OHMS intracavity absorption technique at 1238 nm. For the first time individual hyperfine components of a vibrational transition in H₂ are resolved, displaying a pattern of 4 overlapping components with singly isolated components at the red and blue side. Weak components at a line strength of 4.4×10^{-28} cm/molecule could be observed as a Lamb dip. Analysis yields a hyperfineless purely rovibrational transition frequency for the Q(1) (2-0) line in H₂ at unprecedented accuracy for any rovibrational transition in a molecular hydrogen isotopologue. Its frequency is 242 091 630 140 (9) kHz under the assumption that only a blue recoil component is observed. A 1.7σ deviation from the most advanced quantum electrodynamics calculations is obtained, forming a challenge for theory.

This chapter is based on: *Hyperfine structure in a vibrational quadrupole transition of ortho-H₂*, M.L. Diouf, F.M.J. Cozijn and W. Ubachs, *Molecular Physics*, e2304101 (2024)

8.1 Introduction

In the early days of quantum mechanics it became readily understood that the coupling of the nuclear spins of two protons ($I_p = \frac{1}{2}$) effectively gives rise to two separate molecular hydrogen species: one with a combined spin of $I = 0$ for para-hydrogen, and one with a spin of $I = 1$ for ortho-hydrogen. The Pauli principle, requesting an anti-symmetric wave function under permutation of two identical fermions, rules that the para-species only accommodates quantum states of even rotational angular momentum J , while the ortho-species has $J = \text{odd}$. This separation into non-convertible species strongly impacts the thermal properties of hydrogen gas, in particular the specific heat, as discussed by Farkas [184].

Only in ortho-H₂ the proton spins give rise to a hyperfine structure as was investigated in the measurement of radio-frequency splittings in the $J = 1$ rotational state by Ramsey and coworkers [185–187]. Notwithstanding the vast amount of precise spectroscopic studies of the hydrogen molecule over decades, the hyperfine substructure is hitherto not observed in the vibrational spectrum [19, 26, 188], the Raman spectrum [29], neither in the strong dipole-allowed Lyman and Werner bands [189, 190], nor in the large number of optical transitions connecting electronically excited states of singlet symmetry [191].

In some transitions involving triplet states hyperfine structure could be resolved, due to the coupling of the $S = 1$ electron spin to the nuclear spins. The Ramsey-type technique was extended to investigate the hyperfine structure of the metastable $c^3\Pi_u$ state [192]. Miller and Freund developed the microwave optical magnetic resonance technique allowing them to resolve the hyperfine structure in the $d^3\Pi_u$ and $k^3\Pi_u$ triplet states [193, 194]. Ottinger and coworkers also employed beams of metastable H₂ to unravel the hyperfine structure in $g^3\Sigma_g^+$, $h^3\Sigma_g^+$, $i^3\Pi_g$ and $j^3\Delta_g$ states [195]. A special case is that of the hyperfine structure in Rydberg states of orthohydrogen, which was measured through millimeter-wave spectroscopy [196]. In this case the unpaired electron of the H₂⁺ ion core induces a strong electronic-nuclear spin coupling, giving rise to large hyperfine splittings, while the very small intervals probed by millimeter waves significantly reduce the Doppler width. Some of these splittings could also be resolved via laser excitation to high- n Rydberg states [10].

In the present study the hyperfine structure in a vibrational transition

is resolved for the first time in H_2 . As an extension to a previous work on the measurement of the S(0) line in the (2-0) overtone band of para- H_2 [197] now the Q(1) line in ortho- H_2 is observed as a Lamb dip. The sensitivity to record saturation spectra of extremely weak quadrupole transitions is achieved via the technique of NICE-OHMS.

8.2 Experiment

Saturation spectroscopy of the Q(1) quadrupole overtone transition is performed in a specially designed and built vibration-isolated and cryo-cooled cavity setup for a measurement of the S(0) line in para- H_2 [197]. For the implementation of the NICE-OHMS spectroscopy methods [56, 58], involving locking of the external cavity diode laser to the cavity and to a frequency comb laser (disciplined by a Cs-clock and by GPS), as well as an additional low-frequency wavelength modulation and lock-in detection, and absolute frequency measurement, we refer to previous reports on investigations of the HD molecule [145] and of water [154].

Two major differences with respect to the para- H_2 study are implemented. The concave mirror in the hemispherical resonator of length 371 mm, now has a radius-of-curvature of 6 m. This results in a larger intracavity beam waist (radius 754 μm), therewith somewhat reducing the line broadening due to transit-time effects. The wavelength of the external-cavity diode laser now runs at 1238 nm, outside the gain profile of the tapered amplifier, which is bypassed in the current study. For the highly reflective mirrors ($R > 0.999989$) yielding a finesse of 290,000 now the maximum intracavity intensity is limited to 300 W. Further, the typical temperature operation range of 72 K was kept, and pressure settings are in the range 0.25-1.0 Pa. The configuration yields the stability for long time averaging over multiple scans for many hours.

8.3 Results

8.3.1 Hyperfine resolved Lamb dip measurements

A characteristic spectrum of the Q(1) line of ortho- H_2 in the (2-0) band, measured as a saturated absorption signal, is presented in Fig. 8.1. Measurement conditions are 300 W intracavity power (at beam diameter 1.5 mm), 0.25 Pa H_2 pressure, and 72 K temperature. For compari-

8. HYPERFINE STRUCTURE IN A VIBRATIONAL QUADRUPOLE TRANSITION OF ORTHO- H_2

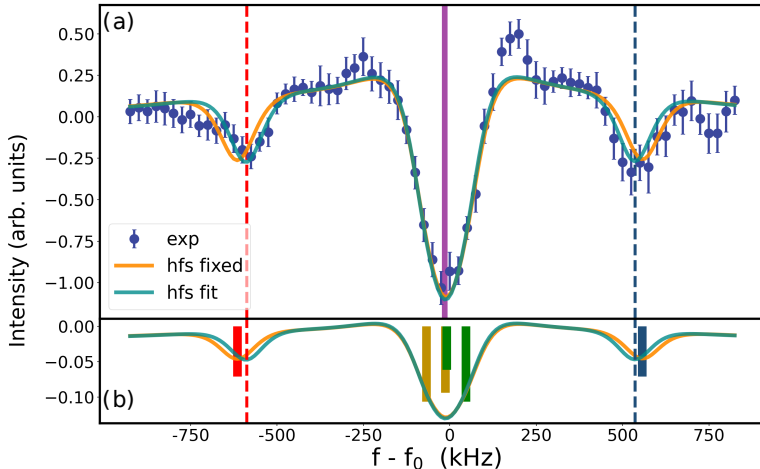


Figure 8.1: (a) Recorded spectrum of the Q(1) line in the (2-0) band of H_2 measured at $\lambda = 1238$ nm, a temperature of 72 K, a total hydrogen pressure of 0.25 Pa and intracavity powers of 300 W. The absolute frequency scale is given via $f_0 = 242\,091\,630\,198$ kHz. (b) Hyperfine components as a stick spectrum with relative intensities from Ref. [198] and color coding congruent with that of Fig. 8.2. The orange curve (in both panels) represents the result of a fit while keeping the hyperfine structure splittings fixed to the calculated values. The green curve gives the result for a fit in which the positions of the outer components were varied. The vertical dashed lines indicate the location of the hyperfine components when fitted.

son a stick spectrum, based on computations by Jozwiak et al. [198], is displayed. The hyperfine level structure of the Q(1) line, shown in Fig. 8.2, also based on Ref. [198], comprises 6 hyperfine components, of which 4 convolve into the central strong component, and one isolated and red-shifted (red colored) and one blue shifted by the approximately the same amount (blue colored). The length of the sticks in Fig. 8.1 corresponds to the computed (relative) intensities [199], that are listed in Table 8.1. Note that the total absorption line strength over all hyperfine components, and defined for linear absorption, is as small as 3.9×10^{-27} cm/molecule. The isolated side components have a line strength of 4.4×10^{-28} cm/molecule. Their detection marks one of the weakest resonances observed as Lamb dips.

The experimental spectrum is fitted to the expected line shape of a $1f$ -demodulated NICE-OHMS signal as measured in the present study [172,

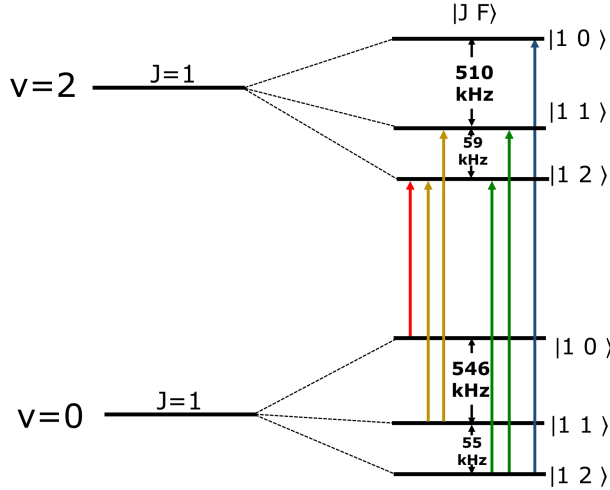


Figure 8.2: Stick spectrum representing all hyperfine components of the Q(1) line in the (2-0) band of H_2 based on calculations by Jozwiak et al. [198]. While the ground state is $v = 0$, the excited state is $v = 2$, the quantum numbers in brackets $|J, F\rangle$ represent the rotational angular momentum J and the total angular momentum F also including nuclear spin. The color code of the components mirrors that of Fig. 8.1.

197]:

$$F(f)_{1f} = \sum_i \frac{4 A_i [\Gamma^2 - 4(f - (f_i - f_0))^2]}{[\Gamma^2 + 4(f - f_i - f_0))^2]^2}. \quad (8.1)$$

In this fitting procedure 6 hyperfine components are included at frequency f_i , whereby the frequency splittings are fixed to the level scheme of Fig. 8.2, and the intensities to the relative transition moments from theory [180, 198] (see Table 8.1). The fit results in three parameters: an intensity value A , a central frequency of the hyperfineless position f_0 , and a value for the width parameter Γ , which is assumed to be equal for all components.

8.3.2 Systematic effects

The absolute frequency of the f_0 position in the spectrum is determined at $f_0 = 242\,091\,630\,198$ kHz, at a 5 kHz statistical uncertainty (1σ) resulting from the fitting procedure. The fit is represented by the thin orange line in Fig. 8.1. It was produced from a least-squares approach,

8. HYPERFINE STRUCTURE IN A VIBRATIONAL QUADRUPOLE TRANSITION OF ORTHO-H₂

Table 8.1: Relative intensities of the six hyperfine components of the Q(1) line in the (2-0) band of H₂ as extracted from [199]. The intensities are listed in relative numbers; when multiplied by 10⁻²⁸ the numbers present the absolute line strengths in cm/molecule. In the final column the transition frequencies of the individual hyperfine components are listed with respect to the purely rovibrational or hyperfineless transition, in units of kHz.

Component	Intensity	Frequency (kHz)
1, 2 >← 1, 0 >	4.38	-599.5
1, 2 >← 1, 1 >	9.86	-53.0
1, 2 >← 1, 2 >	7.67	2.3
1, 1 >← 1, 1 >	3.29	6.1
1, 1 >← 1, 2 >	9.86	61.5
1, 0 >← 1, 2 >	4.38	571.8

fixing the relative intensities and the hyperfine splittings to the computed values by Jozwiak et al. [198], while a common width parameter $\Gamma = 210$ (13) kHz (FWHM) was determined. In an alternative fitting approach the frequency positions of the outer two components of the hyperfine structure were varied. Where theory predicts a splitting of 1171 kHz, the experimentally deduced splitting is 1124 (15) kHz, deviating by a significant 3σ from prediction. Both outer hyperfine components become shifted inwards toward the hyperfineless zero-position by 27 (7) kHz and -21 (11) kHz, for the red and blue components respectively. The position of the zero-point shifts only by 2 kHz, which we adopt as a contribution to the systematic error budget.

A number of additional systematic effects should be considered before extracting the hyperfineless purely rovibrational transition frequency. For an assessment of the pressure shift comparative measurements were performed at pressures of 0.25 Pa (as displayed in Fig. 8.1) and at 0.5 Pa. Results differ by 1 (7) kHz, at insufficient precision to determine a pressure shift coefficient. For the S(0) line in para-H₂ a pressure shift of 15 kHz/Pa was determined [197]. Based on this we estimate a pressure shift correction of +3 (1) kHz. The non-availability of a tapered amplifier at $\lambda = 1238$ nm prohibited measurement of a power dependence. Hence we relied on the measured coefficient of 12(1) kHz GW⁻¹cm² for the S(0) line at 0.25 Pa; based on this we implement a power correction of +4 (1) kHz for the present measurement at 300 W. The correction for the second order Doppler effect is negligibly small (< 1 kHz) [197]. Considering this, the frequency for the purely rovibrational Q(1) tran-

sition is $f_0 = 242\,091\,630\,205$ (9) kHz. The contributions to the error budget and the extraction of the final frequency are listed in Table 8.2.

Table 8.2: Error budget for the measurement of the purely rovibrational transition frequency of the Q(1) line in the (2-0) band of H₂. For details see main text.

Effect	Frequency (kHz)	Uncertainty (kHz)
Fitted frequency	242 091 630 198	5
Hyperfine zero	-	2
Pressure shift	3	1
Power shift	4	1
Blue recoil	-65	-
Final frequency	242 091 630 140	9

8.3.3 Recoil doublet analysis

From early work in laser spectroscopy [73, 75] a recoil doublet, comprising of a red and a blue shifted recoil component at $f_{\text{rec}} = \pm h\nu_0/2mc^2$ is to be expected in saturation spectroscopy. Intriguingly, such a recoil doublet was not observed in our previous study on the S(0) quadrupole transition of H₂ [197]. In the present investigation of the Q(1) line, effects of a recoil doublet on the experimental lineshape is expected at a recoil-doublet splitting of 2×65 kHz.

In Fig. 8.3 the observed experimental data is analyzed for possible effects of a recoil doublet. In panel (a) a comparison is made between the experimental data and a single recoil component of width $\Gamma = 200$ kHz. In panel (b) the experimental data is compared with simulations in which each individual hyperfine component is convoluted with the expected recoil doublet for varying widths Γ . For the low-frequency hyperfine component, it follows that it is not possible to match the observed line shape with any of the simulated doublet models. For the central feature it is directly apparent that all three models are significantly broader than the experimental data. From this analysis we conclude that the observed Q(1) line cannot be composed of a recoil doublet, similar to the case of the S(0) transition in para-H₂.

In the present case of Q(1) it cannot be decided whether the red or blue recoil component is observed as the measurement of a doublet under different power conditions could not be performed, due to the lack of a tapered amplifier at $\lambda = 1238$ nm. Hence, the observed single component is interpreted as the blue recoil component, in analogy to the case

8. HYPERFINE STRUCTURE IN A VIBRATIONAL QUADRUPOLE TRANSITION OF ORTHO- H_2

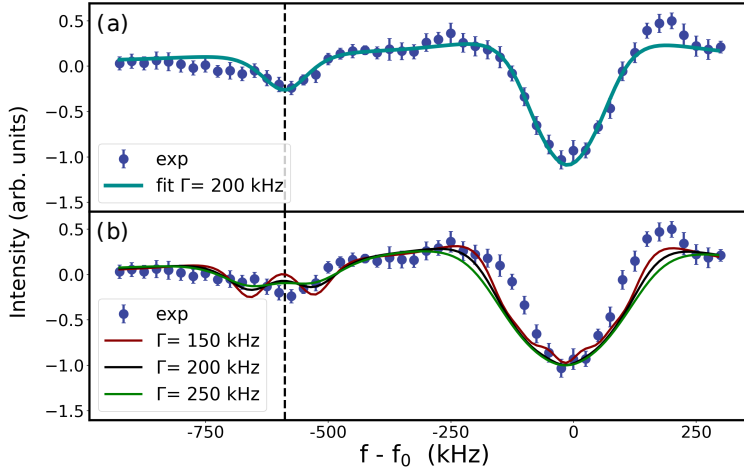


Figure 8.3: Analysis of the possible contribution of a recoil doublet to the experimental data of the Q(1) line. The vertical dashed line indicates the fitted line position of the low-frequency isolated hyperfine transition as in Fig. 8.1. (a) A model fit consisting of a single recoil component to the experimental data, yielding a 200 kHz (FWHM) transition width. (b) A comparison of the experimental data with a model consisting of the recoil doublet splitting of 130 kHz for varying widths as given in the legend.

of the S(0) line, for which further proof was provided [197]. Under this assumption the frequency of the purely rovibrational transition is then $f_0 = 242\,091\,630\,140$ (9) kHz.

The switch to a 6 m radius mirror compared to the 2 m mirror in the previous study on the S(0) transition [197] resulted in a decrease of the observed linewidths at 0.25 Pa from around 250 kHz to 200 kHz currently. This narrowing is a direct result of the 39% increase in transit-time due to the larger beam size. The observed 200 kHz width is also significantly lower than the predicted transit-time width of 320 kHz (for a temperature of 72 K), which can be attributed to the selection of cold molecules in the weakly saturating regime. While a width-to-pressure dependency is absent in this study, preventing extrapolation to zero pressure, an upper limit on the effective temperature can be set at 28 K. The less-than-anticipated narrowing from the transit-time increase can be attributed to the still significant collisional broadening at 0.25 Pa, which limits a further decrease of the observed widths. Another factor at play due to the increased beam size and thus transit-time, can be

that faster molecules start to participate in the saturation signal and somewhat limit the effect of the increased beam size on the linewidth.

8.4 Discussion

The present result for the Q(1) (2-0) purely rovibrational transition frequency signifies a benchmark for comparing with state-of-the-art quantum ab initio calculations in the framework of relativistic quantum electrodynamics (QED). The theoretical results are produced at various levels of sophistication, either via non-adiabatic perturbation theory [151, 159], or via a four-particle variational calculation [4, 5]. The results are being made public via the program suite H2SPECTRE, the latest version being 7.4 [200]. Theoretical transition frequencies in the (2-0) bands of the hydrogen isotopologues yield uncertainties of about 1.0 MHz. Previous results and compilations of transition frequencies of the (2-0) vibrational bands witnessed higher experimental values with respect to theory, for HD [36, 201], for H₂ [188, 197], and for D₂ [37, 202]. For a vast number of lines there occurs a systematic and therefore significant offset between experiment and theory of $1.7 - 1.8\sigma$, where the uncertainty is fully determined by the theoretical results.

The present experimental result represents one of the most accurate measurements of vibrational transitions in the hydrogen isotopologues. The value $f_{\text{exp}} = 242\,091\,630\,140$ (9) kHz may be compared with the theoretical value of $f_{\text{theory}} = 242\,091\,627.70$ (1.47) MHz, which is again off by 1.7σ . This result reconfirms the existing challenge for theory. Recently it was discussed that a more advanced treatment of the leading order QED term, scaling like $m\alpha^5$ is required [182].

8.5 Conclusion

In the present experimental study, performing saturation spectroscopy of the Q(1) transition in the (2-0) band with the NICE-OHMS technique, for the first time hyperfine structure is resolved in a vibrational transition of H₂. The overall pattern of predicted hyperfine splittings in the H₂ vibrational transition [198] is found in reasonable agreement with the present experimental result, although a 3σ deviation is found for the splitting between the outermost spectral components. The purely rotational transition frequency deduced from the center-of-gravity of the

8. HYPERFINE STRUCTURE IN A VIBRATIONAL QUADRUPOLE TRANSITION OF ORTHO-H₂

hyperfine structure yields a value accurate to 9 kHz, establishing the most accurate vibrational transition in H₂ measured so far. The observed deviation from quantum ab initio computations for this purely rovibrational structure is at the 1.7σ level, similar to previous findings on other molecular hydrogen isotopologues. This forms a challenge for theory.

Financial support from the Netherlands Organisation for Scientific Research (NWO), via the Program “The Mysterious Size of the Proton” is gratefully acknowledged.

Precision Measurement of Vibrational Quanta in Tritium Hydride (HT)

Abstract

Saturated absorption measurements of transitions in the (2-0) band of radioactive tritium hydride (HT) are performed with the ultra-sensitive NICE-OHMS intracavity absorption technique in the range 1460-1510 nm. The hyperfine structure of rovibrational transitions of HT, in contrast to that of HD, exhibits a single isolated hyperfine component, allowing for the accurate determination of hyperfineless rovibrational transition frequencies, resulting in $R(0) = 203\,396\,426\,692$ (22) kHz and $R(1) = 205\,380\,033\,644$ (21) kHz. This corresponds to an accuracy three orders of magnitude better than previous measurements in tritiated hydrogen molecules. Observation of an isolated component in P(1) with reversed signal amplitude contradicts models for line shapes in HD based on cross-over resonances.

This chapter is based on: *Precision Measurement of Vibrational Quanta in Tritium Hydride (HT)*, F.M.J. Cozijn, M.L. Diouf, V. Hermann, M. Schlösser and W. Ubachs, *Physical Review Letters* **132**, 113002 (2024)

9.1 Introduction

In the recent decade rapid progress has been made in precision investigations of the quantum level structure of the smallest neutral molecular entity, the hydrogen molecule, existing as three stable isotopologues. On the theory side non-relativistic quantum electrodynamics (QED) has been developed into the framework of nonadiabatic perturbation theory (NAPT) [151, 159]. This has resulted in a publicly available code for computing level energies in molecular hydrogen [200]. In parallel, so-called pre-BO methods have been developed that treat the 4-particle system in a direct variational approach [203, 204] leading to the most accurate binding energies of molecular hydrogen [4, 5]. Such very accurate computations have recently been performed for vibrational transitions in tritium-bearing hydrogen molecular isotopologues [205]. On the experimental side a series of measurements has been reported for the benchmark quantity of the dissociation and ionization energies of H₂ [9], D₂ [11], and HD [12] now reaching accuracy at the 1 MHz level and in agreement with theory.

As an alternative to the measurements based on electronic excitation, studies of vibrational splittings in the ($X^1\Sigma_g^+$) electronic ground state of molecular hydrogen may lead to improved accuracy and more advanced tests of theory in view of the long lifetimes of the states involved. The weak dipole moment in hydrogen deuteride (HD) heteronuclear species gives access to dipole-allowed vibrational transitions, measured via Doppler-broadened absorption spectroscopy [28, 30, 31], and recently also in saturation spectroscopy [50, 145]. Exploitation of the full potential of the extremely narrow Lamb dips is hampered by the asymmetry in the observed line shapes. This was ascribed to underlying and unresolved hyperfine structures [51], but also to other phenomena such as the effect of standing waves in intra-cavity experiments [53, 180]. The HT isotopologue is similarly accessible for dipole transitions. The gas loads required to operate molecular beams cannot be supported by the exempted activity limit (1 GBq, corresponding to 11.3 mbar·cm³ for T₂) allowed in any laser laboratory inside the European Union. Experience with spectroscopic measurements on small samples of tritium containing hydrogen molecules was recently gained by our collaborative team in performing Coherent Anti-Stokes Raman (CARS) measurements on static samples of T₂ [38], DT [39] and HT [40] achieving frequency accuracies of 10 MHz in vibrational splittings. Before, bench-

mark studies had been performed via spontaneous Raman [206] and via intracavity laser absorption [207].

In rovibrational transitions the HT isotopologue appears to have an advantageous hyperfine structure when compared to HD. It is simpler with less components, as $I_T = 1/2$ compared to $I_D = 1$, but more importantly, rovibrational transitions in HT exhibit a single isolated hyperfine component that can possibly be resolved in a high resolution saturated absorption study [208]. The present experimental study exploits this advantage.

9.2 Experiment

9.2.1 Radiation-safe design for tritiated hydrogen

Saturation spectroscopy of HT rovibrational lines is performed in an optical configuration similar to the one used for the HD experiments [51, 145]. However, a major redesign (see Fig. 9.1) was undertaken in order to operate a Noise-Immune Cavity-Enhanced Optical Heterodyne Molecular Spectroscopy (NICE-OHMS) experiment under radiation-safe conditions.

Two layers of gas sealing windows (wedged and angled) were used for radiation safety. A small bore diameter ($d = 10$ mm) cavity was coupled to two connected vacuum sealable chambers containing sintered porous getter materials (SAES, St171). These getter materials have the property that they perform as an active pump for all gases when cooling down, but do release only hydrogen when heated to temperatures in the range 600-900 °C. A first hydrogen-loaded getter was prepared at the TLK tritium gas-mixture infrastructure TRIHYDE [209] with a $H_2:HT:T_2$ mixture (with H:T= 1:1) equivalent to 1 GBq activity. Since the getter stores hydrogen in atomic form, pure samples of HT could not be operated with [210].

After loading the getter the tritium was transported to LaserLab Amsterdam and connected to the multi-chamber vacuum system. These measures and preparations allowed to perform measurements during a 6-week campaign, while each day evacuating the connected optical cavity to a low base pressure by a second larger-sized getter positioned in a separate cell, functioning as a pump in the setup. Before starting the measurements tritiated gas was released into the optical cavity at a de-

9. PRECISION MEASUREMENT OF VIBRATIONAL QUANTA IN TRITIUM HYDRIDE (HT)

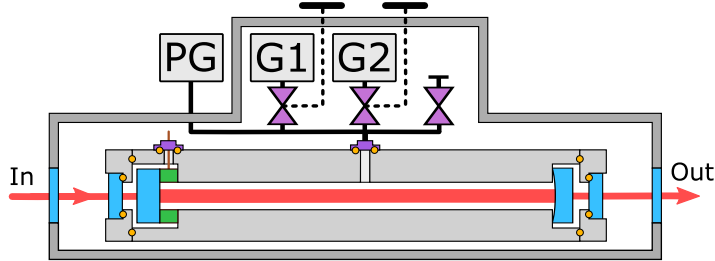


Figure 9.1: Schematic of the tritium-adapted setup: The optical cavity with two reflective mirrors, a piezo stack and two sealed optical windows, is fully metal-sealed using indium wire seals (orange). The assembly is inside a secondary vacuum for additional stability and safety. Getter G1 is the tritium source to acquire and store the tritium. Getter G2 serves as an additional backing pump for when the experiment is not active. The third valve enabled initial pump-down. PG: pressure gauge.

sired hydrogen pressure in the range 0.1-1.0 Pa by controlled heating of the first getter.

9.2.2 NICE-OHMS methodology

For the HT frequency metrology studies a diode laser (TOPTICA DL Pro) running in the range 1430-1520 nm is used. Signal detection of the saturation spectra is accomplished via the NICE-OHMS technique [43, 56, 58] using sideband modulation of the carrier wave, at frequency $f_c \pm f_m$ with $f_m = 405$ MHz, matching the free-spectral-range (FSR) of the cavity for generating the heterodyne NICE-OHMS signal. Feedback mechanisms were applied, locking the laser to the optical cavity for short-term stabilization, and locking the laser to a frequency comb for canceling long-term drift and frequency measurement [51, 145], as well as DeVoe-Brewer locking of the sidebands to the cavity [80]. The optical cavity of length 0.37 m is hemispherical with one curved mirror at a radius-of-curvature of 2 m, resulting in a collimated beam at a waist diameter of 1.2 mm. With reflectivities of $R = 99.996\%$ a cavity finesse of 80,000 is achieved for obtaining intracavity powers of 400 W.

Further noise reduction is accomplished via slow modulation of the cavity length (at 395 Hz) at varying peak-to-peak amplitudes of up to 100 kHz and lock-in detection and demodulation at the first derivative ($1f$). This $1f$ signal should result in a derivative of a dispersive

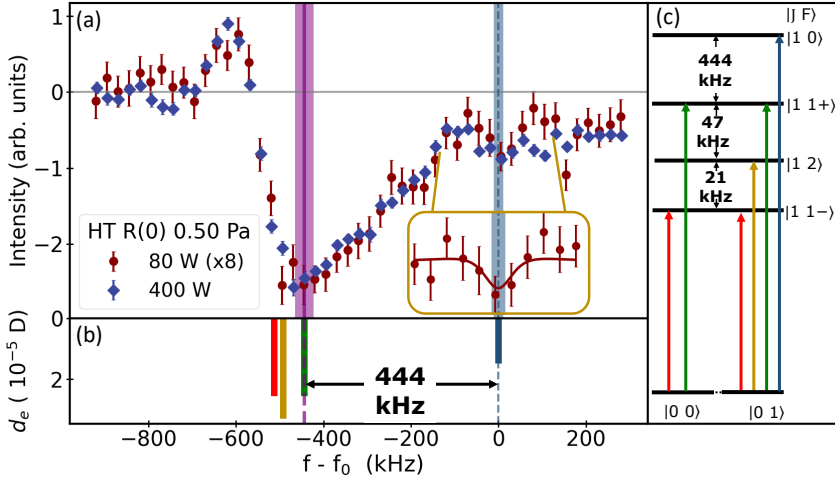


Figure 9.2: (a) Recorded spectra of the R(0) line at a total hydrogen pressure of 0.5 Pa (50% HT) for intracavity powers of 80 W and 400 W. The absolute frequency scale is given via $f_0 = 203\,396\,427\,135$ kHz. In the inset the single isolated hyperfine component is shown with a fit, the width of the blue bar representing the statistical uncertainty. The width of the purple bar, at the location of the purely rovibrational transition, represents the final uncertainty. (b) Hyperfine components as a stick spectrum (strength indicated by dipole moments d_e); (c) Level scheme of hyperfine components.

Lorentzian profile [172], hence in a symmetric line shape, as was found for saturation spectroscopy of water [154].

9.3 Results and discussion

9.3.1 Measurements of the R(0) and R(1) lines

Saturated absorption spectra were measured for two overtone rotational lines in the (2-0) band of HT. Typical recordings took some 12 hours of averaging. A first saturated absorption spectrum, recorded for the R(0) line, is presented in Fig. 9.2. The spectral structure consists of a broad dispersion-shaped resonance, reminiscent of the features observed in HD [50–52, 145, 161], and is associated with the overlapping features of 5 hyperfine components as color-coded in panels (b) and (c) of Fig. 9.2. In the computations by Jozwiak et al. [208] only the couplings between nuclear spin and rotation are included, yielding the hyperfine splittings

9. PRECISION MEASUREMENT OF VIBRATIONAL QUANTA IN TRITIUM HYDRIDE (HT)

Table 9.1: Results of the experimental transition frequencies of the purely rovibrational (hyperfineless) lines R(0) and R(1) in the (2-0) band of HT, and a comparison with results from a calculation in which the non-relativistic energy is computed via the direct non-adiabatic approach [205]. Differences are also presented in terms of the combined standard deviation (σ) of experiment and theory.

Line	Exp. (kHz)	Ref. [200] (MHz)	Diff. (MHz)	Diff. (σ)
R(0)	203 396 426 692 (21)	203 396 424.9 (9)	1.8 (1.1)	1.8
R(1)	205 380 033 644 (22)	205 380 031.7 (9)	1.8 (1.0)	1.8
P(1)	198 824 820 600 (100)	198 824 819.0 (9)	1.9 (1.1)	1.7

in $J = 0$ rotational levels, between $F = 0$ and $F = 1$ components, to be zero, while in refined calculations of the spin-spin interaction a splitting of 0.3 kHz is found for HT [211]. Unlike the case of HD there is a single isolated hyperfine component, for excitation to the $|10\rangle$ level, located at the positive side of the hyperfineless position by 444 kHz [208]. This component, observed as a symmetric narrow Lamb-dip in the spectrum measured at the lower power of 80 W, is fitted (see inset in Fig. 9.2; only the data points covering the isolated hyperfine component as displayed in the insets are included in the fit) to the expected line shape of a $1f$ -demodulated NICE-OHMS signal [172, 197]:

$$F(f)_{1f} = \frac{4A [\Gamma^2 - 4(f - f_0)^2]}{[\Gamma^2 + 4(f - f_0)^2]^2}, \quad (9.1)$$

delivering the line position f_0 of the isolated resonance and its width Γ . A second spectrum, of the R(1) line in the (2-0) band, is displayed in Fig. 9.3. Again, at the high-frequency side of a broad dispersion-shaped feature, an isolated Lamb dip component appears, specifically in the low-power recording (at 80 Watt intracavity). Its center position was determined from a fit to Eq. (9.1), again for the data displayed in the inset. For the R(1) line that component corresponds not to just one but to three hyperfine components.

The spectroscopic analysis of the HT overtone resonances depend on their favorable ordering of hyperfine components, exhibiting an isolated narrow feature, not found in HD [51, 145], where all hyperfine components are overlapped. The statistical uncertainty of the fit of the R(0) line amounts to 11 kHz, while that of the R(1) is 6 kHz, due to its better signal-to-noise ratio. No sign of asymmetry is found in the fitting procedures to the experimental data, strengthening the assumption that the isolated components represent absorption Lamb dips. The re-

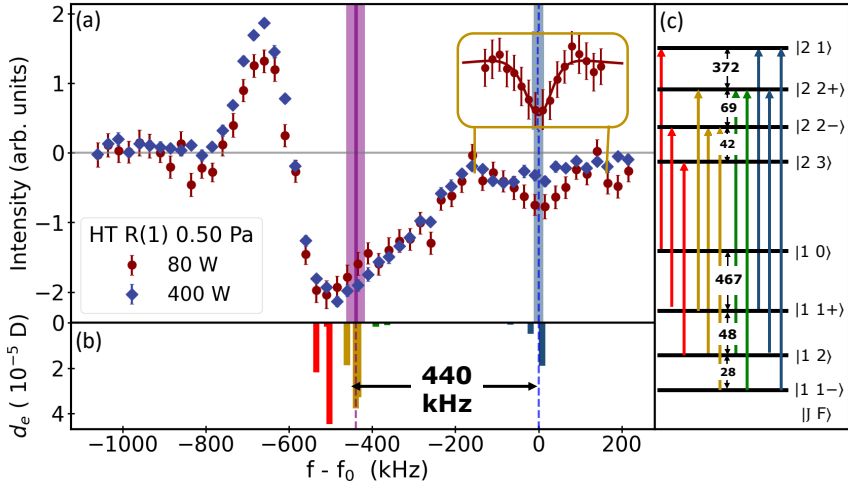


Figure 9.3: (a) Recorded spectra of the R(1) line at two different powers, with an isolated Lamb dip at the high frequency side covering three hyperfine components. The absolute frequency scale is given via $f_0 = 205\,380\,034\,083$ kHz, corresponding to the fitted center position of the isolated Lamb dip as shown in the inset. Its width (blue bar) represents the sum of the statistical uncertainty and the uncertainty contribution of the three components (see text). The purple bar represents the location and final uncertainty of the purely rovibrational transition frequency. (b) Hyperfine stick spectrum for this transition. (c) Level scheme of hyperfine components; the numbers in between levels denote the level splittings in units of kHz.

sulting values are transformed into frequencies of the hyperfineless or purely rovibrational transitions by including the shift of the isolated hyperfine component based on accurately computed values [208] as discussed above and illustrated in Figs. 9.2 and 9.3. Since for the R(1) line the isolated Lamb dip is composed of 3 overlapping hyperfine components a weighted average is taken, adding an uncertainty of 6 kHz. The saturated absorption spectra do not exhibit a first order Doppler effect, but are subject to a second order (relativistic) Doppler effect of $f_{2D} = h\nu_0^2 v^2 / 2mc^2$, which amounts to 1.4 kHz for HT at room temperature.

The overall pattern of the isolated components in the spectra show that the spectra overlap for the two pressure recordings. Quantitative analysis reveals that a pressure shift should be on the order of 5 kHz, and is conservatively estimated at 10 kHz, which is in agreement to pressure shifts found in HD (at 10 kHz/Pa) [51, 145] and in H₂ (at

15 kHz/Pa) [197]. Considering these systematic effects and contributions to the error budget final transition frequencies and uncertainties are determined and listed in Table 9.1.

9.3.2 Lamb peaks in P(1) spectrum

A spectrum of the P(1) line in HT was recorded as well at conditions as indicated in Fig. 9.4. Similar to the case of the P(1) line in HD [146] the saturated spectral components appear as Lamb peaks, rather than as Lamb dips. In the case of HD this phenomenon of reversed signal amplitudes was interpreted as originating from the contribution of crossover resonances, that were included in a comprehensive model based on optical Bloch equations [51]. An important learning from the present study is that this cannot be the case for HT, as crossovers cannot interfere with regular hyperfine components at the location of the isolated component. It must be concluded that the present finding contradicts an explanation based on crossover resonances for the signal inversion in HD [146]. We do not have an explanation for the phenomenon of signal inversion, neither in HT nor in HD, which adds to the conundrum of the dispersive-like line shapes of the strong saturation signals of the non-isolated hyperfine components in both isotopologues. Future studies may reveal whether these phenomena are related to optical pumping, collisional relaxation, or trapping effects of molecules in the nodes of intense standing waves in the cavity. In view of the fact that P(1) is not observed as a regular Lamb dip, we do not pursue extracting an accurate transition frequency via fitting. A rovibrational transition frequency is preliminary estimated at 198 824 820 600 kHz with a conservative uncertainty estimate of 100 kHz.

9.3.3 Recoil shift

A note must be made on the recoil effect on the measured transitions. As is known from the early days of laser spectroscopy in the saturation regime both a red and a blue shifted recoil component is observed [73, 75, 175] at frequencies $f_{\text{rec}} = \pm h\nu_0^2/2mc^2$. For the case of the R-lines of HT in the (2-0) band the recoil shift corresponds to ± 22 kHz. Recently, in the case of a measurement of a Lamb dip in the very weak quadrupole spectrum of H₂ [197] only a single recoil component was observed, which was interpreted as the blue recoil. In the present case of

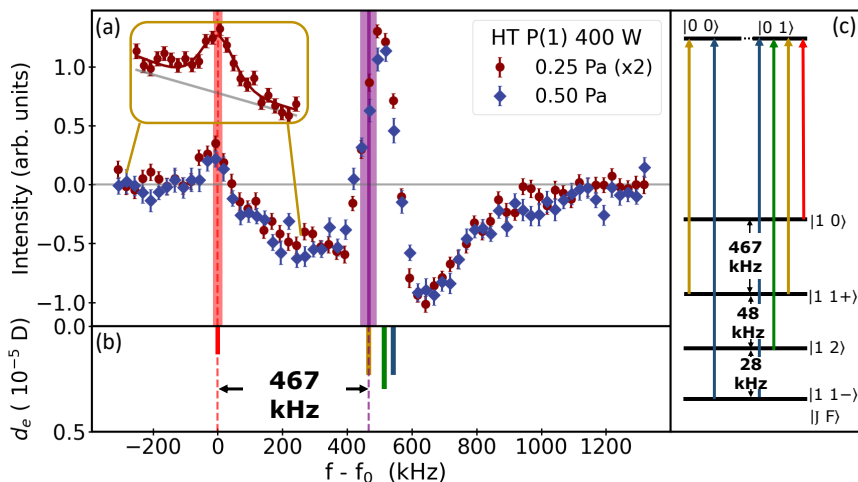


Figure 9.4: (a) Recorded saturated absorption spectra of the P(1) line in the (2-0) band of HT for an intracavity circulating power of 400 W and hydrogen pressures as indicated. The absolute frequency scale is given via $f_0 = 198\,824\,820\,185$ kHz. (b) Stick spectrum of hyperfine components. (c) Level scheme of hyperfine components.

HT the combination of widths and noise levels do not allow for a decision whether the observed spectra cover both recoil components or only one. Here we follow the generally accepted approach to the recoil phenomenon in saturation that the blue and red recoil components average out to no shift of the molecular resonance frequency. If the suppression of red recoil components in intracavity saturation spectroscopy of weak transitions is an ubiquitous feature, then the measured frequencies (as in Table 9.1), should be lowered by 22 kHz. For the moment this is left as an open issue.

9.3.4 Comparison with theory

The present experimental values for the transition frequencies in the (2-0) band come timely for a comparison with very recent calculations for the tritium bearing hydrogen isotopologues [205]. A recent calculation for based on a direct non-adiabatic approach (DNA, hence a four-particle variational [4, 5] involving nonadiabatic James-Coolidge wave functions led to an improvement by an order of magnitude, reaching 0.9 MHz for the overtone transitions in HT [205]. The DNA method

9. PRECISION MEASUREMENT OF VIBRATIONAL QUANTA IN TRITIUM HYDRIDE (HT)

was employed to compute non-relativistic energies at an accuracy of 10^{-13} , so exact for the purpose of comparison with present state-of-the-art experiments. The results from the DNA non-relativistic approach are augmented with computations of relativistic and quantum electrodynamical (QED) corrections [159], which produce the final theoretical uncertainties.

These data have been incorporated in the H2SPECTRE program, version 7.4 [200]. Results of the H2SPECTRE suit indicate that the uncertainty in the computation of level energies amounts to $1.4 \times 10^{-4} \text{ cm}^{-1}$ (or 4.2 MHz), but cancelation of uncertainty occurs when computing the transition frequencies yielding uncertainties of $3.1 \times 10^{-5} \text{ cm}^{-1}$ (or 0.9 MHz). H2SPECTRE also reveals the origin of the estimated uncertainty, which is in the $E^{(5)}$ or $m\alpha^5$ -term in the level energy expansion of the fine structure constant, the leading order QED correction. In Table 9.1 results from experiment and theory are compared for the lines measured in the present study.

The data in Table 9.1 show that the accuracy of the present experimental transition frequencies is among the highest in the hydrogen isotopologues, with those of HD [36] and H₂ [197]. Again, a systematic deviation is found between experiment and theory at the level of 1.8σ . Previously, deviations at exactly the same 1.8σ were found for the (2-0) vibrational bands in HD [36, 201], in H₂ [188, 197], and in D₂ [202]. This large set of data makes the deviations significant. Even for the more advanced treatment of the leading order QED term, that was recently recomputed [182], the discrepancies persist.

9.4 Conclusion

The present study exploits the favorable hyperfine structure in the tritium hydride species using an isolated hyperfine component in the R(0) and R(1) transitions in the (2-0) band to determine purely rovibrational transition frequencies at an accuracy of 20 kHz, a thousand times better than for any previously observed transition in a tritiated hydrogen molecule. It is shown that measurement campaigns of extended duration can be performed in a cavity-enhanced configuration without radioactive tritium degrading the highly reflective mirror coatings, nor having detrimental effects on the instrumentation. This opens the perspective of adding all three tritiated hydrogen molecules to the set of bench-

mark systems for testing molecular quantum theory and probing new physics [6]. With the recent computations of non-relativistic energies in the tritiated species [205], the current results of HT frequencies form an accurate test ground for future computations of the $m\alpha^5$ nonadiabatic QED term in molecular hydrogen isotopologues.

The research was funded via the Access Program of Laserlab-Europe (Grant Numbers 654148 and 871124), a European Union's Horizon 2020 research and innovation programme. Financial support from the Netherlands Organisation for Scientific Research (NWO), via the Program "The Mysterious Size of the Proton" is gratefully acknowledged. M. Schlösser wishes to thank the Baden-Württemberg Foundation for the generous support of this work within the Elite-Postdoc-Fellowship. We thank the KIT mechanical workshop for constructing the multiple chamber cell structure, the co-workers at TLK for supporting tritium activities (safety, legal, filling, advise), and the radiation safety officer at VUA (Ms. J. Houben-Weerts) for making this experiment possible.

Bibliography

- [1] Bohr, N. On the constitution of atoms and molecules. *Philos. Mag. Series 6* **26**, 1–15 (1913).
- [2] Piszczatowski, K. *et al.* Theoretical determination of the dissociation energy of molecular hydrogen. *J. Chem. Theory Comput.* **5**, 3039–3048 (2009).
- [3] Pachucki, K. & Komasa, J. Schrödinger equation solved for the hydrogen molecule with unprecedented accuracy. *J. Chem. Phys.* **144**, 164306 (2016).
- [4] Puchalski, M., Komasa, J., Czachorowski, P. & Pachucki, K. Nonadiabatic QED correction to the dissociation energy of the hydrogen molecule. *Phys. Rev. Lett.* **122**, 103003 (2019).
- [5] Puchalski, M., Komasa, J., Spyszkiewicz, A. & Pachucki, K. Dissociation energy of molecular hydrogen isotopologues. *Phys. Rev. A* **100**, 020503 (2019).
- [6] Ubachs, W., Koelemeij, J. C. J., Eikema, K. S. E. & Salumbides, E. J. Physics beyond the Standard Model from hydrogen spectroscopy. *J. Mol. Spectrosc.* **320**, 1 – 12 (2016).
- [7] Salumbides, E. J. *et al.* Bounds on fifth forces from precision measurements on molecules. *Phys. Rev. D* **87**, 112008 (2013).
- [8] Salumbides, E. J., Schellekens, A. N., Gato-Rivera, B. & Ubachs, W. Constraints on extra dimensions from precision molecular spectroscopy. *New J. Phys.* **17**, 033015 (2015).
- [9] Cheng, C.-F. *et al.* Dissociation energy of the hydrogen molecule at 10^{-9} accuracy. *Phys. Rev. Lett.* **121**, 013001 (2018).
- [10] Hölsch, N. *et al.* Benchmarking theory with an improved measurement of the ionization and dissociation energies of H_2 . *Phys. Rev. Lett.* **122**, 103002 (2019).

BIBLIOGRAPHY

- [11] Hussels, J. *et al.* Improved ionization and dissociation energies of the deuterium molecule. *Phys. Rev. A* **105**, 022820 (2022).
- [12] Hölsch, N. *et al.* Ionization and dissociation energies of HD and dipole-induced g/u -symmetry breaking. *Phys. Rev. A* **108**, 022811 (2023).
- [13] Langmuir, I. The dissociation of hydrogen into atoms.1. *J. Am. Chem. Soc.* **34**, 860–877 (1912).
- [14] Herzberg, G. Quadrupole rotation-vibration spectrum of the hydrogen molecule. *Nature* **163**, 170 (1949).
- [15] Herzberg, G. Forbidden transitions in diatomic molecules: I. the quadrupole rotation-vibration spectrum of H₂. *Can. J. Phys.* **28**, 144–152 (1950).
- [16] Jeppesen, C. R. Bands in the extreme ultraviolet emission spectrum of the H¹H² molecule. *Phys. Rev.* **45**, 480–484 (1934).
- [17] Urey, H. C., Brickwedde, F. G. & Murphy, G. M. A hydrogen isotope of mass 2. *Phys. Rev.* **39**, 164–165 (1932).
- [18] Herzberg, G. Rotation-vibration spectrum of the HD molecule. *Nature* **166**, 563 (1950).
- [19] Bragg, S. L., Smith, W. H. & Brault, J. W. Line positions and strengths in the H₂ quadrupole spectrum. *Astroph. J.* **263**, 999–1004 (1982).
- [20] Jennings, D. E., Weber, A. & Brault, J. W. FTS-raman flame spectroscopy of high- J lines in H₂ and D₂. *J. Mol. Spectr.* **126**, 19 (1987).
- [21] Durie, R. A. & Herzberg, G. Forbidden transitions in diatomic molecules: V. The rotation-vibration spectrum of the hydrogen-deuteride (HD) molecule. *Can. J. Phys.* **38**, 806–818 (1960).
- [22] McKellar, A. R. W. Intensities of dipole and quadrupole rotation-vibration spectra of HD. *Can. J. Phys.* **52**, 1144–1151 (1974).
- [23] Evenson, K. M. *et al.* Frequency measurement of the $J = 1 - 0$ rotational transition of HD. *Astrophys. J. Lett.* **330**, L135 (1988).
- [24] Ulivi, L., de Natale, P. & Inguscio, M. Pure rotational spectrum of hydrogen deuteride by far-infrared Fourier transform spectroscopy. *Astroph. J. Lett.* **378**, L29 (1991).
- [25] Hu, S.-M. *et al.* The $v = 3 - 0$ S(0)-S(3) electric quadrupole transitions of H₂ near 0.8 μm . *Astroph. J.* **749**, 76 (2012).
- [26] Cheng, C.-F. *et al.* Electric-quadrupole transition of H₂ determined to 10⁻⁹ precision. *Phys. Rev. A* **85**, 024501 (2012).

-
- [27] Kassi, S. & Campargue, A. Electric quadrupole transitions and collision-induced absorption in the region of the first overtone band of H₂ near 1.25 μm . *J. Mol. Spectr.* **300**, 55–59 (2014).
- [28] Kassi, S., Lauzin, C., Chaillot, J. & Campargue, A. The (2-0) R(0) and R(1) transition frequencies of HD determined to a 10^{-10} relative accuracy by Doppler spectroscopy at 80 K. *Phys. Chem. Chem. Phys.* **24**, 23164–23172 (2022).
- [29] Lamperti, M. *et al.* Stimulated Raman scattering metrology of molecular hydrogen. *Comm. Phys.* **6**, 67 (2023).
- [30] Kassi, S. & Campargue, A. Electric quadrupole and dipole transitions of the first overtone band of HD by CRDS between 1.45 and 1.33 μm . *J. Mol. Spectrosc.* **267**, 36–42 (2011).
- [31] Fasci, E. *et al.* Precision spectroscopy of HD at 1.38 μm . *Phys. Rev. A* **98**, 022516 (2018).
- [32] Kassi, S., Campargue, A., Pachucki, K. & Komasa, J. The absorption spectrum of D₂: Ultrasensitive cavity ring down spectroscopy of the (2-0) band near 1.7 μm and accurate ab initio line list up to 24 000 cm^{-1} . *J. Chem. Phys.* **136**, 184309 (2012).
- [33] Wcislo, P. *et al.* Accurate deuterium spectroscopy for fundamental studies. *J. Quant. Spectr. Rad. Transfer* **213**, 41–51 (2018).
- [34] Martínez, R. Z., Bermejo, D., Wcislo, P. & Thibault, F. Accurate wavenumber measurements for the S₀(0), S₀(1), and S₀(2) pure rotational Raman lines of D₂. *J. Raman Spectr.* **50**, 127–129 (2019).
- [35] Dickenson, G. D. *et al.* Fundamental vibration of molecular hydrogen. *Phys. Rev. Lett.* **110**, 193601 (2013).
- [36] Fast, A. & Meek, S. A. Sub-ppb measurement of a fundamental band rovibrational transition in HD. *Phys. Rev. Lett.* **125**, 023001 (2020).
- [37] Fast, A. & Meek, S. A. Precise measurement of the D₂ S₁(0) vibrational transition frequency. *Mol. Phys.* **120**, e1999520 (2022).
- [38] Trivikram, T. M., Schlösser, M., Ubachs, W. & Salumbides, E. J. Relativistic and QED effects in the fundamental vibration of T₂. *Phys. Rev. Lett.* **120**, 163002 (2018).
- [39] Lai, K.-F. *et al.* Precision tests of nonadiabatic perturbation theory with measurements on the DT molecule. *Phys. Rev. Res.* **1**, 033124 (2019).
- [40] Lai, K.-F. *et al.* Precision measurement of the fundamental vibrational frequencies of tritium-bearing hydrogen molecules: T₂, DT, HT. *Phys. Chem. Chem. Phys.* **22**, 8973–8987 (2020).

BIBLIOGRAPHY

- [41] Patra, S. *et al.* Proton-electron mass ratio from laser spectroscopy of HD^+ at the part-per-trillion level. *Science* **369**, 1238–1241 (2020).
- [42] Ye, J., Ma, L.-S. & Hall, J. Sub-Doppler optical frequency reference at $1.064\ \mu\text{m}$ by means of ultrasensitive cavity-enhanced frequency modulation spectroscopy of a C_2HD overtone transition. *Opt. Lett.* **21**, 1000–1002 (1996).
- [43] Ma, L.-S., Ye, J., Dubé, P. & Hall, J. Ultrasensitive frequency-modulation spectroscopy enhanced by a high-finesse optical cavity: theory and application to overtone transitions of C_2H_2 and C_2HD . *J. Opt. Soc. Amer. B* **16**, 2255–2268 (1999).
- [44] Ye, J., Ma, L.-S. & Hall, J. Ultrasensitive detections in atomic and molecular physics: demonstration in molecular-overtone spectroscopy. *J. Opt. Soc. Amer. B* **15**, 6–15 (1998).
- [45] O’Keefe, A. & Deacon, D. A. G. Cavity ring-down optical spectrometer for absorption measurements using pulsed laser sources. *Rev. Scient. Instrum.* **59**, 2544–2551 (1988).
- [46] Romanini, D., Kachanov, A., Sadeghi, N. & Stoeckel, F. CW cavity ring down spectroscopy. *Chem. Phys. Lett.* **264**, 316–322 (1997).
- [47] van Zee, R. & Looney, J. P. *Cavity Ring-Down Spectroscopy: Techniques and Applications* (Elsevier, 2002).
- [48] Berden, G. & Engeln, R. *Cavity Ring-Down Spectroscopy: Techniques and Applications* (Wiley, Blackwell Publishing, 2009).
- [49] Gagliardi, G. & Loock, H.-P. *Cavity-Enhanced Spectroscopy and Sensing* (Springer Berlin, Heidelberg, 2013).
- [50] Tao, L.-G. *et al.* Toward a Determination of the Proton-Electron Mass Ratio from the Lamb-Dip Measurement of HD. *Phys. Rev. Lett.* **120**, 153001 (2018).
- [51] Diouf, M. L., Cozijn, F. M. J., Darquié, B., Salumbides, E. J. & Ubachs, W. Lamb-dips and Lamb-peaks in the saturation spectrum of HD. *Opt. Lett.* **44**, 4733 (2019).
- [52] Hua, T.-P., Sun, Y. R. & Hu, S.-M. Dispersion-like lineshape observed in cavity-enhanced saturation spectroscopy of HD at $1.4\ \mu\text{m}$. *Opt. Lett.* **45**, 4863–4866 (2020).
- [53] Lv, Y.-N. *et al.* Fano-like resonance due to interference with distant transitions. *Phys. Rev. Lett.* **129**, 163201 (2022).

-
- [54] Long, D. A., Fleisher, A. J., Wójtcwicz, S. & Hodges, J. T. Quantum-noise-limited cavity ring-down spectroscopy. *Appl. Phys. B* **115**, 149–153 (2014).
- [55] Axner, O., Ma, W. & Foltynowicz, A. Sub-Doppler dispersion and noise-immune cavity-enhanced optical heterodyne molecular spectroscopy revised. *J. Opt. Soc. Am. B* **25**, 1166–1177 (2008).
- [56] Foltynowicz, A., Ma, W., Schmidt, F. & Axner, O. Doppler-broadened noise-immune cavity-enhanced optical heterodyne molecular spectrometry signals from optically saturated transitions under low pressure conditions. *J. Opt. Soc. Am. B* **25**, 1156–1165 (2008).
- [57] Foltynowicz, A., Ma, W., Schmidt, F. & Axner, O. Wavelength-modulated noise-immune cavity-enhanced optical heterodyne molecular spectroscopy signal line shapes in the Doppler limit. *J. Opt. Soc. Amer. B* **26**, 1384–1394 (2009).
- [58] Axner, O., Ehlers, P., Foltynowicz, A., Silander, I. & Wang, J. *NICE-OHMS-Frequency Modulation Cavity-Enhanced Spectroscopy—Principles and Performance*, chap. 6, 211–251. Springer Series in Optical Sciences (Springer, 2014).
- [59] Ehlers, P., Junyang, J., Silander, I. & Axner, O. Doppler broadened NICE-OHMS beyond the triplet formalism: assessment of optimum modulation index. *J. Opt. Soc. Amer. B* **31**, 1499–1507 (2014).
- [60] Schmidt, F., Foltynowicz, A., Ma, W., Lock, T. & Axner, O. Doppler-broadened fiber-laser-based NICE-OHMS – Improved detectability. *Opt. Express* **15**, 10822–10831 (2007).
- [61] Ehlers, P., Silander, I., Wang, J. & Axner, O. Fiber-laser-based noise-immune cavity-enhanced optical heterodyne molecular spectrometry instrumentation for Doppler-broadened detection in the $10^{-12} \text{ cm}^{-1} \text{ Hz}^{-1/2}$ region. *J. Opt. Soc. Amer. B* **29**, 1305–1315 (2012).
- [62] Ehlers, P., Silander, I., Foltynowicz, A. & Axner, O. Fiber-laser-based noise-immune cavity-enhanced optical heterodyne molecular spectrometry incorporating an optical circulator. *Opt. Lett.* **39**, 279–282 (2014).
- [63] Foltynowicz, A., Schmidt, F., Ma, W. & Axner, O. Noise-immune cavity-enhanced optical heterodyne molecular spectroscopy: Current status and future potential. *Appl. Phys. B* **92**, 313–326 (2008).
- [64] Centeno, R., Mandon, J., Cristescu, S., Axner, O. & Harren, F. J. M. External cavity diode laser-based detection of trace gases with NICE-OHMS using current modulation. *Opt. Express* **23**, 6277–6282 (2015).

BIBLIOGRAPHY

- [65] Markus, C. *et al.* High precision rovibrational spectroscopy of OH⁺. *Astroph. J.* **817**, 138–142 (2016).
- [66] Markus, C., Perry, A., Hodges, J. & McCall, B. Improving cavity-enhanced spectroscopy of molecular ions in the mid-infrared with up-conversion detection and Brewster-plate spoilers. *Opt. Express* **25**, 3709–3721 (2017).
- [67] Schäffer, S. A. *et al.* Towards passive and active laser stabilization using cavity-enhanced atomic interaction. *Journal of Physics: Conference Series* **810**, 012002 (2017).
- [68] Dinesan, H., Fasci, E., Castrillo, A. & Gianfrani, L. Absolute frequency stabilization of an extended-cavity diode laser by means of noise-immune cavity-enhanced optical heterodyne molecular spectroscopy. *Opt. Lett.* **39**, 2198–2201 (2014).
- [69] Christensen, B. T. R. *et al.* Nonlinear spectroscopy of Sr atoms in an optical cavity for laser stabilization. *Phys. Rev. A* **92**, 053820 (2015).
- [70] Saraf, S., Berceau, P., Stochino, A., Byer, R. & Lipa, J. Ultrastable frequency reference at 1.56 μm using a ¹²C¹⁶O molecular overtone transition with the noise-immune cavity-enhanced optical heterodyne molecular spectroscopy method. *Opt. Lett.* **41**, 2189–2192 (2016).
- [71] Zhou, Y. *et al.* Laser frequency stabilization based on a universal sub-Doppler NICE-OHMS instrumentation for the potential application in atmospheric lidar. *Atmos. Measur. Tech.* **12**, 1807–1814 (2019).
- [72] Bjorklund, G. C. Frequency-modulation spectroscopy: a new method for measuring weak absorptions and dispersions. *Opt. Lett.* **5**, 15–17 (1980).
- [73] Hall, J. L., Bordé, C. J. & Uehara, K. Direct optical resolution of the recoil effect using saturated absorption spectroscopy. *Phys. Rev. Lett.* **37**, 1339–1342 (1976).
- [74] Bagayev, S. N., Baklanov, A. E., Chebotayev, V. P. & Dychkov, A. S. Superhigh resolution spectroscopy in methane with cold molecules. *Appl. Phys. B* **48**, 31 (1989).
- [75] Bagayev, S. N. *et al.* Second-order Doppler-free spectroscopy. *Appl. Phys. B* **52**, 63 (1991).
- [76] Demtröder, W. *Laser Spectroscopy, 4th Edition* (Springer, 2008).
- [77] Bordé, C. J., Hall, J. L., Kunasz, C. V. & Hummer, D. G. Saturated absorption line shape: Calculation of the transit-time broadening by a perturbation approach. *Phys. Rev. A* **14**, 236–263 (1976).

-
- [78] Letokhov, V. S. & Chebotayev, V. P. *Nonlinear Laser Spectroscopy, Springer Series in optical sciences, Vol. 4* (Springer Verlag, 1977).
- [79] Melosso, M. *et al.* Hyperfine-resolved near-infrared spectra of H₂¹⁷O. *J. Phys. Chem. A* **125**, 7884–7890 (2021).
- [80] DeVoe, R. G. & Brewer, R. G. Laser-frequency division and stabilization. *Phys. Rev. A* **30**, 2827–2829 (1984).
- [81] Silander, I., Ehlers, P., Wang, J. & Axner, O. Frequency modulation background signals from fiber-based electro optic modulators are caused by crosstalk. *J. Opt. Soc. Am. B* **29**, 916–923 (2012).
- [82] Li, Z., Ma, W., Yang, W., Wang, Y. & Zheng, Y. Reduction of zero baseline drift of the Pound–Drever–Hall error signal with a wedged electro-optical crystal for squeezed state generation. *Opt. Lett.* **41**, 3331–3334 (2016).
- [83] Zhang, W. *et al.* Reduction of residual amplitude modulation to 1×10^{-6} for frequency modulation and laser stabilization. *Opt. Lett.* **39**, 1980–1983 (2014).
- [84] Werle, P. Accuracy and precision of laser spectrometers for trace gas sensing in the presence of optical fringes and atmospheric turbulence. *Appl. Phys. B* **102**, 313–329 (2011).
- [85] Whittaker, E. A., Gehrtz, M. & Bjorklund, G. C. Residual amplitude modulation in laser electro-optic phase modulation. *J. Opt. Soc. Am. B* **2**, 1320–1326 (1985).
- [86] Ehlers, P. *Further development of NICE-OHMS – an ultra-sensitive frequency-modulated cavity-enhanced laser-based spectroscopic technique for detection of molecules in gas phase*. Ph.D. thesis, Umeå University, Umeå, Sweden (2014).
- [87] Xiong, B., Du, Z. & Li, J. Modulation index optimization for optical fringe suppression in wavelength modulation spectroscopy. *Rev. Scient. Instrum.* **86**, 113104 (2015).
- [88] Zhao, G., Hausmaninger, T., Ma, W. & Axner, O. Whispering-gallery-mode laser-based noise-immune cavity-enhanced optical heterodyne molecular spectrometry. *Opt. Lett.* **32**, 3109–3112 (2017).
- [89] Hua, T.-P. *et al.* Cavity-enhanced saturation spectroscopy of molecules with sub-kHz accuracy. *Chin. J. Chem. Phys.* **32**, 107–112 (2019).
- [90] Schmidt, F., Foltynowicz, A., Ma, W., Lock, T. & Axner, O. Highly sensitive dispersion spectroscopy by probing the free spectral range of an optical cavity using dual-frequency modulation. *Appl. Phys. B* **101**, 497–509 (2010).

BIBLIOGRAPHY

- [91] Wu, H. *et al.* Comb-locked cavity ring-down spectroscopy with variable temperature. *Opt. Express* **27**, 37559–37567 (2019).
- [92] Santamaria, L. *et al.* Infrared comb spectroscopy of buffer-gas-cooled molecules: Toward absolute frequency metrology of cold acetylene. *Intern. J. Mol. Sciences* **22** (2021).
- [93] Chen, L. *et al.* Vibration-induced elastic deformation of Fabry-Perot cavities. *Phys. Rev. A* **74**, 053801 (2006).
- [94] Nazarova, T., Riehle, F. & Sterr, U. Vibration-insensitive reference cavity for an ultra-narrow-linewidth laser. *Appl. Phys. B* **83**, 531–536 (2006).
- [95] Ludlow, A. D. *et al.* Compact, thermal-noise-limited optical cavity for diode laser stabilization at 1×10^{-15} . *Opt. Lett.* **32**, 641–643 (2007).
- [96] Alnis, J., Matveev, A., Kolachevsky, N., Udem, T. & Hänsch, T. W. Subhertz linewidth diode lasers by stabilization to vibrationally and thermally compensated ultralow-expansion glass Fabry-Pérot cavities. *Phys. Rev. A* **77**, 053809 (2008).
- [97] Kessler, T. *et al.* A sub-40-mHz-linewidth laser based on a silicon single-crystal optical cavity. *Nature Photon.* **6**, 687 – 692 (2012).
- [98] Zhang, W. *et al.* Ultrastable silicon cavity in a continuously operating closed-cycle cryostat at 4 K. *Phys. Rev. Lett.* **119**, 243601 (2017).
- [99] Kogelnik, H. & Li, T. Laser beams and resonators. *Appl. Opt.* **5**, 1550–1567 (1966).
- [100] Hecht, E. *Optics, 4th Edition* (Addison-Wesley, 2002).
- [101] Silander, I., Hausmaninger, T., Ma, W., Harren, F. & Axner, O. Doppler-broadened mid-infrared noise-immune cavity-enhanced optical heterodyne molecular spectrometry based on an optical parametric oscillator for trace gas detection. *Opt. Lett.* **40**, 439–442 (2015).
- [102] Huang, H. & Lehmann, K. Noise in cavity ring-down spectroscopy caused by transverse mode coupling. *Opt. Express* **15**, 8745–8759 (2007).
- [103] Robinson, J. M. *et al.* Crystalline optical cavity at 4 K with thermal-noise-limited instability and ultralow drift. *Optica* **6**, 240–243 (2019).
- [104] Ekin, J. *Experimental Techniques for Low-Temperature Measurements: Cryostat Design, Material Properties and Superconductor Critical-Current Testing* (Oxford University Press, 2006).
- [105] Möhle, K. *Piezoelectrically Tunable Optical Cavities for the Gravitational Wave Detector LISA*. Ph.D. thesis, Humboldt-Universität, Berlin, Germany (2006).

-
- [106] See website manufacturer: <https://www.piceramic.com/en/expertise/piezo-technology/properties-piezo-actuators/temperature-dependence>.
- [107] Webster, S. A., Oxborrow, M. & Gill, P. Vibration insensitive optical cavity. *Phys. Rev. A* **75**, 011801 (2007).
- [108] Williams, D. C. The parallelism of a length bar with an end load. *J. Scient. Instrum.* **39**, 608 (1962).
- [109] Duckworth, R. C., Demko, J. A., Gouge, M. J. & Urbahn, J. A. Measurement of the emissivity of clean and contaminated silver plated copper surfaces at cryogenic temperatures. *AIP Conf. Proc.* **824**, 61–68 (2006).
- [110] Puchalski, M., Komasa, J., Czachorowski, P. & Pachucki, K. Complete α^6m corrections to the ground state of H_2 . *Phys. Rev. Lett.* **117**, 263002 (2016).
- [111] Liu, J. *et al.* Determination of the ionization and dissociation energies of the hydrogen molecule. *J. Chem. Phys.* **130**, 174306 (2009).
- [112] Sprecher, D., Jungen, C., Ubachs, W. & Merkt, F. Towards measuring the ionisation and dissociation energies of molecular hydrogen with sub-MHz accuracy. *Farad. Discuss.* **150**, 51–70 (2011).
- [113] Tan, Y. *et al.* Cavity ring-down spectroscopy of the electric quadrupole transitions of H_2 in the 784 - 852 nm region. *J. Mol. Spectr.* **300**, 60–64 (2014).
- [114] Maddaloni, P. *et al.* Absolute measurement of the S(0) and S(1) lines in the electric quadrupole fundamental band of D_2 around 3 μm . *J. Chem. Phys.* **133**, 154317 (2010).
- [115] Mondelain, D. *et al.* Sub-MHz accuracy measurement of the S(2) 2-0 transition frequency of D_2 by comb-assisted cavity ring down spectroscopy. *J. Mol. Spectr.* **326**, 5 – 8 (2016).
- [116] Bubin, S., Leonarski, F., Stanke, M. & Adamowicz, L. Charge asymmetry in pure vibrational states of the HD molecule. *J. Chem. Phys.* **130**, 124120 (2009).
- [117] Pachucki, K. & Komasa, J. Electric dipole rovibrational transitions in the HD molecule. *Phys. Rev. A* **78**, 052503 (2008).
- [118] McKellar, A. R. W. Intensities and the Fano line shape in the infrared spectrum of HD. *Can. J. Phys.* **51**, 389–397 (1973).
- [119] Weisłó, P., Gordon, I. E., Cheng, C.-F., Hu, S.-M. & Ciuryłó, R. Collision-induced line-shape effects limiting the accuracy in Doppler-limited spectroscopy of H_2 . *Phys. Rev. A* **93**, 022501 (2016).

- [120] Pachucki, K. & Komasa, J. Rovibrational levels of HD. *Phys. Chem. Chem. Phys.* **12**, 9188–9196 (2010).
- [121] Foltynowicz, A., Silander, I. & Axner, O. Reduction of background signals in fiber-based NICE-OHMS. *J. Opt. Soc. Am. B* **28**, 2797–2805 (2011).
- [122] Dinesan, H., Fasci, E., d’Addio, A., Castrillo, A. & Gianfrani, L. Characterization of the frequency stability of an optical frequency standard at 1.39 μm based upon noise-immune cavity-enhanced optical heterodyne molecular spectroscopy. *Opt. Express* **23**, 1757–1766 (2015).
- [123] Drever, R. W. P. *et al.* Laser phase and frequency stabilization using an optical resonator. *Appl. Phys. B* **31**, 97–105 (1983).
- [124] Dupré, P. Sub-Doppler noise-immune cavity-enhanced optical heterodyne molecular spectrometry modeling: from Doppler broadening to cross-sideband resonances. *J. Opt. Soc. Amer. B* **32**, 838–860 (2015).
- [125] Dupré, P. Dipole saturated absorption modeling in gas phase: Dealing with a gaussian beam. *J. Quant. Spectrosc. Rad. Transfer* **205**, 196 – 212 (2018).
- [126] Bagaev, S. N., Vasilenko, L. S., Dmitriev, A. K., Skvortsov, M. N. & Chebotaev, V. P. Narrowing of nonlinear resonances in low-pressure gases. *JETP Lett.* **23**, 360–363 (1976).
- [127] Bagaev, S. N., Baklanov, A. E., Dychkov, A. S., Pokasov, P. V. & Chebotaev, V. P. Ultrahigh resolution laser spectroscopy with cold particles. *JETP Lett.* **45**, 471–475 (1987).
- [128] Ramsey, N. F. & Lewis, H. R. Theory of hydrogen deuteride in magnetic fields. *Phys. Rev.* **108**, 1246–1250 (1957).
- [129] Code, R. F. & Ramsey, N. F. Molecular-beam magnetic resonance studies of HD and D₂. *Phys. Rev. A* **4**, 1945–1959 (1971).
- [130] J. Gauss (private communication).
- [131] Giusfredi, G. *et al.* Saturated-absorption cavity ring-down spectroscopy. *Phys. Rev. Lett.* **104**, 110801 (2010).
- [132] Pachucki, K. & Komasa, J. Accurate adiabatic correction in the hydrogen molecule. *J. Chem. Phys.* **141**, 224103 (2014).
- [133] Puchalski, M., Komasa, J. & Pachucki, K. Relativistic corrections for the ground electronic state of molecular hydrogen. *Phys. Rev. A* **95**, 052506 (2017).
- [134] Beyer, A. *et al.* The Rydberg constant and proton size from atomic hydrogen. *Science* **358**, 79–85 (2017).

-
- [135] Pohl, R. *et al.* The size of the proton. *Nature* **466**, 213–216 (2010).
- [136] Biesheuvel, J. *et al.* Probing QED and fundamental constants through laser spectroscopy of vibrational transitions in HD⁺. *Nat. Comm.* **7**, 10385 (2016).
- [137] Urey, H. C. & Teal, G. K. The hydrogen isotope of atomic weight two. *Rev. Mod. Phys.* **7**, 34–94 (1935).
- [138] de Lange, A., Reinhold, E. & Ubachs, W. Phenomena of g-u symmetry-breakdown in HD. *Intern. Rev. Phys. Chem.* **21**, 257–275 (2002).
- [139] Wick, G. C. Oscillation and rotation spectrum of the molecule HD. *Atti Reale Accad. Nazionale Lincei* **21**, 708–714 (1935).
- [140] Rich, N., Johns, J. & McKellar, A. Frequency and intensity measurements in the fundamental infrared band of HD. *J. Molec. Spectr.* **95**, 432–438 (1982).
- [141] Vasilchenko, S. *et al.* The HD spectrum near 2.3 μm by CRDS-VECSEL: Electric quadrupole transition and collision-induced absorption. *J. Mol. Spectrosc.* **326**, 9–16 (2016).
- [142] Trefler, M. & Gush, H. P. Electric dipole moment of HD. *Phys. Rev. Lett.* **20**, 703–705 (1968).
- [143] Essenwanger, P. & Gush, H. P. Rotational spectrum of HD at low pressures. *Can. J. Phys.* **62**, 1680–1685 (1984).
- [144] Drouin, B. J., Yu, S., Pearson, J. C. & Gupta, H. Terahertz spectroscopy for space applications: 2.5–2.7 THz spectra of HD, H₂O and NH₃. *J. Mol. Struct.* **1006**, 2–12 (2011).
- [145] Cozijn, F. M. J., Dupré, P., Salumbides, E. J., Eikema, K. S. E. & Ubachs, W. Sub-Doppler frequency metrology in HD for tests of fundamental physics. *Phys. Rev. Lett.* **120**, 153002 (2018).
- [146] Diouf, M. L., Cozijn, F. M. J., Lai, K.-F., Salumbides, E. J. & Ubachs, W. Lamb-peak spectrum of the HD (2-0) P(1) line. *Phys. Rev. Research* **2**, 023209 (2020).
- [147] Niu, M. L., Salumbides, E. J., Dickenson, G. D., Eikema, K. S. E. & Ubachs, W. Precision spectroscopy of the $X^1\Sigma_g^+, v = 0 \rightarrow 1$ ($J = 0 - 2$) rovibrational splittings in H₂, HD and D₂. *J. Mol. Spectr.* **300**, 44–54 (2014).
- [148] Castrillo, A., Fasci, E. & Gianfrani, L. Doppler-limited precision spectroscopy of HD at 1.4 μm : An improved determination of the R(1) center frequency. *Phys. Rev. A* **103**, 022828 (2021).

BIBLIOGRAPHY

- [149] Castrillo, A., Fasci, E. & Gianfrani, L. Erratum: Doppler-limited precision spectroscopy of HD at 1.4 μm : An improved determination of the $R(1)$ center frequency [Phys. Rev. A 103, 022828 (2021)]. *Phys. Rev. A* **103**, 069902 (2021).
- [150] Ledbetter, M. P., Romalis, M. V. & Kimball, D. F. J. Constraints on short-range spin-dependent interactions from scalar spin-spin coupling in deuterated molecular hydrogen. *Phys. Rev. Lett.* **110**, 040402 (2013).
- [151] Czachorowski, P., Puchalski, M., Komasa, J. & Pachucki, K. Nonadiabatic relativistic correction in H_2 , D_2 , and HD. *Phys. Rev. A* **98**, 052506 (2018).
- [152] Puchalski, M., Spyszkievicz, A., Komasa, J. & Pachucki, K. Nonadiabatic relativistic correction to the dissociation energy of H_2 , D_2 , and HD. *Phys. Rev. Lett.* **121**, 073001 (2018).
- [153] H2SPECTRE ver 7.3 Fortran source code, University of Warsaw, Poland (2020).
- [154] Tobias, R. *et al.* Spectroscopic-network-assisted precision spectroscopy and its application to water. *Nature Comm.* **11**, 1709 (2020).
- [155] Rabiner, L. R. & Gold, B. *Theory and Application of Digital Signal Processing* (Prentice-Hall, 1975).
- [156] Hall, C. A. & Meyer, W. Optimal error bounds for cubic spline interpolation. *J. Approx. Theory* **16**, 105–122 (1976).
- [157] Jóźwiak, H., Cybulski, H. & Wcisło, P. Positions and intensities of hyperfine components of all rovibrational dipole lines in the HD molecule. *J. Quant. Spectr. Rad. Transfer* **253**, 107171 (2020).
- [158] Pachucki, K. private communication.
- [159] Komasa, J., Puchalski, M., Czachorowski, P., Lach, G. & Pachucki, K. Rovibrational energy levels of the hydrogen molecule through nonadiabatic perturbation theory. *Phys. Rev. A* **100**, 032519 (2019).
- [160] Sprecher, D., Liu, J., Jungen, C., Ubachs, W. & Merkt, F. Communication: The ionization and dissociation energies of HD. *J. Chem. Phys.* **133**, 111102 (2010).
- [161] Cozijn, F. M. J. *et al.* Rotational level spacings in HD from vibrational saturation spectroscopy. *Phys. Rev. A* **105**, 062823 (2022).
- [162] F. M. J. Cozijn *et al.*, to be published; see Chapter 2.
- [163] Bielska, K. *et al.* Frequency-based dispersion Lamb-dip spectroscopy in a high finesse optical cavity. *Opt. Express* **29**, 39449–39460 (2021).

-
- [164] Tan, Y. *et al.* Cavity-enhanced saturated absorption spectroscopy of the (30012) - (00001) band of $^{12}\text{C}^{16}\text{O}_2$. *J. Chem. Phys.* **156**, 044201 (2022).
- [165] Puchalski, M., Komasa, J. & Pachucki, K. Hyperfine structure of the first rotational level in H_2 , D_2 and HD molecules and the deuteron quadrupole moment. *Phys. Rev. Lett.* **125**, 253001 (2020).
- [166] S.-M. Hu, Precise lineshape parameters from Doppler-free spectroscopy at low pressures, 25th International Conference on Spectral Line Shapes, Caserta, Italy, 19-24 June (2022).
- [167] Perevalov, B., Perevalov, V. & Campargue, A. A (nearly) complete experimental linelist for $^{13}\text{C}^{16}\text{O}_2$, $^{16}\text{O}^{13}\text{C}^{18}\text{O}$, $^{16}\text{O}^{13}\text{C}^{17}\text{O}$, $^{13}\text{C}^{18}\text{O}_2$ and $^{17}\text{O}^{13}\text{C}^{18}\text{O}$ by high-sensitivity CW-CRDS spectroscopy between 5851 and 7045 cm^{-1} . *J. Quant. Spectr. Rad. Transfer* **109**, 2437–2462 (2008).
- [168] Heitler, W. & London, F. Wechselwirkung neutraler atome und homopolare bindung nach der quantenmechanik. *Zeitschr. f. Phys.* **44**, 455–472 (1927).
- [169] Liu, Q.-H., Lv, Y.-N., Zou, C.-L., Cheng, C.-F. & Hu, S.-M. Saturated absorption spectroscopy of HD at 76 K. *Phys. Rev. A* **106**, 062805 (2022).
- [170] Pachucki, K. & Komasa, J. Magnetic dipole transitions in the hydrogen molecule. *Phys. Rev. A* **83**, 032501 (2011).
- [171] Diouf, M. L. *et al.* Ultraprecise relative energies in the (2 0 0) vibrational band of H_2^{16}O . *Mol. Phys.* **120**, e2050430 (2022).
- [172] Foltynowicz, A. *Fiber-laser-based Noise-Immune Cavity-Enhanced Optical Heterodyne Molecular Spectrometry*. Ph.D. thesis, Umeå University, Umeå, Sweden (2009).
- [173] Shimoda, K. *Introduction to Laser Physics, Springer Series in optical physics, Vol. 44* (Springer Verlag, 2008).
- [174] Kol’chenko, A. P., Rautian, S. G. & Sokolovskii, R. I. Interaction of an atom with a strong electromagnetic field with the recoil effect taken into consideration. *Sov. Phys. JETP* **28**, 986–990 (1969).
- [175] Barger, R. L., Bergquist, J. C., English, T. C. & Glaze, D. J. Resolution of photon-recoil structure of the 6573-Å calcium line in an atomic beam with optical Ramsey fringes. *Appl. Phys. Lett.* **34**, 850–852 (1979).
- [176] Riehle, F., Ishikawa, J. & Helmcke, J. Suppression of a recoil component in nonlinear Doppler-free spectroscopy. *Phys. Rev. Lett.* **61**, 2092–2095 (1988).

BIBLIOGRAPHY

- [177] Kurosu, T. & Morinaga, A. Suppression of the high-frequency recoil component in optical Ramsey-fringe spectroscopy. *Phys. Rev. A* **45**, 4799–4802 (1992).
- [178] Oates, C. W., Wilpers, G. & Hollberg, L. Observation of large atomic-recoil-induced asymmetries in cold atom spectroscopy. *Phys. Rev. A* **71**, 023404 (2005).
- [179] Alekseev, V. A. *et al.* Observation of the recoil effect in saturated dispersion resonances in methane. *Sov. J. Quant. Electr.* **14**, 441 (1984).
- [180] Józwiak, H. & Wcisło, P. Magic wavelength for a rovibrational transition in molecular hydrogen. *Sci. Rep.* **12**, 14529 (2022).
- [181] H2SPECTRE ver 7.4 Fortran source code, University of Warsaw, Poland (2022).
- [182] Siłkowski, M., Pachucki, K., Komasa, J. & Puchalski, M. Leading-order QED effects in the ground electronic state of molecular hydrogen. *Phys. Rev. A* **107**, 032807 (2023).
- [183] Black, J. H. & Dalgarno, A. Interstellar H₂ - The population of excited rotational states and the infrared response to ultraviolet radiation. *Astroph. J.* **203**, 132–142 (1976).
- [184] Farkas, A. *Orthohydrogen, Parahydrogen and Heavy Hydrogen* (Cambridge University Press, 1935).
- [185] Kolsky, H. G., Phipps, T. E., Ramsey, N. F. & Silsbee, H. B. Radiofrequency spectrum of H₂ in a magnetic field. *Phys. Rev.* **79**, 883–884 (1950).
- [186] Kolsky, H. G., Phipps, T. E., Ramsey, N. F. & Silsbee, H. B. Nuclear radiofrequency spectra of H₂ and D₂ in high and low magnetic fields. *Phys. Rev.* **87**, 395–403 (1952).
- [187] Harrick, N. J. & Ramsey, N. F. Rotational magnetic moment, magnetic susceptibilities, and electron distribution in the hydrogen molecule. *Phys. Rev.* **88**, 228–232 (1952).
- [188] Fleurbaey, H., Koroleva, A. O., Kassi, S. & Campargue, A. The high-accuracy spectroscopy of H₂ rovibrational transitions in the (2-0) band near 1.2 μm . *Phys. Chem. Chem. Phys.* **25**, 14749–14756 (2023).
- [189] Dabrowski, I. The Lyman and Werner bands of H₂. *Can. J. Phys.* **62**, 1639–1664 (1984).

-
- [190] Ubachs, W. & Reinhold, E. Highly accurate H₂ Lyman and Werner band laboratory measurements and an improved constraint on a cosmological variation of the proton-to-electron mass ratio. *Phys. Rev. Lett.* **92**, 101302 (2004).
- [191] Bailly, D., Salumbides, E., Vervloet, M. & Ubachs, W. Accurate level energies in the EF¹Σ_g⁺, GK¹Σ_g⁺, H¹Σ_g⁺, B¹Σ_u⁺, C¹Π_u, B¹Σ_u⁺, D¹Π_u, I¹Π_g, J¹Δ_g states of H₂. *Mol. Phys.* **108**, 827–846 (2010).
- [192] Brooks, P. R., Lichten, W. & Reno, R. Metastable hydrogen molecules. III. Hyperfine structure of orthohydrogen. *Phys. Rev. A* **4**, 2217–2223 (1971).
- [193] Freund, R. S. & Miller, T. A. Fermi-contact hyperfine interaction and the electron spin g-factor in H₂ d(3p) ³Π_u. *J. Chem. Phys.* **59**, 5770–5776 (2003).
- [194] Miller, T. A., Freund, R. S. & Zegarski, B. R. Fine and hyperfine structure of ortho-H₂, k(4p) ³Π_u. *J. Chem. Phys.* **60**, 3195–3202 (1974).
- [195] Ottinger, C., Rox, T. & Sharma, A. Laser spectroscopy of the H₂ (n = 3 Triplet Gerade) complex: Fine and hyperfine structure of the levels in ortho-H₂. *J. Mol. Spectr.* **163**, 414–427 (1994).
- [196] Osterwalder, A., Wüest, A., Merkt, F. & Jungen, C. High-resolution millimeter wave spectroscopy and multichannel quantum defect theory of the hyperfine structure in high Rydberg states of molecular hydrogen H₂. *J. Chem. Phys.* **121**, 11810–11838 (2004).
- [197] Cozijn, F. M. J., Diouf, M. L. & Ubachs, W. Lamb dip of a quadrupole transition in H₂. *Phys. Rev. Lett.* **131**, 073001 (2023).
- [198] Józwiak, H., Cybulski, H. & Wcisło, P. Hyperfine components of all rovibrational quadrupole transitions in the H₂ and D₂ molecules. *J. Quant. Spectr. Rad. Transfer* **253**, 107186 (2020).
- [199] Józwiak, H. & Wcisło, P. Relative intensities of hyperfine components of rovibrational transitions in molecular hydrogen. *Phys. Rev. A* **105**, 062812 (2022).
- [200] H2SPECTRE ver 7.4 Fortran source code, University of Warsaw, Poland (2022).
- [201] Cozijn, F. M. J., Diouf, M. L. & Ubachs, W. Saturation spectroscopy of R(0), R(2) and P(2) lines in the (2-0) band of HD. *Eur. J. Phys. D* **76**, 220 (2022).
- [202] Zaborowski, M. *et al.* Ultrahigh finesse cavity-enhanced spectroscopy for accurate tests of quantum electrodynamics for molecules. *Opt. Lett.* **45**, 1603–1606 (2020).

BIBLIOGRAPHY

- [203] Simmen, B., Mátyus, E. & Reiher, M. Elimination of the translational kinetic energy contamination in pre-Born–Oppenheimer calculations. *Mol. Phys.* **111**, 2086–2092 (2013).
- [204] Wang, L. M. & Yan, Z.-C. Relativistic corrections to the ground state of H₂ calculated without using the Born–Oppenheimer approximation. *Phys. Rev. A* **97**, 060501 (2018).
- [205] Pachucki, K. & Komasa, J. Nonrelativistic energy of tritium-containing hydrogen molecule isotopologues. *Mol. Phys.* **120**, e2040627 (2022).
- [206] Veirs, D. K. & Rosenblatt, G. M. Raman line positions in molecular hydrogen: H₂, HD, HT, D₂, DT, and T₂. *J. Mol. Spectr.* **121**, 401–419 (1987).
- [207] Chuang, M.-C. & Zare, R. N. Rotation-vibration spectrum of HT: Line position measurements of the 1-0, 4-0, and 5-0 bands. *J. Mol. Spectr.* **121**, 380 – 400 (1987).
- [208] Józwiak, H., Cybulski, H. & Weisło, P. Hyperfine components of rovibrational dipole transitions in HT and DT. *J. Quant. Spectr. Rad. Transfer* **270**, 107662 (2021).
- [209] Niemes, S. *et al.* Accurate reference gas mixtures containing tritiated molecules: Their production and Raman-based analysis. *Sensors* **21**, 6170 (2021).
- [210] V. Hermann, B. Rothmund, F. M. J. Cozijn, M. L. Diouf, W. Ubachs, M. Schlösser, Pressure control of tritiated hydrogen isotopologues in hermetically sealed vessels by non-evaporable getters for sub-Doppler resolution spectroscopy, to be published (2024).
- [211] Puchalski, M., Komasa, J. & Pachucki, K. Nuclear spin-spin coupling in HD, HT, and DT. *Phys. Rev. Lett.* **120**, 083001 (2018).

List of Publications

The chapters in this thesis are based on the following publications:

- **Chapter 4:**
F.M.J. Cozijn, P. Dupré, E.J. Salumbides, K.S.E. Eikema and W. Ubachs, “Sub-Doppler frequency metrology in HD for test of fundamental physics,” *Phys. Rev. Lett.* **120**, 153002 (2018).
- **Chapter 5:**
F.M.J. Cozijn, M.L. Diouf, V. Hermann, E.J. Salumbides, M. Schlösser and W. Ubachs, “Rotational level spacings in HD from vibrational saturation spectroscopy,” *Phys. Rev. A* **105**, 062823 (2022).
- **Chapter 6:**
F.M.J. Cozijn, M.L. Diouf, and W. Ubachs, “Saturation spectroscopy of R(0), R(2) and P(2) lines in the (2-0) band of HD,” *Eur. Phys. J. D* **76**, 220 (2022).
- **Chapter 7:**
F.M.J. Cozijn, M.L. Diouf, and W. Ubachs, “Lamb Dip of a Quadrupole Transition in H₂,” *Phys. Rev. Lett.* **131**, 073001 (2023).
- **Chapter 8:**
M.L. Diouf, F.M.J. Cozijn and W. Ubachs, “Hyperfine structure in a vibrational quadrupole transition of ortho-H₂,” *Mol. Phys.*, e2304101 (2024).
- **Chapter 9:**
F.M.J. Cozijn, M.L. Diouf, V. Hermann, M. Schlösser and W. Ubachs, “Precision Measurement of Vibrational Quanta in Tritium Hydride (HT),” *Phys. Rev. Lett.* **132**, 113002 (2024).

The author also contributed to the following publications:

- (i) F.M.J. Cozijn, J. Biesheuvel, A.S. Flores, W. Ubachs, G. Blume, A. Wicht, K. Paschke, G. Erbert and J.C.J. Koelemeij, “Laser cooling of beryllium ions using a frequency-doubled 626 nm diode laser,” *Opt. Lett.* **38**, 2370-2372 (2013).
- (ii) M.L. Diouf, F.M.J. Cozijn, B. Darquié, E.J. Salumbides and W. Ubachs, “Lamb-dips and Lamb-peaks in the saturation spectrum of HD,” *Opt. Lett.* **44**, 4733-4736 (2019).
- (iii) R. Tóbiás, T. Furtenbacher, I. Simkó, A.G. Császár, M.L. Diouf, F.M.J. Cozijn, J.M.A. Staa, E.J. Salumbides and W. Ubachs, “Spectroscopic-network-assisted precision spectroscopy and its application to water,” *Nat. Commun.* **11**, 1708 (2020).
- (iv) M.L. Diouf, F.M.J. Cozijn, K.F. Lai, E.J. Salumbides and W. Ubachs, “Lamb-peak spectrum of the HD (2-0) P(1) line,” *Phys. Rev. Res.* **2**, 023209 (2020).
- (v) S. Patra, M. Germann, J.Ph. Karr, M. Haidar, L. Hilico, V.I. Korobov, F.M.J. Cozijn, K.S.E. Eikema, W. Ubachs and J.C.J. Koelemeij, “Proton-electron mass ratio from laser spectroscopy of HD⁺ at the part-per-trillion level,” *Science* **369**, 1238-1241 (2020).
- (vi) M.L. Diouf, R. Tóbiás, I. Simkó, F.M.J. Cozijn, E.J. Salumbides, W. Ubachs and A.G. Császár, “Network-Based Design of Near-Infrared Lamb-Dip Experiments and the Determination of Pure Rotational Energies of H₂¹⁸O at kHz Accuracy,” *J. Phys. Chem. Ref. Data* **50**, 023106 (2021).
- (vii) M. Melosso, M.L. Diouf, L. Bizzocchi, M.E. Harding, F.M.J. Cozijn, C. Puzzarini and W. Ubachs, “Hyperfine-Resolved Near-Infrared Spectra of H₂¹⁷O,” *J. Phys. Chem. A* **125**, 7884–7890 (2021).

-
- (viii) M.L. Diouf, R. Tóbiás, T.S. van der Schaaf, F.M.J. Cozijn, E.J. Salumbides, A.G. Császár and W. Ubachs, “Ultraprecise relative energies in the (2 0 0) vibrational band of H_2^{16}O ,” *Mol. Phys.* **120**, e2050430 (2022).
- (ix) M.L. Diouf, R. Tóbiás, F.M.J. Cozijn, E.J. Salumbides, C. Fábri, C. Puzzarini, A.G. Császár and W. Ubachs, “Parity-pair-mixing effects in nonlinear spectroscopy of HDO,” *Opt. Express.* **30**, 46040-46059 (2022).
- (x) R. Tóbiás, M.L. Diouf, F.M.J. Cozijn, W. Ubachs and A.G. Császár, “All paths lead to hubs in the spectroscopic networks of water isotopologues H_2^{16}O and H_2^{18}O ,” *Commun. Chem.* **7**, 34 (2024).
- (xi) W. Ubachs, A.G. Császár, M.L. Diouf, F.M.J. Cozijn and R. Tóbiás, “A Network Approach for the Accurate Characterization of Water Lines Observable in Astronomical Masers and Extragalactic Environments,” *ACS Earth Space Chem.* **8**, 1901-1912 (2024).
- (xii) V. Hermann, B. Rothmund, F.M.J. Cozijn, M.L. Diouf, W. Ubachs and M. Schlösser, “Pressure control of tritiated hydrogen isotopologues in hermetically sealed vessels by non-evaporable getters for sub-Doppler-resolution spectroscopy,” *Submitted* (2024).

Dankwoord

Het einde van een tijdperk zullen sommigen zeggen. Voor mij is vooral de vraag: waar te beginnen? Na zoveel jaren in het Laserlab doorgebracht te hebben zijn het aantal mensen en collega's die onderdeel zijn geweest van deze lange periode bijna ontelbaar geworden en kan ik een boekje op zichzelf schrijven om iedereen voldoende recht te doen aan zijn of haar bijdrage.

Om het toch wat structuur te geven wil ik beginnen bij het begin. Dus bedankt Jeroen, jij hebt lang geleden het vuurtje voor experimentele natuurkunde en laserfysica in mij aangewakkerd door mij al in een vroeg stadium van mijn studie destijds bij jouw experiment te betrekken, want jij had al snel door dat ik liever in het lab stond dan in de collegezalen zat (of aan het schrijven was). Door deze beginfase voelde ik mij al direct thuis in het Laserlab, en dat is nooit veranderd.

Wim, ik weet nog goed dat jij mij had gevraagd om een mogelijke PhD positie te bespreken. Het zou om een volledig nieuw experiment gaan, wat mij als experimentalist pur sang natuurlijk direct aansprak. Na de eerste 4 jaar van mijn PhD waren er al voldoende resultaten voor een deftig proefschrift, maar we hadden allebei honger naar meer en hadden een ultiem doel gesteld; verzadiging van de quadrupool transitie in H_2 . Bovendien wist jij het steeds te regelen dat er toch weer ruimte was om door te gaan, voor mij soms nog steeds een raadsel hoe je dit precies voor elkaar kreeg. Maar voor mij is de cirkel nu rond. De doelen zijn behaald en ben dankbaar dat ik alle aspecten van het experiment heb mogen uitvoeren, van ontwerp tot publicatie. Bedankt dat je mij al die jaren de mogelijkheden, vrijheid en steun hebt gegeven om dit te volbrengen. We hebben iets prachtigs neergezet en ik ben enorm trots op het resultaat dat we hebben behaald.

I would also like to thank Edcel. Your guidance and support at the onset of the experiment were of huge importance. Your critical thinking helped

me tremendously and your never-ending good spirits made working in the lab always enjoyable.

After a few years on my own, Meissa joined the experiment as my partner in crime on the experiment. I think we were an amazing team and worked very synergistically; you were on the programming and performing the bulk of the measurements, and I was on the experiment side. Your never-ending energy during campaigns to squeeze out the tiniest and weakest signals was a joy to see. I'm proud and happy to see you moving on in your physics career abroad, but as a true friendship, our paths will definitely cross again in the future.

Collaborations are a fact of life when working with Wim. The many Laserlab access programs brought in multiple research groups, which really broadened the scientific scope of the experiment. First, I would like to thank Roland and Atilla for the highly successful and longstanding collaboration on water spectroscopy. I liked the fact that the experiment obtained a broader purpose and it was a nice distraction in between our hydrogen campaigns. Next, I would like to thank both Magnus and Valentin. It was a bold move to perform the same experiment on radioactive tritium, but with careful planning, engineering, and sufficient patience we pulled it off. The last and most recent collaboration on methanol with Clément and Alexandr was also very enjoyable by pushing our frequency calibration infrastructure to the absolute limit. Thank you Clément for adopting the experiment and continuing to pursue new scientific goals. I'm sure and convinced the setup will be in good hands for the future.

Ook de mensen in zowel de mechanische als elektronische werkplaats waren onmisbaar voor het succesvol maken van dit onderzoek en experiment. Bedankt Joost, Jacob en Jurriaan voor het meedenken en maken van de mechanische onderdelen en bedankt Tim voor het ontwikkelen van de ruisarme piezo versterkers. Maar ik wil met name Mike bedanken voor zijn langdurige inzet en support voor het maken van talloze onderdelen voor de opstelling. Zonder jouw inspanningen en snelle service had het bouwen veel langer geduurd.

Hoewel ik zelf een handige jongen ben, is de technische support vanuit onze eigen groep van onmisbaar belang. Rob, bedankt voor al je inzet door de jaren heen. Je kritische en praktische blik op de zaken zijn enorm nuttig geweest en door je snelle hulp en inspanning konden wij altijd snel door met de experimenten.

Bedankt Kjeld, zonder jouw fantastische infrastructuur waren de metingen niet mogelijk geweest. Succes in het komende jaar met de grote verhuizing van het lab, ik ben zeer benieuwd hoe het er straks bij staat in het nieuwe gebouw.

I would also like to thank all other current and previous colleagues in the lab who were absolutely vital for the enjoyable mood in and outside the lab. First of all, I would like to thank all people in close proximity to my experiment during all those years. So thanks, Joël, Cung Feng, Madhu, Kenneth, Ming Li. Just a few meters further I would like to thank the people from the metastable helium corner, so thanks Wim, Remi, Bob, Yuri, Raphael, Oleksiy, Adonis and Ruud. En natuurlijk niet te vergeten Kees, bedankt voor de gezelligheid in de laatste fase. Het voelde soms even als the last-man-standing in die grote ruimte samen. Bedankt voor het lachen en het enthousiasme voor de airfryer bij mij aan te wakkeren en succes met je nieuwe zand business. Rodrigo and Sougandh, thanks for assisting me with the new frequency comb and new VSL link. Also thanks to Max, the Daniël's, Rick, Maarten, Wander, Jillis, Dmitrii, Matthias, Sayan, Jia, Vincent, Andrès, Alejandra, Elmer, Charlaine, Julian, Mathieu, Laura, Robert, Matthijs, Anne, Johannes and André. Ook wil ik al mijn vrienden buiten het lab bedanken voor de nodige ontspanning en om mijn gedachten af en toe op iets anders te zetten.

Ik wil ook graag mijn familie bedanken, waarbij in het bijzonder mijn lieve en zorgzame ouders. Zonder jullie onvoorwaardelijke steun in de begindagen van mijn studie had ik hier nu nooit gestaan. Jullie hulp met de verbouwing en zorg rondom Tobi is ontzettend fijn en onmisbaar geweest. Mede daardoor heb ik mijn PhD en proefschrift met onstpanning kunnen afronden.

Als laatste wil ik natuurlijk Nusch bedanken. Lieve Nusch, aan het begin van mijn promotietraject leerden wij elkaar kennen. Ondanks dat je niet altijd precies begreep wat ik deed, heb je mij altijd gesteund in mijn passie. In de laatste fase van het schrijven van mijn proefschrift werd je geduld soms even op de proef gesteld, maar zodra je deze woorden leest zit het er echt op! Op naar nieuwe uitdagingen en avonturen. Ik heb er heel veel zin in om dat samen met jou en Tobi te ontdekken.